Universidade Estadual de Campinas
Faculdade de Engenharia Elétrica e de Computação
Departamento de Sistemas e Energia

Andres de Jesus Arguello Guillen

RESONANCE ASSESSMENT IN POWER SYSTEMS WITH DFIG-BASED WIND PARKS

Análise de ressonância em sistemas de potência com parques eólicos baseados em GIDA

Campinas
2019

State University of Campinas
School of Electrical and Computer Engineering
Departament of Systems and Energy

Andres de Jesus Arguello Guillen

RESONANCE ASSESSMENT IN POWER SYSTEMS WITH DFIG-BASED WIND PARKS

Análise de ressonância em sistemas de potência com parques eólicos baseados em GIDA

Dissertation presented to the School of Electrical and Computer Engineering of the State University of Campinas as part of the mandatory requirements to obtain the *Master in Electrical Engineering* degree, in the area of *Electric Power Systems.*

Dissertação apresentada à Faculdade de Engenharia Elétrica e de Computação da Universidade Estadual de Campinas como parte dos requisitos exigidos para a obtenção do título de *Mestre em Engenharia Elétrica*, na área de *Energia Elétrica.*

Supervisor:
Prof. Dr. Walmir de Freitas Filho

Este exemplar corresponde à versão final da tese defendida pelo aluno Andres de Jesus Arguello Guillen, e orientada pelo
Prof. Dr. Walmir de Freitas Filho

Campinas
2019

Agência(s) de fomento e nº(s) de processo(s): Não se aplica.
ORCID: https://orcid.org/0000-0003-2084-4342

Ficha catalográfica
Universidade Estadual de Campinas
Biblioteca da Área de Engenharia e Arquitetura
Elizangela Aparecida dos Santos Souza - CRB 8/8098

Arguello Guillen, Andres de Jesus, 1991-
Ar38r Resonance assessment in power systems with DFIG-based wind parks / Andres de Jesus Arguello Guillen. – Campinas, SP : [s.n.], 2019.

Orientador: Walmir de Freitas Filho.
Dissertação (mestrado) – Universidade Estadual de Campinas, Faculdade de Engenharia Elétrica e de Computação.

1. Energia elétrica. 2. Estabilidade. 3. Frequencias harmônicas. 4. Máquinas elétricas de indução. 5. Parque eólico. 6. Ressonância. I. Freitas Filho, Walmir de, 1971-. II. Universidade Estadual de Campinas. Faculdade de Engenharia Elétrica e de Computação. III. Título.

Informações para Biblioteca Digital

Título em outro idioma: Análise de ressonância em sistemas de potência com parques eólicos baseados em GIDA
Palavras-chave em inglês:
Electric energy
Stability
Harmonic frequencies
Induction electric machines
Wind park
Resonance
Área de concentração: Energia Elétrica
Titulação: Mestre em Engenharia Elétrica
Banca examinadora:
Walmir de Freitas Filho [Orientador]
Luiz Carlos Pereira da Silva
Osvaldo Ronald Saavedra Mendez
Data de defesa: 30-01-2019
Programa de Pós-Graduação: Engenharia Elétrica

COMISSÃO JULGADORA - DISSERTAÇÃO DE MESTRADO

Candidato: Andres de Jesus Arguello Guillen RA: 190723

Data da Defesa: 30 de janeiro de 2019

Título da Tese: Resonance assessment in power systems with DFIG-based wind parks.

Análise de Ressonâcia em Sistemas de Potência com Parques Eólicos baseados em GIDA.

Prof. Dr. Walmir de Freitas Filho (Presidente)

Prof. Dr. Luiz Carlos Pereira da Silva

Prof. Dr. Osvaldo Ronald Saavedra Mendez

A ata de defesa, com as respectivas assinaturas dos membros da Comissão Julgadora, encontra-se no SIGA (Sistema de Fluxo de Dissertação/Tese) e na Secretaria de Pós-Graduação da Faculdade de Engenharia Elétrica e de Computação.

"One day I will find the words, and they will be simple."
(Jack Kerouac)

To my family, friends and the eager reader

Acknowledgements

To Prof. Dr. Walmir de Freitas Filho for his tutoring and advice, as well as for entrusting me with this research topic and the oportunity to work with the Power System's research group of the FEEC-UNICAMP.

To Dr. Tiago Rodarte Ricciardi for working with me in several parallel research topics.

A special recognition to Dr. Ricardo Torquato Borges for his technical support and guidance on how to develop, structure and present this research project.

To my LE-41 lab colleagues for their warm welcome as a member of the group.

To Natali Versiani for the information of the wind park technologies at north-east and south regions wind of Brazil.

To Dr. Alécio Barreto Fernandes for the information of the characteristics of feeders and capacitor banks in several examples of wind park projects in Brazil.

To Dr. Gustavo Valverde Mora for giving me the oportunity to work with him since I was an undergraduate student, in research and field studies that eventually led to a job in the academic community.

To my dear wife Bruna Ribeiro Braga for her inconditional love and patience.

To my family for their love and entire support to study and pursue an engineering career.

To the University of Costa Rica (UCR), the School of Electrical Engineering (EIE), and the Office of Internacional Affairs and External Cooperation (OAICE) for the economical support, and the specialization scholarship oportunity.

Abstract

The increase of the penetration of wind parks (WP) based on doubly-fed induction generators (DFIG) in electric power systems may bring problems associated with high-frequency resonances in the range between 180 Hz and 1500 Hz. There are two main phenomena to be analyzed: unstable resonances, when a resonance occurs in frequencies where the DFIG voltage source converters (VSC) have negative damping characteristic; and weakly damped resonances close to frequencies such as 5^{th}, 7^{th}, 11^{th} and 13^{th} harmonics, which are typically present as background grid distortions. Traditionally, these resonances are studied with electromagnetic transient (EMT) simulations as they are able to account for all dynamic characteristics of the circuit. However, numerous EMT simulations are generally required in the studies, which leads to high computational costs.

This dissertation develops simplified approaches to address these resonances. Prior to developing these methods, it is first confirmed that, at frequencies between 180 Hz and 1500 Hz, the DFIG can be modeled as a linear impedance using the average model of the VSCs. Then, a chart is developed to quickly identify if a WP can become unstable. This chart establishes a risk region: if WP and grid characteristics (short-circuit level to wind park size ratio and reactive compensation to wind park size ratio) lay inside this region, the WP can become unstable. It is found that this risk region can be significantly reduced by properly designing the control parameters of the converters. Therefore, high-frequency instabilities are unlikely to become a general concern for utilities. Nevertheless, weakly damped harmonic resonances can still occur and must be considered when operating and designing DFIG-based WPs.

Two additional charts are proposed to analyze the risk of weakly damped harmonic resonances in the system. The charts establish a risk region by correlating the short-circuit level of the grid at the point of common coupling, with the WP rated power capacity and reactive power compensation level. Two parameters delimit this risk region: Resonance frequency and voltage amplification with respect to background harmonic distortions in the grid.

All three charts proposed in this dissertation can be obtained analytically, based on wind park impedance models, without the need for running any simulation. A measurement-based method is also developed to obtain these charts without prior knowledge of any wind park characteristic. These methods for obtaining the charts were properly validated with detailed EMT simulations. The proposed charts can be easily obtained and consulted by engineers, and have the potential to greatly facilitate resonance assessment in systems with WPs.

Keywords: Doubly fed induction generator; harmonic resonance; high-frequency stability; power quality; wind parks.

Resumo

O incremento da penetração de parques eólicos (PE) baseados em geradores de indução duplamente alimentados (GIDA) no sistema de potência elétrica pode trazer problemas de qualidade de energia relacionados com ressonância de alta frequência no intervalo de 180 Hz e 1500 Hz. Dois problemas potenciais são analisados: Ressonância instável pela caraterística de amortecimento negativo dos conversores tipo fonte de tensão (VSC); e ressonâncias mal amortecidas pela excitação de componentes de distorção de tensão na rede próximos à 5^{ta}, 7^{ma}, 11^{ra} e 13^{ra} harmônicas. Estas ressonâncias são estudadas com numerosas simulações de transitórios eletromagnéticos (TEM) já que levam em conta as caraterísticas dinâmicas do circuito mas com alto nível de detalhe e custo computacional.

Este documento apresenta o desenvolvimento de métodos simplificados para estudar as ressonâncias. Inicialmente, esta dissertação confirma que em frequências entre 180 Hz e 1500 Hz, o GIDA pode-se modelar como uma impedância linear com o modelo *average* dos VSCs. Posteriormente, desenvolve-se um gráfico para identificar rapidamente se um parque eólico vira instável. Este gráfico estabelece uma região de risco: se as características do parque eólico e da rede (relação de curto circuito e relação de potência compensação reativa) estão localizadas dentro desta região, o parque pode virar instável. Este problema pode-se mitigar com uma escolha adequada de parâmetros de controle, e por tanto, não deveria representar um problema geral para o operador de rede. Mesmo assim, a ressonância mal amortecida pode ocorrer e deve-se considerar ao operar e projetar PEs baseados em GIDA.

Dois gráficos adicionais são propostos para analisar o risco de ressonâncias mal amortecidas no sistema. Os gráficos estabelecem a região de risco correlacionando o nível de curto-circuito da rede no ponto de acoplamento comum, com a capacidade nominal do parque eólico e o nível de compensação de potência reativa. Dois parâmetros delimitam a região: A frequência de ressonância, e a amplificação de tensão com respeito a distorções harmônicas na rede.

Os três gráficos propostos nesta dissertação podem-se obter analiticamente com os modelos de impedância dos PEs sem necessidade de simulação. Um método baseado em medição também foi desenvolvido para obter os gráficos sem conhecimento prévio das características do parque. Estes métodos para obter os gráficos foram validados com simulações detalhadas de transitórios eletromagnéticos. Os gráficos propostos podem ser facilmente obtidos e consultados por engenheiros, e apresentam grande potencial para facilitar a análise de ressonância em sistemas com PEs.

Palavras-chaves: Gerador de indução duplamente alimentado; ressonância harmônica; estabilidade de alta frequência; qualidade de energia; parques eólicos.

List of figures

List of tables

Table of contents

1 Introduction

The increasing penetration of power electronics based equipment in power systems, such as wind parks (WP), brings up a series of challenges to ensure adequate operating conditions. For example, it is important to assess power quality issues such as overvoltages due to harmonic distortion and resonances.

Resonance problems in wind parks at low frequencies (8 Hz) were reported in Germany (BUCHHAGEN *et al.*, 2015) and China (XIE *et al.*, 2017), and at high frequencies (900 Hz) were reported in India (PATEL; JOSHI, 2017; SORENSEN *et al.*, 2000) and Spain (BACELLS; GONZÁLEZ, 2011).

These resonance problems gain relevance in the academic community and industry due to the sustained growth of wind generation adoption in the last two decades, reaching a world-wide installed capacity near 500 GW in 2016 according to (REN21, 2017). China has the largest share by holding roughly 170 GW of installed capacity or 34 % of the world's total, and according to (ABEEÓLICA, 2017) at 2017, Brazil held 13.3 GW of operating wind power plants plus 4.65 GW in pending projects, corresponding to 8.3 % of Brazil's total installed capacity. These numbers demonstrate the high participation of wind worldwide, and thus, the importance of studying the power quality impacts of wind parks.

The doubly-fed induction generator (DFIG) and full-converter generator are the technologies with the largest share of participation in the market (XIE *et al.*, 2017), the DFIG being the predominant. For example: Brazil's north-eastern region has over 11400 MW of wind generation installed capacity, 84 % of it being DFIG technology (ONS, 2018); and China's northern region has a wind generation installed capacity of 3423 MW, where 83 % is DFIG-based (XIE *et al.*, 2017). These generators are able to operate at variable wind speeds as their power electronics converters allow for a more flexible control (WECC, 2011). The DFIG has a lower commercial cost than the full-converter due to the following characteristics:

- The power electronics converters of the DFIG are sized at about 30 % of the rated generator capacity, whereas full-converter technologies are sized at 100 %;
- The DFIG uses a typical wounded rotor induction machine, whereas materials such as the permanent magnets used in full-converters, are scarcer.

DFIGs allow for active power control and a partial reactive power control. The authors in (BAROUDI *et al.*, 2007) present a summary of the different wind generator converter topologies and machines, listing the advantages and disadvantages. DFIGs are more vulnerable than full-converters to grid disturbances due to their topological characteristics:

- Direct coupling of the machine's stator windings to the grid: This means that its impedance interacts with the grid and the stator is exposed to transient events, unbalance, and resonance (SONG; BLAABJERG, 2017b);
- Capacitance required for steady-state reactive power compensation: Every shunt capacitor stage causes a different high-frequency resonance (LEAO *et al.*, 2014).

Detailed theoretical development of the resonances associated with WPs based on the circuit impedances is given in (ZHENG; BOLLEN, 2010). The authors mention that the induction machine impedance and the circuit's resistances are important to assess the amplification at resonance, but they neglect the effect of the power converters. Authors in (SONG; BLAABJERG, 2017b) point out the power electronics converters control affects the resonance characteristics and need to be included in resonance studies.

The previously stated points motivate a more in-depth analysis of the resonance phenomenon in power systems with penetration of DFIG-based WPs. This dissertation studies high-frequency resonances caused by capacitor banks that are used for reactive power compensation on DFIG-based WPs, including the interaction of the power electronics converters control with the grid.

1.1 Resonances associated with capacitor banks of DFIGs

The diagram at Fig. 1.1 corresponds to a circuit of a DFIG-based wind park (represented by the equivalent of one large generator) connected to the transmission system at the high voltage (HV) bus. The DFIG has two power electronics converters in back-to-back configuration: The rotor-side converter (RSC) which is connected to the rotor of the machine and regulates the active and reactive power injection; and the grid-side converter (GSC), which in this study, regulates the voltage of the DC bus and is connected to the grid via a filter. The DFIG is connected at the low voltage (LV) bus through the stator of the induction machine (IM) and the filter of the GSC. The wind park has a capacitor bank for steady-state reactive power support, power factor correction and fault ride-through, connected at the medium voltage (MV) bus.

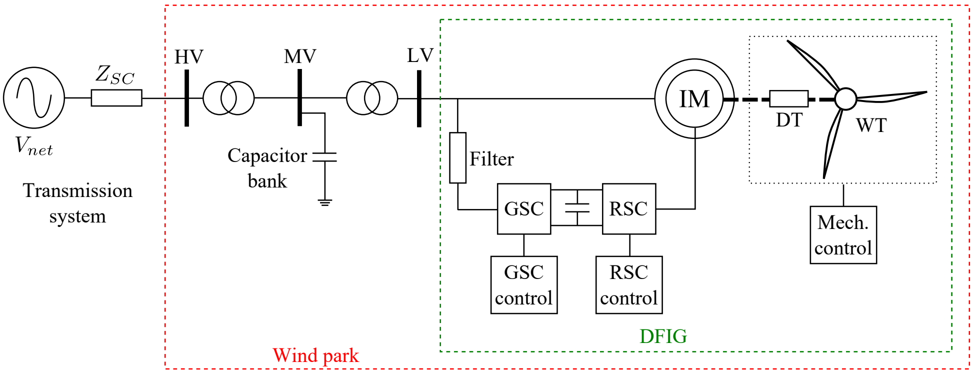

Figure 1.1 – Circuit of a DFIG-based wind park

The shunt capacitor banks create resonances in the circuit. It is important to understand the range of frequencies of such resonances as this range is a key parameter to determine the stability and voltage amplification of the resonance (LEAO *et al.*, 2014).

The reactive compensation of WPs is sized to maintain a near-to-unity power factor at the PCC (0.95-0.98 leading or lagging in the United States; 0.9 lagging to 0.95 leading while within the $1 \pm 5\%$ pu band of voltage at PCC in Canada (CAMM *et al.*, 2009); 0.95 leading or lagging in Brazil (ONS, 2010)).

Commercial power converters for DFIGs have a capability around 0.95 lagging to 0.9 leading on their own, however, they are used in combination with the discrete capacitor bank stages to enhance the generator's capability curve (CAMM; EDWARDS, 2008).

The power factor pf of a WP can be calculated with expression (1.1) (CAMM; EDWARDS, 2008) by compensating with the power of a capacitor bank Q_C for the reactive power losses Q_L of the transformers and feeders and generators, at a given active power production of P.

$$pf = \frac{P}{\sqrt{P^2 + (Q_C - Q_L)^2}} \tag{1.1}$$

For example, a wind park of rated capacity $S_{WP} = 200$ MVA injecting $P = 200$ MW of active power, with reactive power losses of $Q_L = 37$ MVAr and a compensation bank of $Q_C = 72$ MVAr, results in a power factor of $pf = 0.985$ leading (CAMM; EDWARDS, 2008). The respective reactive compensation ratio corresponds to $Q_C/S_{WP} = 0.36$.

The capacitor bank can resonate with the inductances from the grid, the feeders, the GSC filter and the induction machine. Fig. 1.2 presents the resonance frequency value for several combinations of short-circuit level S_{SC}, reactive power compensation Q_C and wind park size S_{WP}. These parameters result in different combinations of short-circuit ratios S_{SC}/S_{WP} and reactive power compensation ratios Q_C/S_{WP}. The figure is built for a wind park with a rated capacity of $S_{WP} = 100$ MVA and performing multiple EMT simulations for different combinations of parameters. The results from Fig. 1.2 show the capacitor bank can resonate with the inductance of the grid and of the DFIG in the range of frequencies between 180 and 1500 Hz.

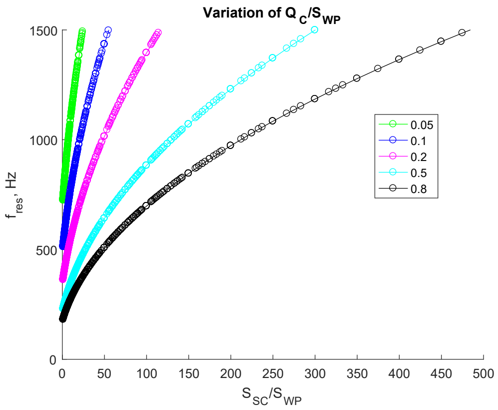

Figure 1.2 – Typical resonance frequency in DFIG-based WPs due to reactive compensation

This resonance frequency can also be estimated analytically based on the simplified representation of the DFIG-based wind park of Fig. 1.3. The resonance frequency of such circuit is given by expression (1.2), with the equivalent inductance at PCC, i.e., L_{PCC} (a shunt equivalent of the inductances of the grid equivalent, the induction machine and filters) and the capacitance C_{PCC} of the reactive power compensation bank.

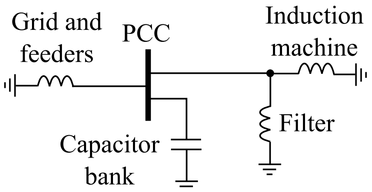

Figure 1.3 – Inductances of the DFIG wind park that resonate with the capacitor bank

$$f_{res} = \frac{1}{2\pi\sqrt{L_{PCC}C_{PCC}}} \tag{1.2}$$

1.2 Unstable and weakly damped resonance of DFIGs

Problematic high-frequency resonances associated with the interaction of the grid and the converter control of DFIGs can be divided in two main types (SONG; BLAABJERG, 2017a; SONG; BLAABJERG, 2017b; SONG *et al.*, 2017):

- Unstable resonance: It appears when a natural oscillation mode (i.e., a resonance frequency) of the system presents positive feedback through the control loop of the converters. This occurs due to the negative damping characteristic of the VSCs, which is associated with phase shifts in the control circuit caused by filtering, delays in the feedback loop and the gains of the current controllers. The waveforms in Fig. 1.4 were obtained with EMT simulation at the PCC of a DFIG with a wind turbine, as in Fig. 1.1. Note that, at unstable resonance, the DFIG sustains an additional voltage component in the frequency of resonance without external excitation. Such condition may occur after connecting a group of generators, grid reconfigurations, or switching a capacitor bank, which leads to a resonance frequency with negative damping. This type of resonance is further explained in chapter 3.

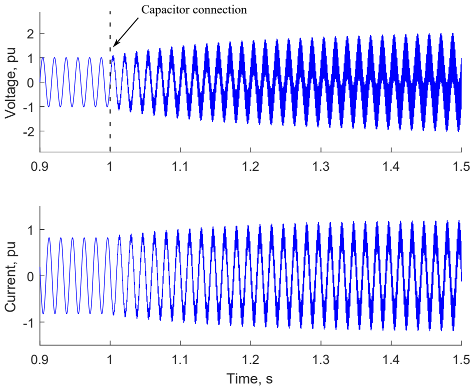

Figure 1.4 – Unstable resonance at 1067 Hz due to capacitor switching

- Weakly damped resonance: It occurs at stable conditions and it can be observed as the amplification of background voltage distortions of the grid. It occurs when there is a background harmonic distortion component close to a resonance frequency of the system, as observed in the waveforms of Fig. 1.5 for the PCC of a DFIG with a wind turbine. This type of resonance is further explained in chapter 4.

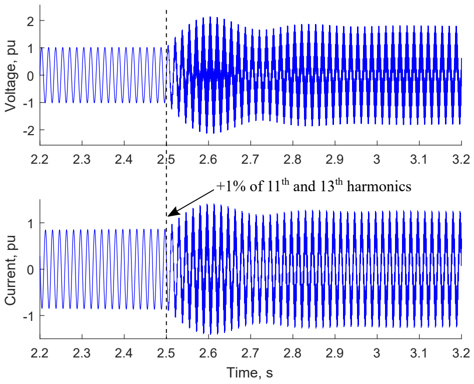

Figure 1.5 – Weakly damped resonance at 780 Hz due to grid distortion at 13^{th} harmonic

These resonances are analyzed in the literature with the following approaches:

- Full time domain modelling and simulation: It uses EMT simulation at every tested scenario with highly detailed differential and non-linear models. It is the most accurate approach but requires the highest computational and modelling effort (LAROSE *et al.*, 2013; BUCHHAGEN *et al.*, 2015; KARAAGAC *et al.*, 2018). This approach obtains a numerical solution of the system. With this method, it is possible to evaluate any type of disturbances for both weakly damped and unstable resonances by processing the resulting time domain signals. However, there is a limitation on the size of the system to be modeled due to the computational constraints. In addition, the authors in (BUCHHAGEN *et al.*, 2015) mention that due to intellectual property issues, most manufactures do not reveal great detail of the control system, which makes it even more difficult to represent it accurately;

- Partial time domain / frequency domain modelling and eigenvalue analysis: By using this approach, the EMT model of the WP is linearized at an operating point (neglecting saturations, simplifying certain system stages, and using a first-order approximation of the equations), to later obtain a state-space model (JAZAERI *et al.*, 2012; EBRAHIMZADEH *et al.*, 2018; LIU *et al.*, 2017; FAN *et al.*, 2011). Eigenvalue analysis is applied to the state transition matrix to obtain the system's singularities, and the oscillation modes can be studied with a Nyquist plot or a root-locus map. As the entire system has to be linearized, including the grid, this approach involves a more complex analytic development. This approach is used to study small disturbances. It is also possible to evaluate harmonic resonance in time domain with this model;
- Frequency domain modelling and analysis: This approach is based on the linearized EMT model. It is possible to determine an expression in frequency domain for the WP impedance using the state space matrices from the previous approach, by isolating the transfer function of terminal voltage in terms of the terminal current (MONJO *et al.*, 2015; LIU *et al.*, 2017). With this method the WP can be seen as a frequency dependent Norton equivalent. Only, passive elements, measurement filters, control delays and the fastest control stages are considered to calculate the equivalent impedance. Bode diagrams are commonly used to identify the resonance frequencies. The model is also used to study system stability with the Nyquist plot, or the gain and phase margins in a Bode plot (FAN; MIAO, 2012).

The authors in (WANG; BLAABJERG, 2018) conducted a detailed research on the adequacy of the different modeling techniques available in the literature to study the high-frequency stability in power electronics-based equipment. They determined that the last approach (frequency domain modelling and analysis) can be used on stability studies of the interaction of the grid and the converter control. This model is valid for frequencies lower than the switching frequency of the converters, as the focus of the present study.

1.3 Harmonic distortion profiles of transmission systems and DFIGs

The harmonic resonance problem appears when a resonance of the system is excited by a harmonic distortion with a similar frequency. Therefore, it is important to understand the sources of these distortions, which may come from the grid or from another generator within the WP.

Traditionally, the most common harmonic components in transmission systems are the odd orders non-multiples of the third, e.g., 5^{th}, 7^{th}, 11^{th} and 13^{th} orders. It is not common to find even harmonics in the network unless an equipment malfunctions (irregular power electronics switching) or has erratic behavior (electric arc related phenomena). Multiples of the third order harmonic are also uncommon due to the zero-sequence filtering nature of delta-winding transformers.

Standards such as the IEEE 519-1992 and IEC 61000-3-6 are commonly adopted to limit harmonic emissions. These standards focus on the emission of the equipment or the maximum allowed harmonic distortion in the network in order to ensure electromagnetic compatibility, depending on the voltage level and type of equipment. A comparison of these standards is available in (HALPIN, 2005) and (LEAO *et al.*, 2014).

In Brazil, the limits to waveform distortion due to odd-order harmonics (5^{th}, 7^{th}, 11^{th}, 13^{th}) in the transmission system are detailed in the submodule 2.8 of the PROREDE standard (ONS, 2011). These correspond to 1.5 % for voltages between 13.8 kV to 69 kV, and to 0.6 % for voltages of 69 kV and above. In the studies of this dissertation, the voltage distortions from the transmission system were included individually with a value of 1 % of the fundamental.

Harmonic components can also originate from within the WPs from core saturations and electronic equipment switching (LAROSE *et al.*, 2013; PRECIADO *et al.*, 2015). Important distortions appear at a few kHz due to the action of the PWM switching of the converters (TENTZERAKIS; PAPATHANASSIOU, 2007). In addition, several authors also mention important presence of inter-harmonics, third-order multiples and even order harmonics (YANG *et al.*, 2013; YANG *et al.*, 2011; PRECIADO *et al.*, 2015; YANG *et al.*, 2016; BRADT *et al.*, 2011; ANDRADE *et al.*, 2015). Even though the harmonic spectrum is rich, there is a common consensus that the injection at PCC is low. The circuit is generally able to filter/damp most of the harmonics injected by the generators. This is further confirmed by simulations of this dissertation, as the wind park emissions do not affect the overall results.

1.4 Objectives

The main objectives of this dissertation are:

- Develop an impedance model of DFIG-based wind parks for high-frequency studies. This model will enable simplified analytical studies to predict the behavior of these wind parks, without running detailed EMT simulations;
- Analyze and characterize high-frequency stability limits of DFIG-based wind parks. The idea is to identify under which grid characteristics the DFIG converters can become unstable to mitigate the root causes of these unstable interactions;
- Analyze and characterize harmonic resonances in DFIG-based wind parks. The idea is to identify under which grid characteristics that problematic resonances can occur.

In this case, a resonance is characterized as problematic when it has signifficant amplification of voltage and occurs close to an odd harmonic frequency;

- Develop practical charts for first-screening assessment of the risk of unstable and weakly damped resonances in these wind parks. These charts are developed to help engineers quickly identify problematic conditions on wind parks. They can be obtained analytically, based on the simple analysis of the circuit model, or through measurements collected at the wind park entrance. No computer simulation is required.

1.5 Organization

The rest of this dissertation is organized as follows:

- Chapter 2 presents the development and validation of an impedance-based model for the DFIG. It is built by simplifying the detailed EMT model of DFIGs. Validation studies are also presented to confirm this equivalent impedance can outline the characteristics of the resonance phenomena analyzed in this dissertation;
- Chapter 3 presents the study of stability at high-frequency resonance of the DFIG. A practical chart is proposed to assess the risk of DFIG-based wind parks becoming unstable in a simplified fashion, without the need to run any EMT simulation. A simple analytical approach is presented to build the chart and validated with EMT simulation;
- Chapter 4 presents the study of weakly damped harmonic resonances in circuits with DFIG-based wind parks. Two practical charts are proposed to assess what is the risk of problematic resonances (i.e., resonances with high voltage amplification and close to harmonic frequencies) in a wind park. These charts can be obtained in a simplified fashion, without running any EMT simulation. Model-based and measurement-based approaches to build the charts are presented and validated with EMT simulation;
- Chapter 5 summarizes the main conclusions of this work and outlines ideas for future research.

2 Model of DFIG-based wind parks for high frequencies

This chapter derives an equivalent impedance model for doubly-fed induction generator (DFIG) based wind parks (WP), which will be used in the following chapters to study electric resonance in the frequency range from 180 Hz to 1500 Hz. This model is obtained from the average converter model and then validated with EMT simulation.

Sensitivity studies are also provided to investigate the effect of several system parameters on the resonance frequency and on the amplification level created by a resonance.

2.1 Electromagnetic transients (EMT) model

The EMT model of the DFIG is the most accurate representation of the system and will be discussed in this section. First, a high-level block diagram of a DFIG with a wind turbine is presented in Fig. 2.1 (GAGNON *et al.*, 2010).

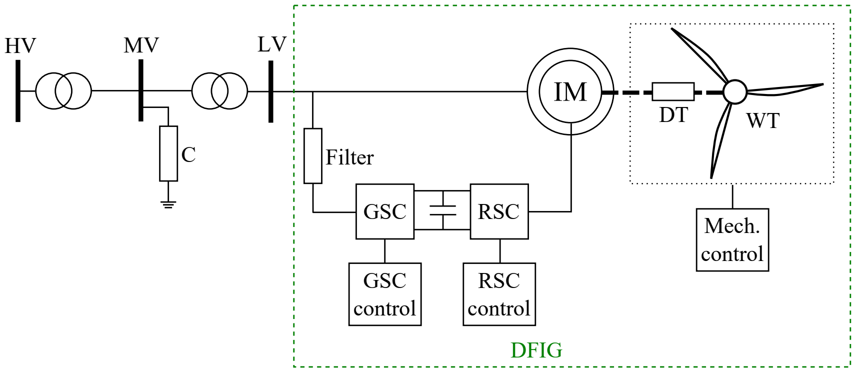

Figure 2.1 – Block diagram of DFIG with a wind turbine

A more detailed diagram with the most relevant internal variables is given in Fig. 2.2. The interaction of the variables and their nomenclature is explained as follows:

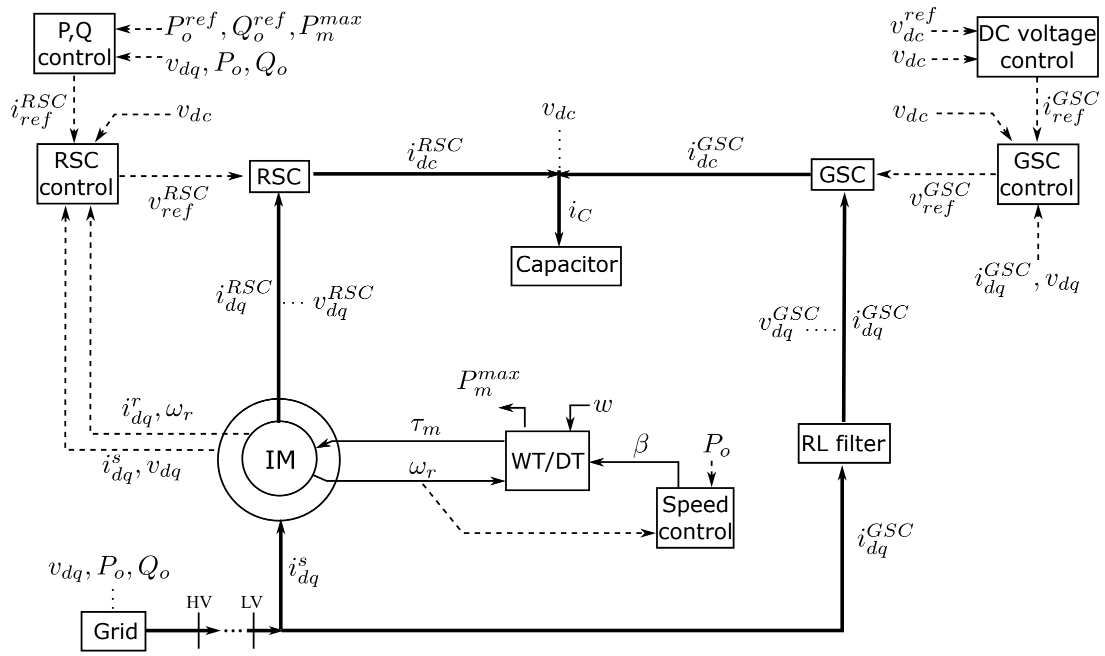

Figure 2.2 – Interaction of variables in model of DFIG with a wind turbine

- Classical wind turbine (WT) algebraic model in terms of the wind speed w, with a two-masses drive train (DT) to couple the mechanical dynamics of the generator and turbine.
- Sixth-order electromechanical model of the induction machine (IM) without saturation nor space harmonics.
- Switched model of the VSCs in back-to-back configuration, with a rotor side converter (RSC) and a grid side converter (GSC).
- DC bus capacitor electric dynamics.
- Resistive-inductive (RL) filter for the GSC (the IM acts as the filter for the RSC). Other filter topologies can be used, such as the inductive-capacitive-inductive (LCL) arrangement (HAMZA *et al.*, 2015).
- The pitch angle β of the blades is adjusted to regulate the injected power P_o. The maximum power point tracking (MPPT) function is used to determine the optimal reference value for rotational speed ω_r, subject to the maximum possible mechanical power P_m^{max} output.
- The present study uses the d component of the output currents of the GSC i_{dq}^{GSC} and its terminal voltages v_{dq}^{GSC} to control the voltage v_{dc} at the capacitor of the DC bus. The q component is left unused in the present dissertation, but it can be controlled to provide additional reactive power support.
- The RSC output currents i_{dq}^{RSC} and voltages v_{dq}^{RSC} are adjusted for active power P_o, and reactive power Q_o / AC voltage /v_{ac} control. Depending on the alignment of the dq axis in the rotor, either the d or q axis currents can be used to control the active power (one controls the electric torque and the other the flux at the rotor). The present study uses the d component for active power and the q component for

reactive power control. These powers are measured at the PCC between the turbine and the grid (in this case, the high voltage (HV) bus, to include the capacitor bank contribution). The reactive power output is limited by the actual active power output and the converters capacity.

The model also includes measurement filters, transient gain reduction blocks, and digital control delays. If the model is used to represent a WP equivalent as in Fig. 2.1, it includes a reactive power compensation capacitance (C) at the medium voltage (MV) bus.

The DFIG control system uses proportional-integral (PI) controllers, with saturation and anti-windup functions. It was designed in per unit (pu) system and dq-frame, with a phase-locked loop (PLL) to track the fundamental frequency and calculate the angle reference at stator terminals (the rotor reference frame also depends on the rotor speed ω_r). The PLL model was fully considered for EMT simulation.

The dynamics of the PLL were later neglected to obtain the analytic impedance model as these are slower than those of the current controllers (the bandwidth of the PLL is generally lower than 100 Hz while the bandwidth of the current controller is around 500 Hz).

When the controllers are in cascade configuration within the same loop, they can be classified as outer and inner control loops. The inner loop is typically designed at least ten times faster than the outer loop to decouple the control dynamics (CHANG; HU, 2017). This distinction is important to build the equivalent impedance model of the DFIG. The outer control loops of the DFIG model correspond to:

- Powers and AC voltage to RSC current reference (P_o,Q_o,$v_{dq} \rightarrow i_{ref}^{RSC}$);
- DC voltage to GSC current reference ($v_{dc} \rightarrow i_{ref}^{GSC}$).

The outputs of the outer loops, as well as the rotational speed of the turbine, are considered constant as their variation is much slower than the high-frequency resonances.

The inner current control loops of the DFIG are detailed in Fig 2.3. These loops compare the measured current values to the references given by the outer loops and set the VSC's voltages:

- RSC currents to RSC voltages ($i_{dq}^{RSC} \rightarrow v_{dq}^{RSC}$);
- GSC currents to GSC voltages ($i_{dq}^{GSC} \rightarrow v_{dq}^{GSC}$).

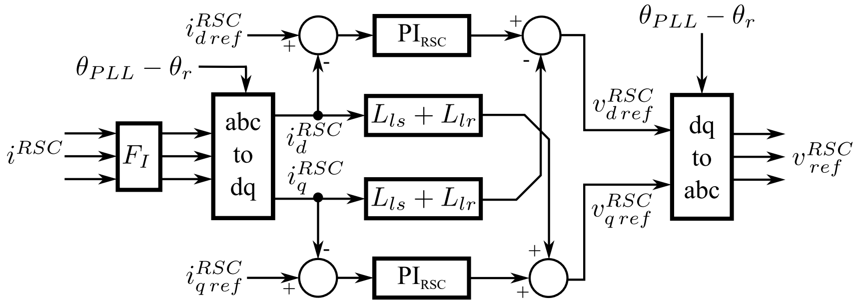

(a) RSC control loop

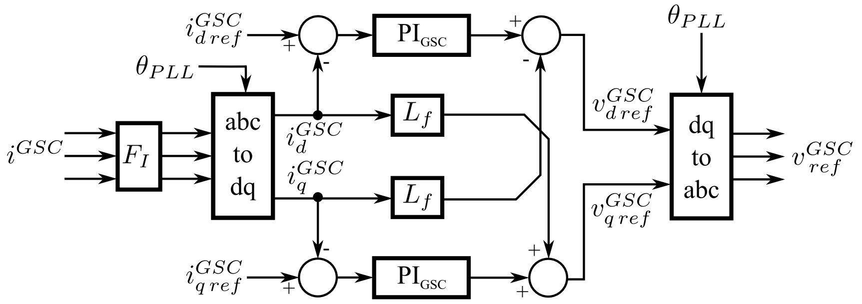

(b) GSC control loop

Figure 2.3 – Current control diagrams of RSC and GSC

The blocks with the transfer functions F_V and F_I filter the high-frequency components of the voltages and the currents of the inner current control loops. These filters introduce a delay in the feedback signal which also affects the equivalent impedance model.

The reference voltages of the converters in Fig. 2.3 include crossed-inductive feed-forward terms. The RSC uses the stator and rotor winding inductances $L_{ls} + L_{lr}$ and neglects the magnetization inductance. The GSC uses the RL filter inductance L_f. Other feed-forward terms can be used or even neglected. This will change the dynamic behaviour of the DFIG and thus, its resulting equivalent impedance model.

Finally, the switched and average converter models are presented in Fig. 2.4(a) and Fig. 2.4(b) respectively. Here, the PWM and switching of the converters are replaced by delay functions F_d^{RSC} and F_d^{GSC} of 1.5 × the converter's switching period (1 × due to delay between measurement sampling and control action, +0.5 × due to delay when updating the PWM cycle).

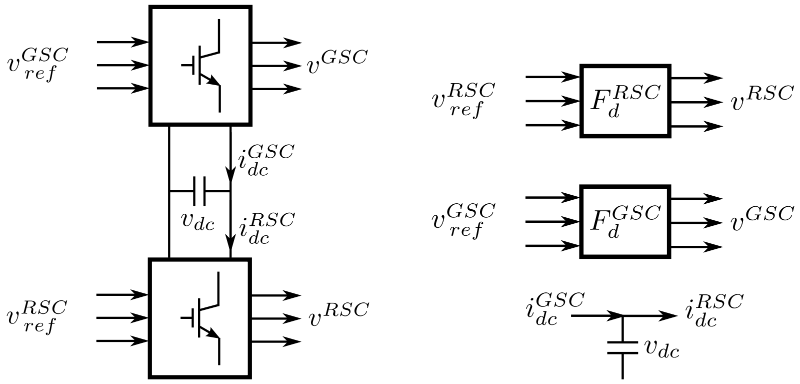

(a) Switched (b) Average

Figure 2.4 – Voltage source converter and DC bus models

2.2 Impedance model

The equivalent impedance representation of the DFIG is widely used in the literature for resonance analysis (SONG; BLAABJERG, 2017a; SONG; BLAABJERG, 2017b; SONG *et al.*, 2017). This model can be obtained by linearizing the average converter EMT model of the DFIG (LIAO *et al.*, 2015; VIETO; SUN, 2017). Several stages of the system can be simplified based on their controller's bandwidth as in Table 1.

Table 1 – Example of typical control bandwidths for DFIG with a wind turbine (WANG, 2014)

Stage	**Bandwidth (Hz)**
Active power and frequency, external loops	0.1
Reactive power, AC and DC voltage, external loop	10
Synchronization with the grid, PLL	100
Current control, internal loop	500
Power electronic commutation, PWM	2500

The DFIG diagram from Fig. 2.1 can be simplified into two independent branches: the RL+GSC branch (grid side converter and its filter); and the IM+RSC branch (induction machine and rotor side converter) by taking into account the following considerations:

- The switched model of the converters was simplified to the average model.
- The DC bus voltage is stiff (constant), so the DC dynamics of the RSC and GSC are decoupled.
- The mechanical stages yield a constant rotational speed due to its slow variation.
- The current references used in the RSC and GSC control circuits are fixed values because the outer control loops have a slow dynamic response (slow variation).
- The filter is modeled as an RL series branch, and the induction machine is modeled with the steady state equivalent.

- The measurement filters and digital control delays were modeled to include the phase shift created by the control circuit.
- Saturations were neglected.

The results from the previous list of considerations can be seen in Fig. 2.5. The RSC and the GSC can now be represented as a current-controlled voltage source.

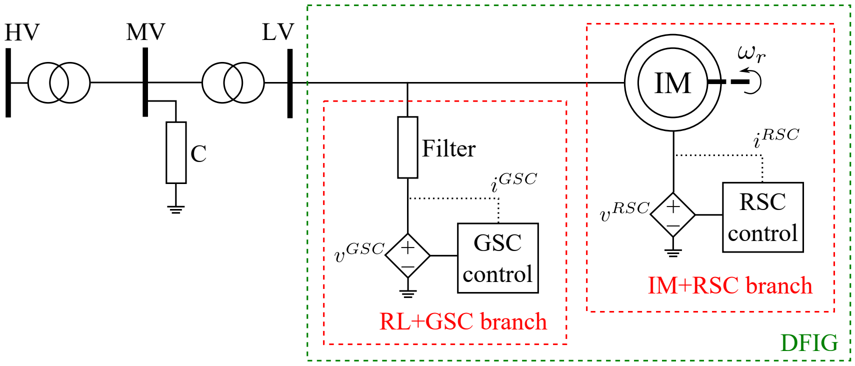

Figure 2.5 – Simplified model of a DFIG with a wind turbine

Fig. 2.6 presents the small-signal representation of the inner current control loop of the converters in *dq* reference frame.

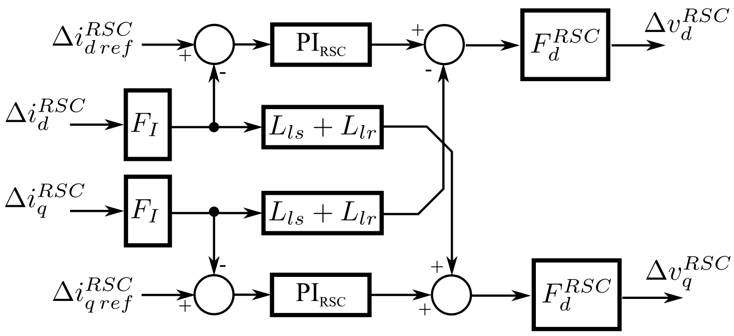

(a) RSC control loop

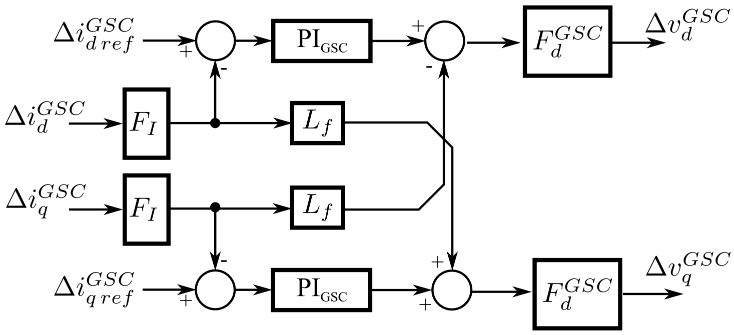

(b) GSC control loop

Figure 2.6 – Current control loops of RSC and GSC, small disturbance

The expressions in frequency domain for the current measurement filters F_I (modeled as a second order filter), and digital control delays $F_{d\,GSC}$, $F_{d\,RSC}$ (modeled as a first order delay), the machine slip η (as function of the mechanical rotational speed ω_r), and the current control PIs (proportional K_p and integral K_i gains) are presented as follows:

$$F_I = \frac{{\omega_I}^2}{\left(s - j\omega_0\right)^2 + 2\xi\omega_I\left(s - j\omega_0\right) + {\omega_I}^2} \qquad \omega_I = 2\pi f_I \tag{2.1}$$

$$F_{d\,GSC} = \frac{1}{T_{d\,GSC}\left(s - j\omega_0\right) + 1} \qquad F_{d\,RSC} = \frac{1}{T_{d\,RSC}\left(s - j\omega_0\right) + 1} \tag{2.2}$$

$$\eta = \frac{s - j\omega_r}{s} \tag{2.3}$$

$$PI_{GSC} = K_{pGSC} + \frac{K_{iGSC}}{s - j\omega_0} \qquad PI_{RSC} = K_{pRSC} + \frac{K_{iRSC}}{s - j\omega_0} \tag{2.4}$$

The digital delay for PWM switching is commonly represented in the literature by $F_d = e^{-T_d s}$. This delay is relevant for stability analysis. The studies analyzing the eigenvalues of the DFIG use its polynomial approximation as a Pade equivalent (limited to a first or second order). During the development of the present work, a first order delay demonstrated to be sufficient to model the desired frequency range.

It is possible to obtain a small disturbance representation of Fig. 2.5 by analysis of the voltages Δv_{dq}^{RSC} and Δv_{dq}^{RSC} in the control diagrams in Fig. 2.6. This leads to expressions (2.5) and (2.6) respectively.

$$\begin{pmatrix} \Delta v_d^{RSC} \\ \Delta v_q^{RSC} \end{pmatrix} = F_d^{RSC} F_I \begin{pmatrix} PI_{RSC} & \left(L_{ls} + L_{lr}\right) \\ -\left(L_{ls} + L_{lr}\right) & PI_{RSC} \end{pmatrix} \begin{pmatrix} \Delta i_d^{RSC} \\ \Delta i_q^{RSC} \end{pmatrix} + F_d^{RSC} PI_{RSC} \begin{pmatrix} \Delta i_{d\,ref}^{RSC} \\ \Delta i_{q\,ref}^{RSC} \end{pmatrix} \tag{2.5}$$

$$\begin{pmatrix} \Delta v_d^{GSC} \\ \Delta v_q^{GSC} \end{pmatrix} = F_d^{GSC} F_I \begin{pmatrix} PI_{GSC} & L_f \\ -L_f & PI_{GSC} \end{pmatrix} \begin{pmatrix} \Delta i_d^{RSC} \\ \Delta i_q^{RSC} \end{pmatrix} + F_d^{GSC} PI_{GSC} \begin{pmatrix} \Delta i_{d\,ref}^{GSC} \\ \Delta i_{q\,ref}^{GSC} \end{pmatrix} \tag{2.6}$$

Expressions (2.5) and (2.6) can be rewritten as (2.7) and (2.8) respectively, so the terms $Z_{dq}^{RSC}\Delta i_{dq}^{RSC}$ and $Z_{dq}^{GSC}\Delta i_{dq}^{GSC}$ represent the voltage drops due to the internal impedance of the Thévenin equivalents of the converters, and the terms $K_{RSC}\Delta i_{dq\,ref}^{RSC}$ and $K_{GSC}\Delta i_{dq\,ref}^{GSC}$ correspond to the internal voltages of the Thévenin equivalents.

$$\Delta v_{dq}^{RSC} = Z_{dq}^{RSC} \Delta i_{dq}^{RSC} + K_{RSC} \Delta i_{dq\,ref}^{RSC} \tag{2.7}$$

$$\Delta v_{dq}^{GSC} = Z_{dq}^{GSC} \Delta i_{dq}^{GSC} + K_{GSC} \Delta i_{dq\,ref}^{GSC} \tag{2.8}$$

where:

$$Z_{dq}^{RSC} = F_d^{RSC} F_I \begin{pmatrix} PI_{RSC} & (L_{ls} + L_{lr}) \\ -(L_{ls} + L_{lr}) & PI_{RSC} \end{pmatrix} \qquad K_{RSC} = F_d^{RSC} PI_{RSC}$$

$$Z_{dq}^{GSC} = F_d^{GSC} F_I \begin{pmatrix} PI_{GSC} & L_f \\ -L_f & PI_{GSC} \end{pmatrix} \qquad K_{GSC} = F_d^{GSC} PI_{GSC}$$

Expressions (2.7) and (2.8) can be transformed from dq domain to positive-negative sequence domain pn using expressions (2.9) and (2.10) (SHALIL; PARSA, 2017). This procedure results in expressions (2.11) and (2.12).

$$v_{pn} = \begin{pmatrix} 1 & j \\ 1 & -j \end{pmatrix} v_{dq} \qquad i_{pn} = \begin{pmatrix} 1 & j \\ 1 & -j \end{pmatrix} i_{dq} \qquad i_{pn\,ref} = \begin{pmatrix} 1 & j \\ 1 & -j \end{pmatrix} i_{dq\,ref} \tag{2.9}$$

$$Z_{pn} = \begin{pmatrix} 1 & j \\ 1 & -j \end{pmatrix} Z_{dq} \begin{pmatrix} 1 & 1 \\ -j & j \end{pmatrix} \tag{2.10}$$

$$\Delta v_{pn}^{RSC} = Z_{pn}^{RSC} \Delta i_{pn}^{RSC} + K_{RSC} \Delta i_{pn\,ref}^{RSC} \tag{2.11}$$

$$\Delta v_{pn}^{GSC} = Z_{pn}^{GSC} \Delta i_{pn}^{GSC} + K_{GSC} \Delta i_{pn\,ref}^{GSC} \tag{2.12}$$

The elements from the Z_{dq} impedance matrix have a particular symmetry which enables a perfect decoupling of the positive and negative sequence impedance as in expression (2.13) due to the previous considerations (neglecting the PLL, DC bus and outer loop dynamics). This dissertation considers balanced conditions, therefore, only the positive sequence element $a - jb$ of expression (2.13) is of interest. This last consideration results in expressions (2.14) and (2.15) for the impedances of the RSC and the GSC respectively.

$$Z_{pn} = \frac{1}{2} \begin{pmatrix} 1 & j \\ 1 & -j \end{pmatrix} \begin{pmatrix} a & b \\ -b & a \end{pmatrix} \begin{pmatrix} 1 & 1 \\ -j & j \end{pmatrix} = \begin{pmatrix} a - jb & 0 \\ 0 & a + jb \end{pmatrix} \tag{2.13}$$

$$Z_{RSC} = (PI_{RSC} - j(L_{ls} + L_{lr}))F_I F_d^{RSC} \tag{2.14}$$

$$Z_{GSC} = (PI_{GSC} - jL_f)F_I F_d^{GSC} \tag{2.15}$$

Finally, the small disturbance Thévenin equivalents in phase domain for the current controlled voltage sources of Fig. 2.5 are described by expressions (2.16) and (2.17).

$$\Delta v^{RSC} = Z^{RSC}\Delta i^{RSC} + K_{RSC}\Delta i^{RSC}_{ref} \tag{2.16}$$

$$\Delta v^{GSC} = Z^{GSC}\Delta i^{GSC} + K_{GSC}\Delta i^{GSC}_{ref} \tag{2.17}$$

Fig. 2.7 presents the equivalent small signal DFIG model. From this point on, the converters are studied as frequency dependent Norton equivalents with current sources as described in expression (2.18). Note that the Norton equivalent of the RSC was scaled by a factor η corresponding to the slip of the induction machine.

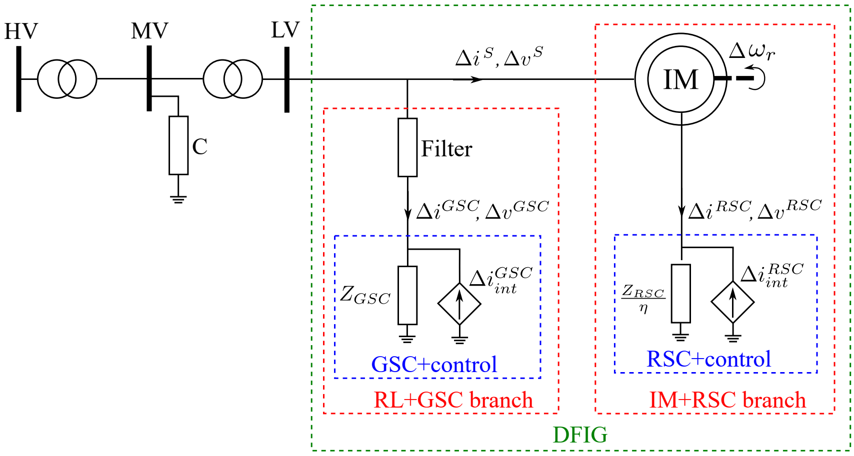

Figure 2.7 – Small signal model of DFIG with a wind turbine

$$\Delta i^{RSC}_{int} = \left(\eta\frac{K_{RSC}}{Z_{RSC}}\right)\Delta i^{RSC}_{ref} \qquad \Delta i^{GSC}_{int} = \left(\frac{K_{GSC}}{Z_{GSC}}\right)\Delta i^{GSC}_{ref} \tag{2.18}$$

In this small signal model, the variation of current references (Δi^{RSC}_{ref} and Δi^{GSC}_{ref}) can be neglected because these currents are the outputs of outer control loops which are much slower than the inner current control. In fact, the literature review in Chapter 1 and the simulation show the reference currents provided by the outer control loops do not present high-frequency distortions due to the presence of measurement filters. Therefore, the reference currents can be neglected for frequencies up to 1500 Hz (i.e., $I^{RSC}_{int} \approx 0$, $I^{GSC}_{int} \approx 0$).

By putting together the previous results, the DFIG and the grid equivalent at PCC can be analyzed as a set of impedances above the fundamental frequency with Fig. 2.8.

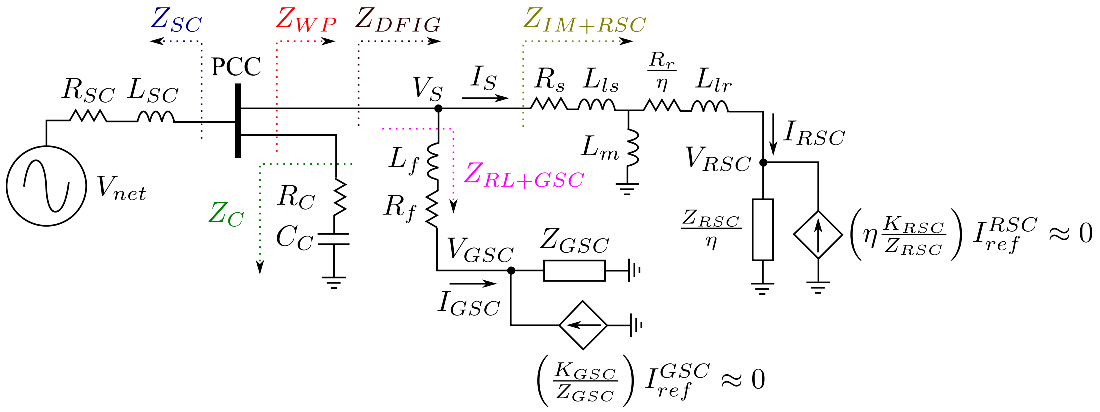

Figure 2.8 – Equivalent impedance model of the DFIG for high-frequency at PCC

The contribution of the converters to the equivalent impedance model of the DFIG is described by the terminal voltages and the currents as the transfer functions in expression (2.19) (see expressions (2.14) and (2.15)).

$$\frac{Z_{RSC}}{\eta} = \frac{V_{RSC}}{I_{RSC}} \qquad Z_{GSC} = \frac{V_{GSC}}{I_{GSC}} \tag{2.19}$$

The impedances for the IM+RSC branch, the RL+GSC branch, the DFIG and the wind park including its reactive power compensation bank C_C are given as follows:

$$Z_{RL+GSC} = R_f + L_f s + Z_{GSC} \tag{2.20}$$

$$Z_{IM+RSC} = R_s + sL_s + \left((sL_m)^{-1} + \left(\frac{R_r + Z_{RSC}}{\eta} + sL_r\right)^{-1}\right)^{-1} \tag{2.21}$$

$$Z_{DFIG} = \left({Z_{RSC+IM}}^{-1} + {Z_{GSC+RL}}^{-1}\right)^{-1} \tag{2.22}$$

$$Z_{WP} = \left({Z_{DFIG}}^{-1} + {Z_C}^{-1}\right)^{-1} \tag{2.23}$$

where the s sub-index denotes the stator, r the rotor, m the magnetization and f the filter. As the control system is designed with pu values, its mathematical expression yields impedance terms in pu. Finally, the analytic expressions for the two branches of the DFIG's impedance can be obtained by isolating the transfer functions of expression (2.24).

$$Z_{IM+RSC} = V_S/I_S \qquad Z_{RL+GSC} = V_S/I_{GSC} \tag{2.24}$$

2.3 Validation of the DFIG's impedance model

Based on the impedance diagram of Fig.2.8 (which represents a WP as an aggregated unit at PCC), the impedances of the IM+RSC and RL+GSC branches of the DFIG (see expression (2.24)) can be obtained with a measurement-based approach with the effects of small disturbances at any frequency f at machine terminals, measuring the change in voltage δV and current δI.

These disturbances consist of a small sinusoidal voltage component of frequency f at the grid equivalent V_{net} (1 % or 2 % of the fundamental), which can be isolated with FFT decomposition. Two sets of voltage and current measurements (V_1, I_1) and (V_2, I_2) obtained at time instants with different grid distortion levels can be used as in expression (2.25) (XU *et al.*, 2001).

$$Z(f) = \frac{\delta V}{\delta I} = \frac{V_2(f) - V_1(f)}{I_2(f) - I_1(f)} \tag{2.25}$$

Fig. 2.9 presents equivalent impedance estimates obtained from an EMT simulation where a 100 MVA DFIG-based wind park is modeled in detail. The red markers correspond to the calculated values from the measurements using two different conditions of grid harmonic pollution as explained previously (1 and 2 % of the fundamental), and the blue lines correspond to expressions (2.21), (2.20) and (2.22) from the analytic model.

The results demonstrate a good match between the detailed EMT simulation and the analytic equivalent impedance model. The differences in the resistances are due to the lower signal-to-noise ratio. Nevertheless, the tendency of the mean value matches the analytic model. This is further confirmed by using the average converter model as in Fig. 2.10.

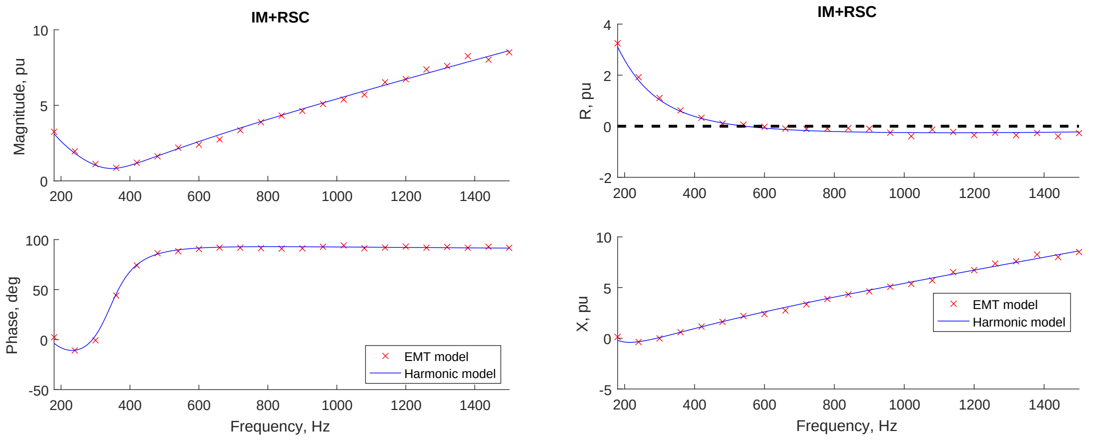

(a) Z_{IM+RSC} magnitude and angle (b) Z_{IM+RSC} resistance and reactance

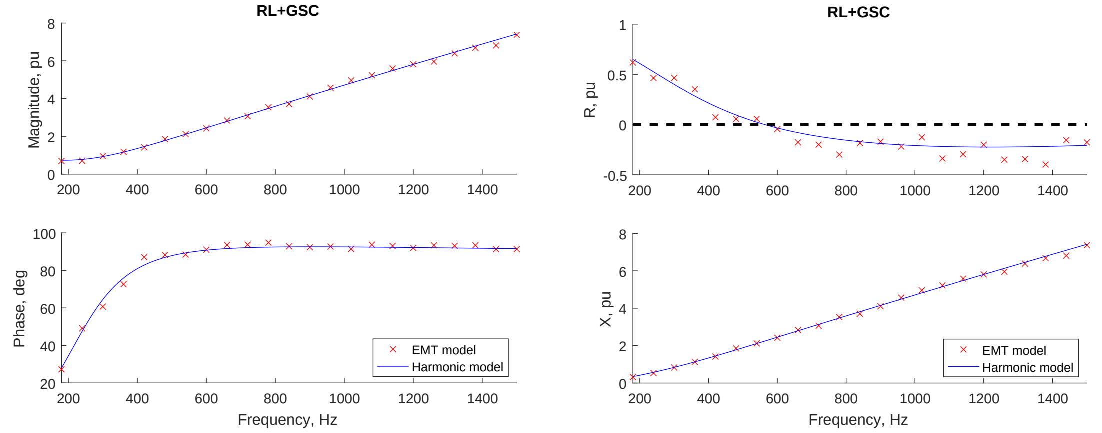

(c) Z_{RL+GSC} magnitude and angle (d) Z_{RL+GSC} resistance and reactance

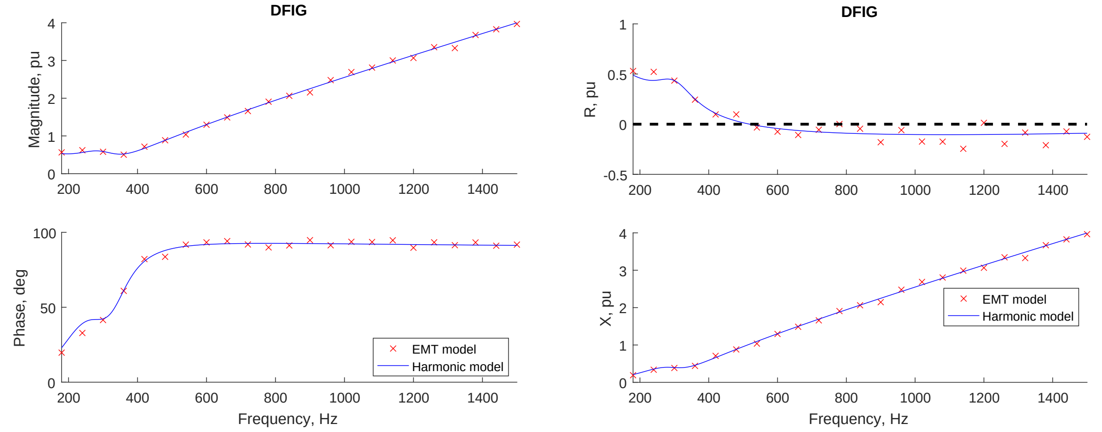

(e) Z_{DFIG} magnitude and angle (f) Z_{DFIG} resistance and reactance

Figure 2.9 – DFIG impedances from EMT simulation, switched converter model

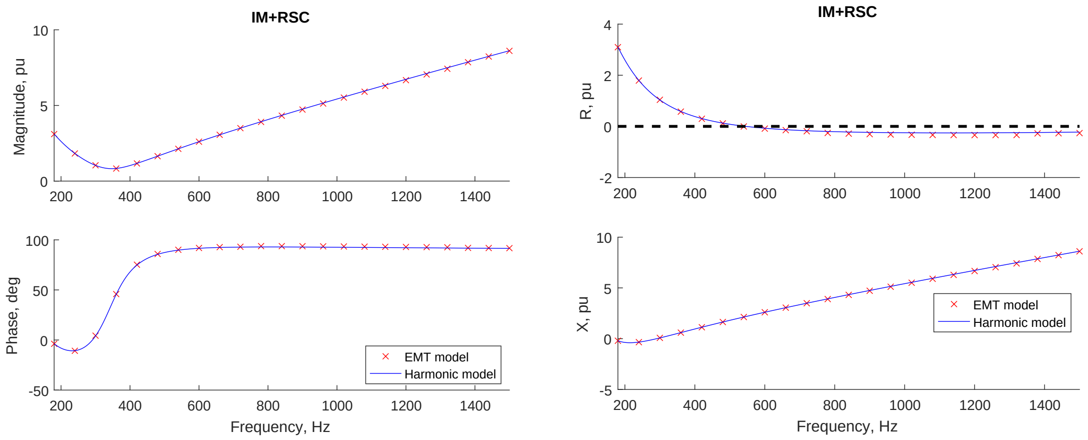

(a) Z_{IM+RSC} magnitude and angle (b) Z_{IM+RSC} resistance and reactance

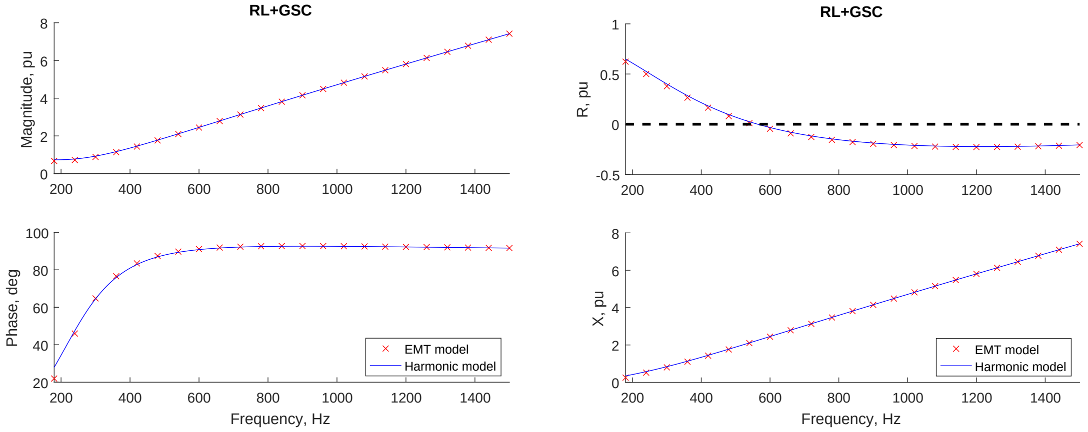

(c) Z_{RL+GSC} magnitude and angle (d) Z_{RL+GSC} resistance and reactance

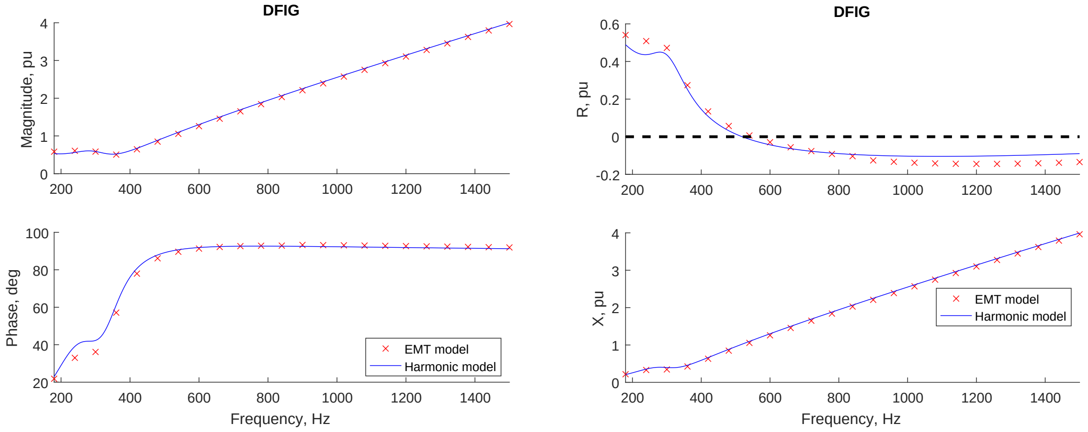

(e) Z_{DFIG} magnitude and angle (f) Z_{DFIG} resistance and reactance

Figure 2.10 – DFIG impedances from EMT simulation, average converter model

The parameters of the equivalent impedance model to build for Fig. 2.9 and Fig. 2.10 are detailed in Table 3 of the Appendix A. Note the negative resistance values of the VSC's. This characteristic is further explored for stability assessment in chapter 3.

2.4 High-frequency resonance study with DFIG impedance model

The impedance model of the DFIG can be used to obtain simplified analytic expressions and study different characteristics of the resonance such as the amplification and frequency value. The present section first defines expressions for the amplification in terms of the impedances of the circuit. Later on, it studies the effect of the control and grid parameters on the amplification and the resonance frequency.

2.4.1 Amplification at PCC

The expressions to calculate the impedance of the grid equivalent and the compensation capacitance are given by (2.27) and (2.29) respectively. It is useful to express these impedances in terms of the short-circuit and reactive power compensation ratios to facilitate the representation of multiple scenarios of different parameter combinations in a single plot. This is expanded in the sensitivity analysis of section 2.4.3.

$$L_{SC} = \frac{{V_{\substack{base\\PCC}}}^{2}}{\omega_0 \left(S_{SC}/S_{WP}\right) S_{WP}} \frac{1}{\sqrt{1+\left(X/R\right)^{-2}}} \qquad R_{SC} = \frac{\omega_0 L_{SC}}{(X/R)} \tag{2.26}$$

$$Z_{SC} = R_{SC} + sL_{SC} \tag{2.27}$$

$$C_C = \frac{\left(Q_C/S_{WP}\right) S_{WP}}{\omega_0 {V_{\substack{base\\PCC}}}^{2}} \tag{2.28}$$

$$Z_C = \frac{1}{sC_C} \tag{2.29}$$

The expression that describes the amplification of signals from the grid at the PCC is given by (2.30). If the denominator of the expression becomes smaller (this occurs at frequencies where the signs of the impedances oppose each other) the impedances tend to cancel each other out, therefore, the amplification becomes larger. The validation of the amplification of grid harmonic distortion components is presented in Fig. 2.11 for a single DFIG and a WP equivalent.

$$A = \frac{Z_{WP}}{Z_{SC} + Z_{WP}} \tag{2.30}$$

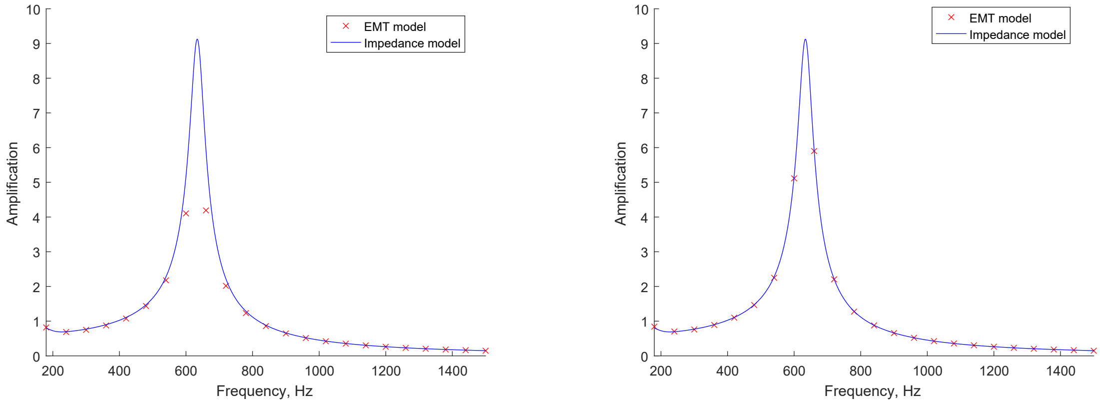

(a) $(S_{WP}, Q_C, S_{SC}) = (2, 0.4, 30)$ MVA

(b) $(S_{WP}, Q_C, S_{SC}) = (100, 20, 1500)$ MVA

Figure 2.11 – Amplification plot of harmonic distortion at PCC

A good correspondence between the model and the simulation can be observed. An interesting result is that the amplification plot is the same for different WP capacities if the short-circuit ratio $S_{SC}/S_{WP} = 15$ and reactive power compensation ratio $Q_C/S_{WP} = 0.2$ remain constant, as in Fig. 2.11. The peaks of the amplification plot inform the exact location of resonance frequencies and their total amplification.

2.4.2 Effect of the WP feeder impedance

The DFIG impedance model was further evaluated considering a WP with line and transformer impedances using the circuit in Fig. 2.12. This circuit has four symmetrical overhead feeders, each with a DFIG equivalent. The reactive power compensation bank was modeled as a bulk capacitor for the entire park near the PCC (red impedance) and included as part of the WP impedance.

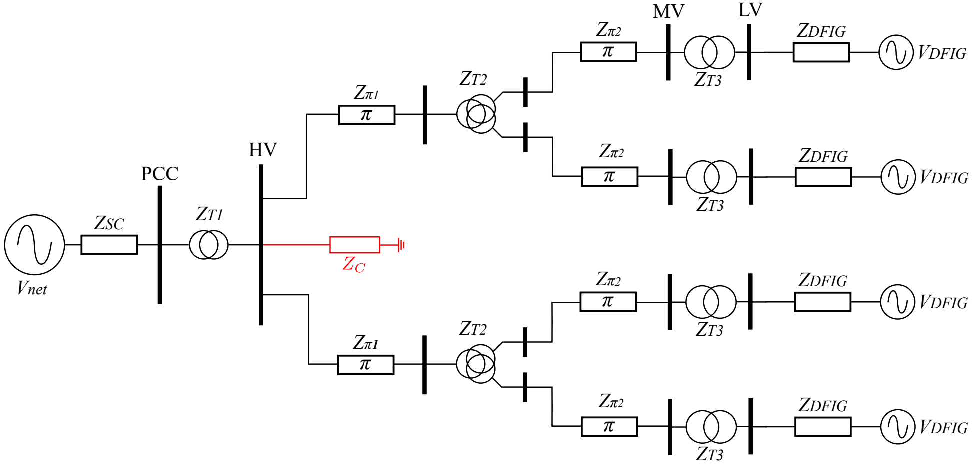

Figure 2.12 – Detailed WP with non-ideal feeders, bulk compensation

This study was conducted to evaluate the effects of the additional WP components in the impedance profile at PCC. The WP feeder parameters (modified from (EBRAHIMZADEH *et al.*, 2018)) are available in Table. 4 of the Appendix A. The reactive power compensation to WP capacity ratio was set to $Q_C/S_{WP} = 0.2$.

The results of the impedance validation at the PCC of the detailed WP are presented in Fig. 2.13(a), and the respective amplification diagram in Fig. 2.13(b). The results from Fig. 2.13 include the impedances of the feeders and the transformers of the wind park.

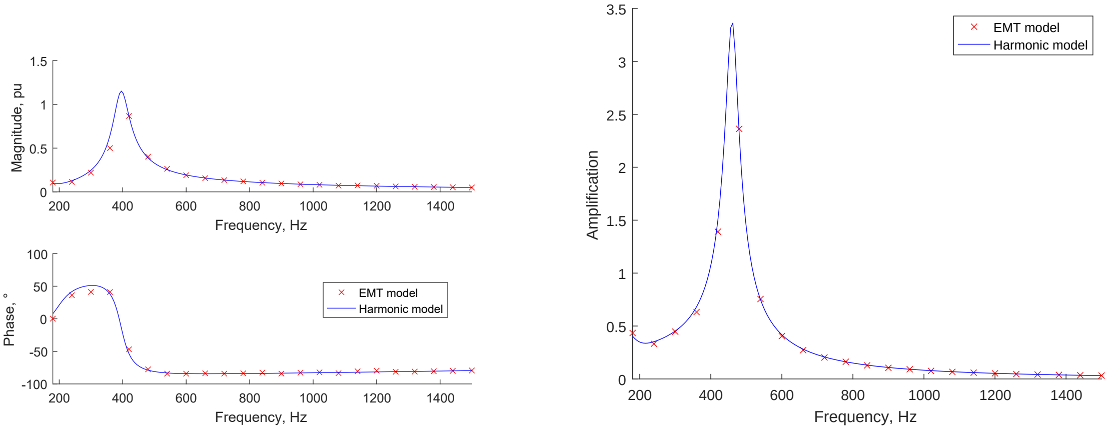

(a) Impedance at PCC (b) Amplification at PCC

Figure 2.13 – Detailed WP equivalent impedance at PCC and amplification

As observed from the studies, the capacitances associated with the pi model of the overhead lines in the circuit did not lead to additional resonances in the studied range of frequencies due to their small value. Therefore, the capacitances of short overhead lines can be neglected and only the reactive power compensation banks need to be included in the model. Underground or submarine cables with considerable lengths may present important capacitances that should be included in the impedance model as these are typically 10 to 30 times greater than those from an overhead line with simmilar capacity.

2.4.3 Sensitivity of resonance frequency and maximum amplification

The resonance frequency and its respective amplification value can be obtained from the peaks of the amplification plot. If only one capacitance is relevant in the studied frequency range (as it was demonstrated in section (2.4.2)), then only one resonance peak will appear in the amplification plot as different capacitors do not oscillate coherently (XU *et al.*, 2005), unless in perfectly symmetric conditions.

In order to focus in the most influential parameters of the model, it is interesting to observe how the peak value changes with the variations of parameters in the grid equivalent and the impedance model of the DFIG.

The reactive power compensation ratio Q_C/S_{WP} and the short-circuit ratio S_{SC}/S_{WP} were used to perform the sensitivity analysis. The arrays for the parametric sweep are detailed as follows:

- S_{SC}: [10:10:100,200:100:1000,1500:500:10000] MVA

- S_{WP}: [2:1,10,20:10:100,150:50:1000] MVA
- Q_C/S_{WP}: [0.05,0.1,0.2,0.5,0.8]

Only those combinations with $S_{SC} > S_{WP}$ were evaluated. The base scenario is given in Fig. 2.14. Note the clearly defined tendency by using the ratios to represent the results (this is further explored in section (2.5)). Also note that a change of tendency in the amplification occurs when the resonance frequency is higher than the maximum evaluated frequency (1500 Hz). This happens because the frequency that yields the maximum amplification in such study range corresponds to the largest evaluated frequency (i.e., 1500 Hz).

This change of tendency is more evident for low ratios such as $Q_C/S_{WP} = 0.05$, as the capacitance values lead to resonance frequencies higher than the largest evaluated frequency.

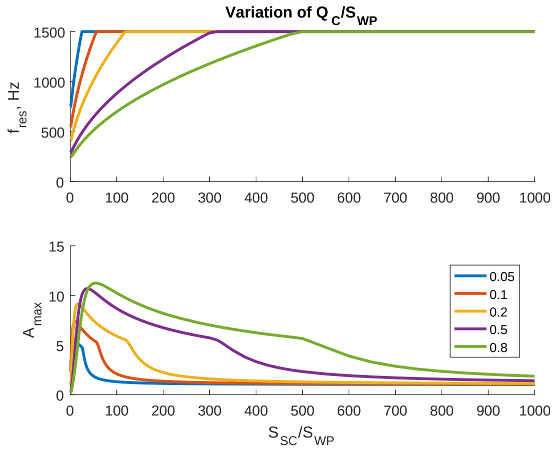

Figure 2.14 – Resonance frequency and maximum amplification of base scenario

The results of the sensitivity study can be seen in Fig. 2.15. The most influential variables correspond to the grid's X/R ratio and the current measurement filter cutoff frequency f_I for certain combinations (low S_{SC}/S_{WP} and certain Q_C/S_{WP} ratios) as observed in Fig. 2.15. These variables have direct influence over the circuit's resistances, meaning that the lower the damping, the higher the amplification values at resonance.

It can be observed in Fig. 2.15(a) how the amplification at resonance can reach very large values, specially for small reactive power compensations, where the risk is higher if the current filter bandwidth is low. This can be further appreciated with the zoomed tendency in Fig. 2.15(b).

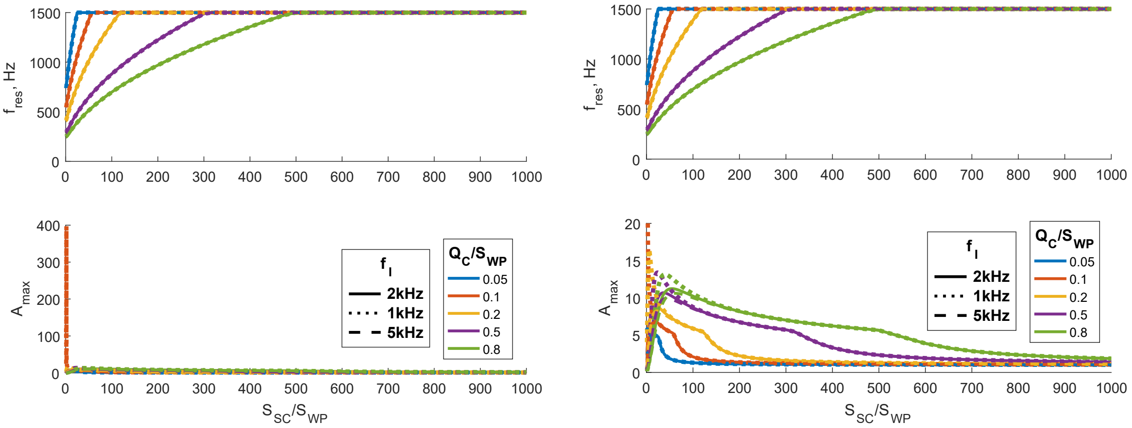

(a) Sensitivity to filter cutoff frequency f_I (b) Sensitivity to filter cutoff frequency f_I, zoom

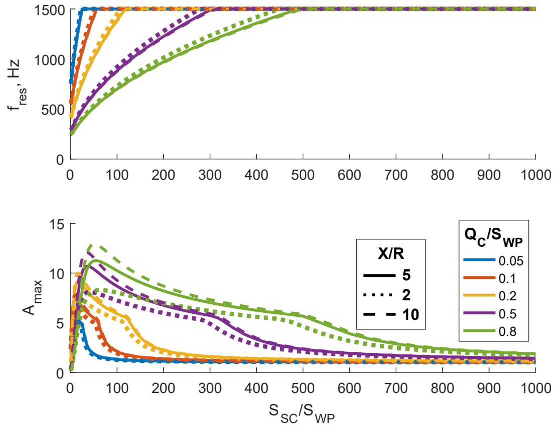

(c) Sensitivity to grid's X/R ratio

Figure 2.15 – Sensitivity analysis of f_{res}, A_{max}, most influential variables

The results in Fig. 2.16 show that the proportional gains of the controllers only influence the amplification, and most visibly for large Q_C/S_{WP} and low S_{SC}/S_{WP} (weak network) ratios. Additionally, the switching frequencies that define the control delays and the measurement filter cutoff frequency affect the maximum amplification for low S_{SC}/S_{WP} ratios.

As observed in Fig. 2.16, there is no significant change in the resonance frequency for any of the less influential variables.

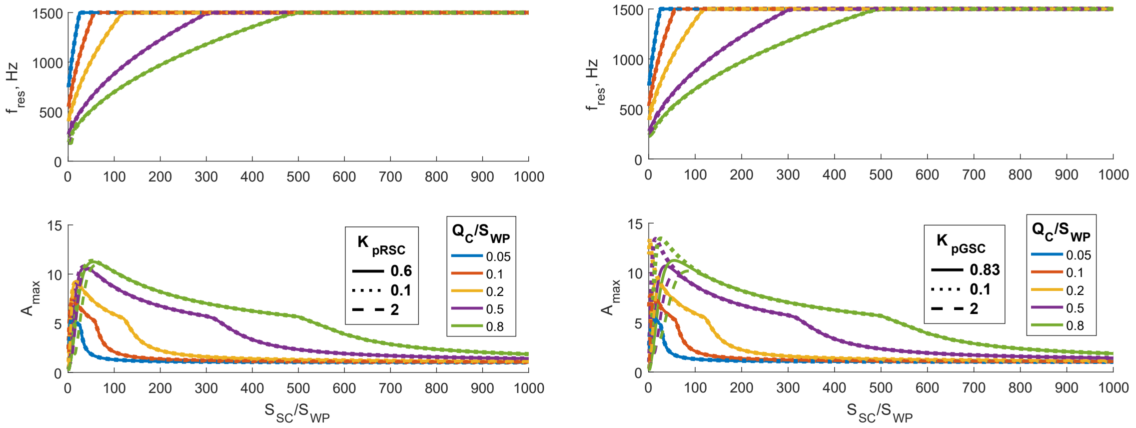

(a) Sensitivity to RSC proportional gain K_{pRSC} (b) Sensitivity to GSC proportional gain K_{pGSC}

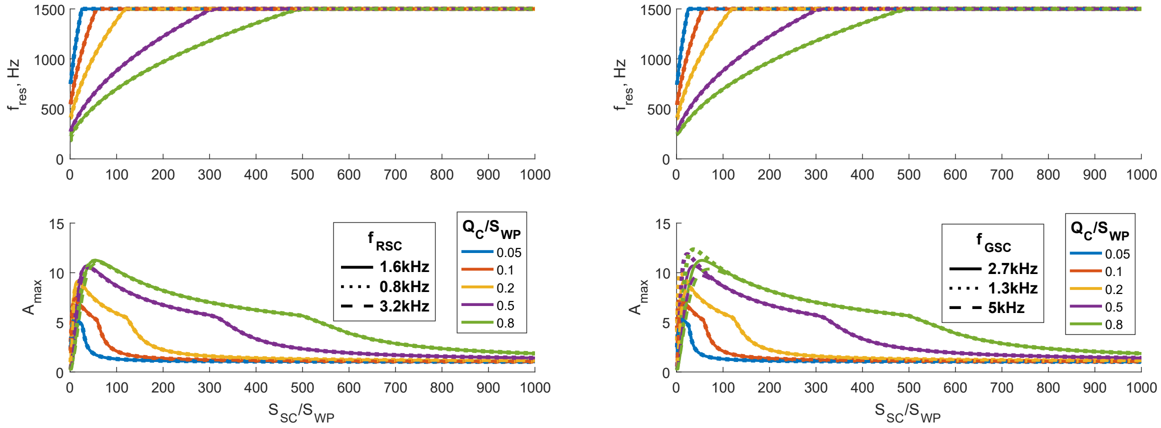

(c) Sensitivity to RSC switching frequency f_{RSC} (d) Sensitivity to GSC switching frequency f_{GSC}

Figure 2.16 – Sensitivity analysis of f_{res}, A_{max}, less influential variables

The integral gains have little to no effect as seen in Fig. 2.17. To justify the previous results involving the control gains of the converters, recall expressions (2.14), (2.15) and consider the part of the converter impedance associated with the PIs as in expression (2.31):

$$Z_{PI} \propto K_P + \frac{K_I}{s} \tag{2.31}$$

where the real component of the impedance is associated to the proportional gain K_P, and the imaginary component associated to the integral gain K_I (which in addition becomes smaller with larger frequencies). The real part of the converter impedance dominates over the imaginary part, therefore, the proportional gain of the converters has a higher influence in the DFIG impedance.

The real part of the converter impedance can be seen as a resistance, which explains why it only has important effects in the value of amplification at resonance and no important influence in the resonance frequency. Given the values of the present case, the imaginary part of the induction machine impedance dominates over the RSC and the real part of the GSC impedance dominates over the RL filter.

As seen in Fig. 2.17, the rotor speed was also not influential as the mechanical variables affect mostly frequencies lower than the fundamental, while resonances due to shunt capacitors occur at higher frequencies.

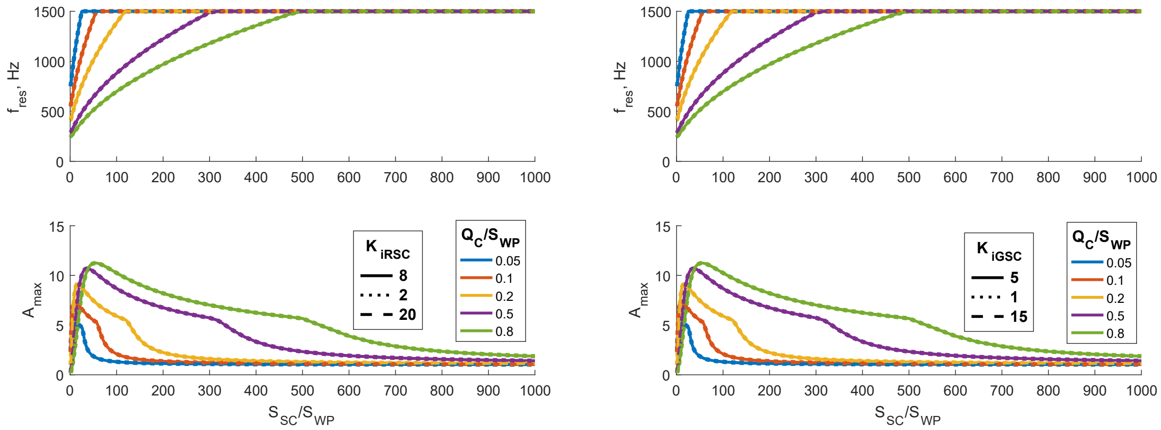

(a) Sensitivity to RSC integral gain K_{iRSC} (b) Sensitivity to GSC integral gain K_{iGSC}

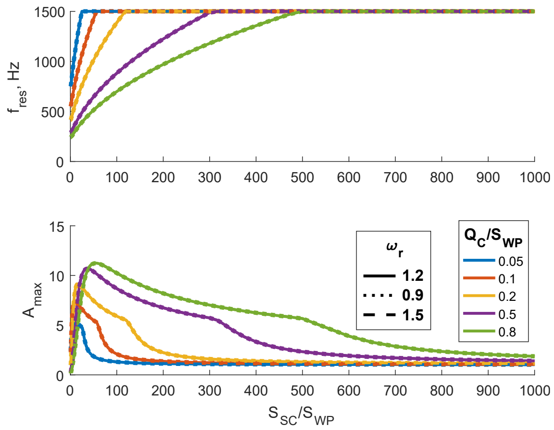

(c) Sensitivity to rotational speed ω_r

Figure 2.17 – Sensitivity analysis of f_{res}, A_{max}, non-influential variables

2.5 Analytic determination of resonance frequency

Based on the previous sensitivity analysis and the reasoning of the real and imaginary parts of the converter impedance from expression (2.31), the inductances and capacitances of the circuit have the highest influence in the resonance frequency. If all resistances and converter impedances are neglected, the circuit becomes a pure LC equivalent at the PCC as in Fig. 2.18.

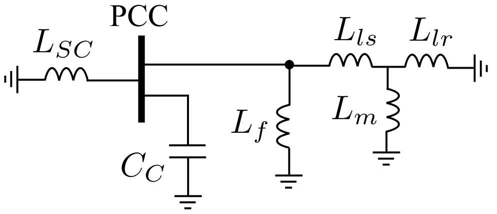

Figure 2.18 – Simplified LC circuit at PCC for resonance frequency determination

The only relevant capacitive element C_{PCC} would be given by the reactive power compensation C_C and the inductive element L_{PCC} corresponds to a composition of the DFIG and the grid inductances. Therefore, the resonance frequency of the resulting circuit can be described using a expression (2.32).

$$f_{res} = \frac{1}{2\pi\sqrt{L_{PCC}C_{PCC}}} \tag{2.32}$$

where:

$$L_{PCC} = \left(L_{SC}^{-1} + L_{DFIG}^{-1}\right)^{-1} \tag{2.33}$$

The equivalent inductance of the DFIG is described by (2.34) (in terms of the induction machine (IM) and RL filter parameters), the grid inductance is described by (2.35) (in terms of the short-circuit capacity and X/R ratio), and the capacitance by (2.36).

$$L_{DFIG} = \left(\left(L_s + \left(L_r^{-1} + L_m^{-1}\right)^{-1}\right)^{-1} + L_f^{-1}\right)^{-1} \tag{2.34}$$

$$L_{SC} = \frac{{V_{\underset{PCC}{base}}}^{2}}{S_{SC}\omega_0}\frac{1}{\sqrt{1+(X/R)^{-2}}} \tag{2.35}$$

$$C_{PCC} = \frac{\left(Q_C/S_{WP}\right)S_{WP}}{\omega_0 {V_{\underset{PCC}{base}}}^{2}} \tag{2.36}$$

The approximate value of the resonace frequency corresponds to expression (2.37). This expression was obtained by introducing (2.34) and (2.35) into (2.33), and then (2.33) and (2.36) into (2.32).

Using expression (2.37), it is possible to determine the approximate value of the resonance frequency in terms of the ratios of the circuit and the pu value of the DFIG inductance in machine basis (2.38). Therefore, the expression is generic for any combination of WP capacity, reactive power compensation, and short-circuit capacity.

$$f_{res} \approx f_0\sqrt{\left(Q_C/S_{WP}\right)^{-1}\left(\sqrt{1+(X/R)^{-2}}\left(S_{SC}/S_{WP}\right) + {L_{DFIG_{pu}}}^{-1}\right)} \tag{2.37}$$

$$L_{DFIG\,pu} = L_{DFIG} \frac{S_{WP}\omega_0}{{V_{base}}_{PCC}^{\;2}} \tag{2.38}$$

The previous expression was validated using a frequency sweep of the impedance model without any simplifications. The results of the validation are presented in Fig. 2.19(a) for several reactive power compensation levels (0.05, 0.1, 0.2, 0.5, and 0.8 of the rated WP capacity). With the approximate resonance frequency, it is also possible to calculate the maximum amplification directly using (2.30) instead of performing a frequency sweep. The respective validation results for the amplification calculated at the approximate resonance frequency are presented in Fig. 2.19(b).

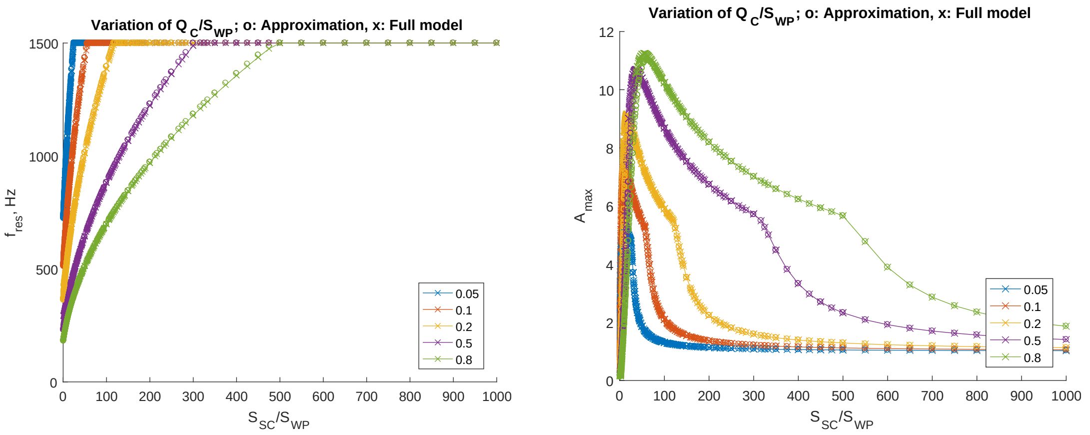

(a) Resonance frequency

(b) Amplification

Figure 2.19 – Resonance frequency and amplification approximation results

The upper saturation value in the validation results represents the highest considered resonance frequency (1500 Hz). It can be observed that the approximation is very accurate, where low Q_C/S_{WP} ratios lead to high-frequency resonances with small variations of the S_{SC}/S_{WP} ratio. Another important observation is that small S_{SC}/S_{WP} ratios (weak network conditions) also lead to resonance at frequencies close to those of the background distortions typically found in the grid.

Expression (2.37) can be used as a quick reference to obtain the resonance frequency of a WP configuration in terms of readily available parameters for the utility. It will also be useful in the developments of the following chapters of this dissertation.

2.6 Summary

This chapter has obtained and validated an equivalent impedance model for DFIG-based wind parks at a frequency range from 180 to 1500 Hz, which is below the switching frequency of both the rotor-side and grid-side converters. The main findings of are:

- RSC and GSC behave as a linear device in the frequency range of study. Therefore, they can be modeled as an impedance. This impedance is obtained by considering only the inner current control loops (which have fast dynamics). External control loops and the PLL have slower dynamics and can be assumed to be ideal in this study.
- The equivalent resistance of the RSC and GSC can become negative at some high frequencies due to the phase angle shift introduced by measurement filters and the time delays introduced by the control circuit. The relationship of this characteristic with the stability of the system will be further addressed in the following chapter.
- High-frequency resonances can take place between the shunt capacitor of the wind park and the inductive characteristic of the utility grid. The resonance frequency can be estimated analytically by using only the utility grid inductance, the reactive power compensation capacitance and the DFIG inductances.

3 High-frequency stability analysis

The previous chapter confirmed a range of frequencies where the DFIG impedance model presents negative resistance (i.e., negative damping). A clear understanding of the variables that influence this negative resistance characteristic is important to study the system stability at resonance frequencies. Initially, this chapter studies the influence of the converter control on the negative resistance value. Later on, using the impedance model of the DFIG, it explains the mechanism to enter high-frequency unstable resonance conditions.

To assess the stability for different combinations of WP capacity, reactive power compensation, and short-circuit level of the grid, this chapter proposes a chart relating the short-circuit ratio and the reactive power compensation ratio. The chart defines a risk region built from the combinations leading to unstable resonance, which allows for a fast and simplified assessment of the phenomenon. The chart is developed with the equivalent impedance model and validated with numerous EMT simulations.

3.1 Unstable resonance in DFIG-based wind parks

According to (SONG *et al.*, 2017), high-frequency unstable resonance can occur in DFIG-based wind parks. This is confirmed by the results of the waveforms in Fig. 3.1, obtained with EMT simulation at the PCC of a DFIG-based WP of $S_{WP} = 100$ MVA after connecting an additional reactive power compensation stage of $Q_C = 10$ MVA at 1 s. The parameters of the grid are $X/R = 10$ and $S_{SC} = 3000$ MVA.

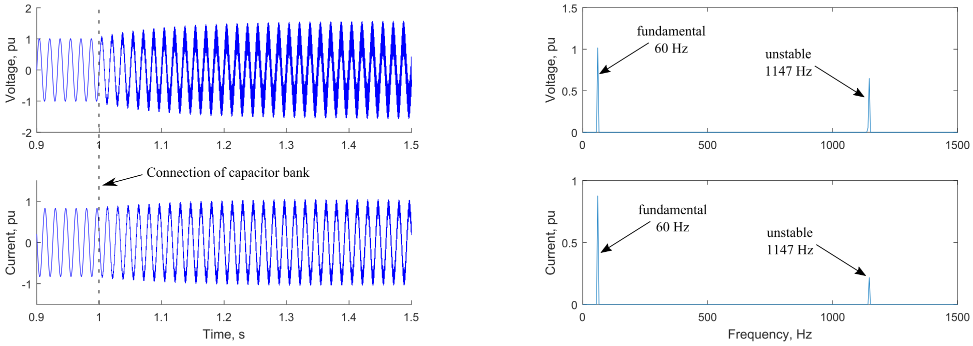

(a) Voltage and current waveforms

(b) FFT spectrum of the last 12 fundamental cycles

Figure 3.1 – Unstable resonance (1147 Hz) due to capacitor switching

At unstable resonance, the DFIG sustains an additional voltage component in the frequency of resonance without external excitation. Such condition can also occur after connecting a group of generators, faults or grid reconfigurations, amongst other actions which change the impedance of the DFIG or the grid.

Unstable resonance appears when a natural oscillation mode of the system presents positive feedback through the control loop of the converters. This is associated with a phase shift of the controlled signal due to filtering, delays in the feedback loop and the gains of the current controllers. This positive feedback defines the negative damping characteristic of the power electronics converters of the DFIG, hence, the importance of studying the behavior of the resistive part of the resulting impedance.

A large number of combinations between grid and wind park parameters may lead to high-frequency unstable resonances. Therefore, using an EMT simulation-based approach to study this phenomenon is not viable. In order to facilitate the assessment of multiple scenarios of high-frequency unstable resonance in DFIG-based wind parks, the following sections present a practical chart that can be used to identify the risk of instability without the need to run any simulation.

3.2 Visualization of the negative resistance and sensitivity to converter control

Impedance angles greater than |90°| imply negative resistance, however, this is not clear in the Bode plot representation of the DFIG impedance as in the diagrams of the left column of Fig. 3.2. On the other hand, the plots in the right column of Fig. 3.2 allow for a better visualization of the negative resistance by separating the real and imaginary components.

The results in Fig. 3.2 present the impedance for the each of the branches of the DFIG. It can be observed that the negative resistance interval starts near 600 Hz for both converter branches, but the upper boundary of the negative resistance interval is located at a much higher frequency than the range considered in the present study (180 Hz to 1500 Hz).

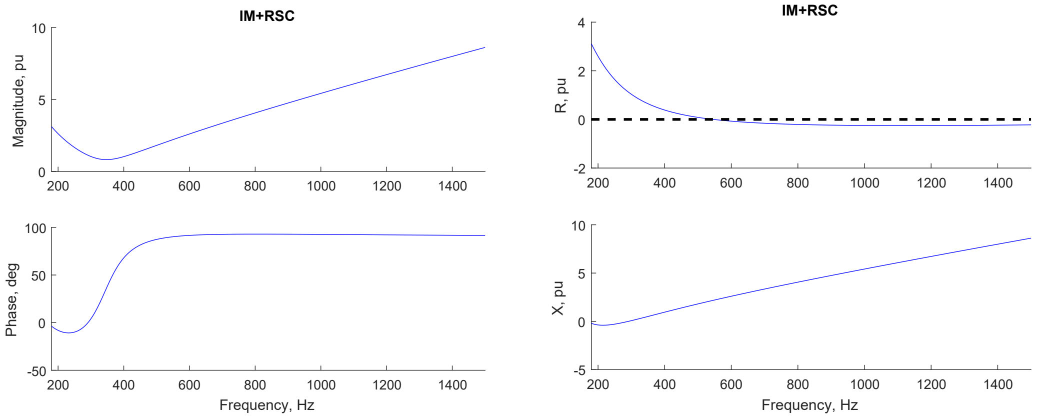

(a) Z_{IM+RSC} magnitude and angle (b) Z_{IM+RSC} resistance and reactance

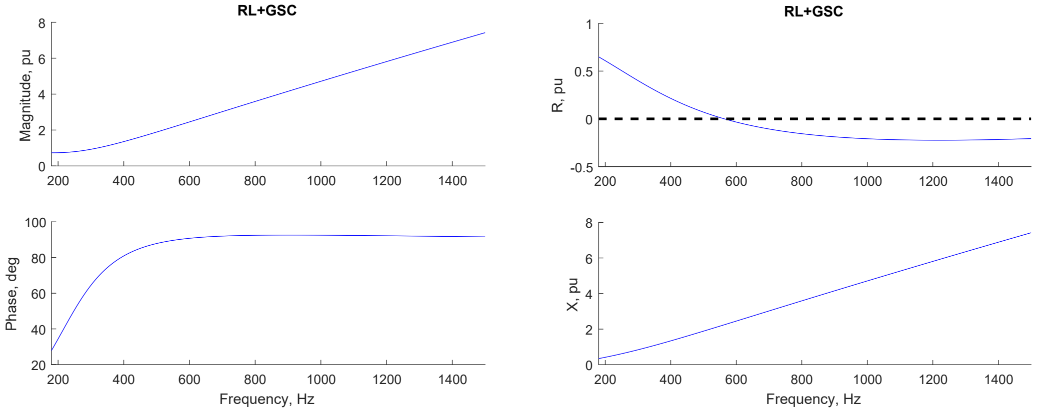

(c) Z_{RL+GSC} magnitude and angle (d) Z_{RL+GSC} resistance and reactance

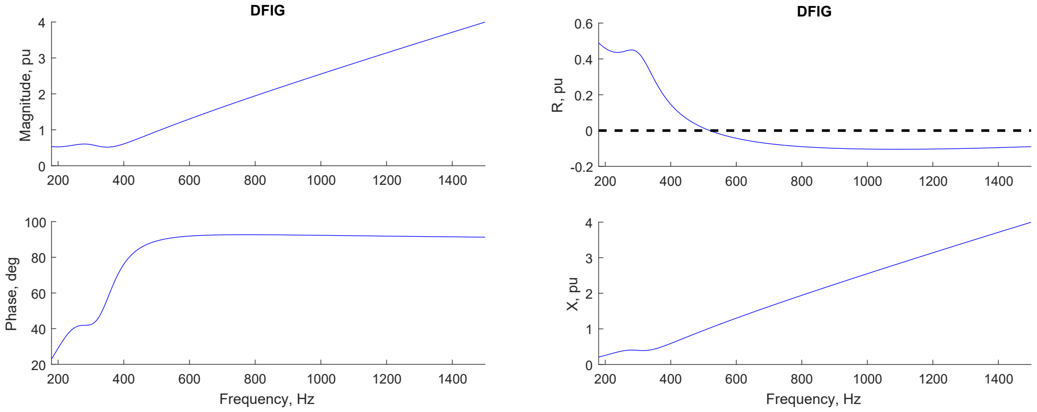

(e) Z_{DFIG} magnitude and angle (f) Z_{DFIG} resistance and reactance

Figure 3.2 – DFIG impedances, magnitude and angle vs resistance and reactance

The negative resistance of the DFIG is a characteristic that depends on the control parameters of the converters (measurement and control delays, as well as the control gains). The grid has no influence over it. Therefore, the resistance is analyzed in terms of: the measurement filter cutoff frequency f_I; the machine rotational speed ω_r; the switching frequencies of the RSC and GSC f_{RSC} and f_{GSC}; and the current control loop gains K_{pRSC}, K_{iRSC}, K_{pGSC}, K_{iGSC}.

The results of the sensitivity study are presented in pu of machine basis. The non-influential variables are detailed in Fig. 3.3. The integral gains have no significant effect in the resistance as their contribution is inversely proportional to the frequency. As for the rotational speed effects, the resistance associated with the rotor slip is only partially affected at frequencies near the fundamental. These variables have no influence in the frequencies with negative resistance.

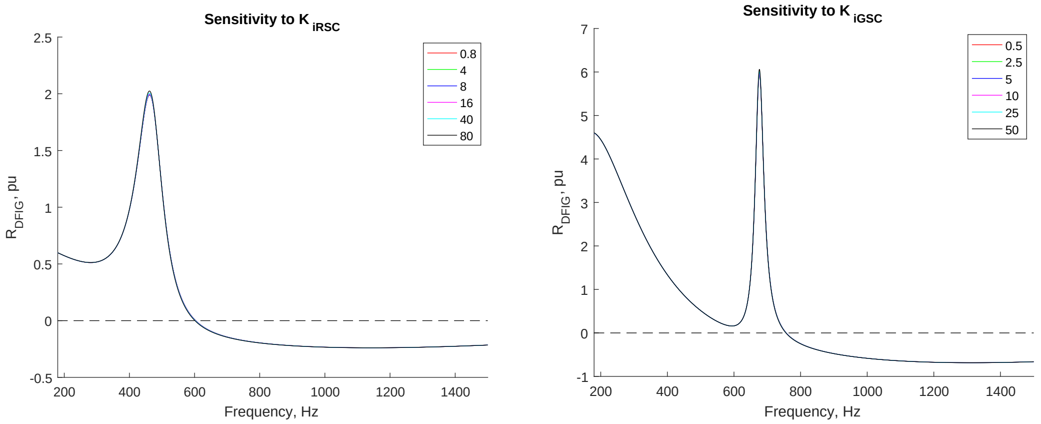

(a) Sensitivity to RSC integral gain K_{iRSC}

(b) Sensitivity to GSC integral gain K_{iGSC}

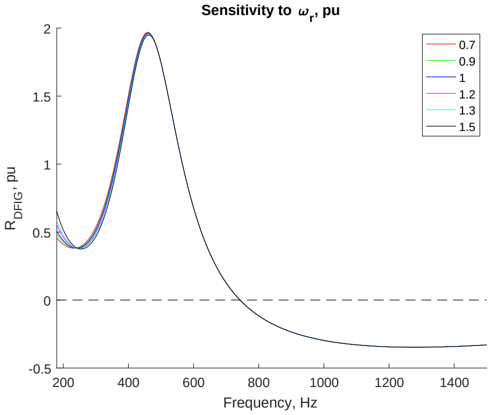

(c) Sensitivity to rotational speed ω_r

Figure 3.3 – Sensitivity analysis of R_{DFIG}, non-influential variables

The variables with significant influence are presented in Fig. 3.4.

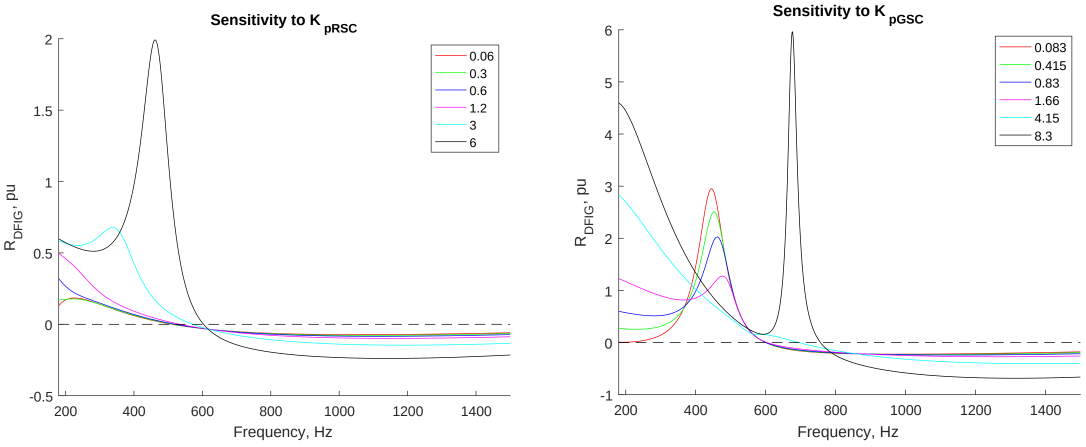

(a) Sensitivity to proportional gain of RSC K_{pRSC}

(b) Sensitivity to proportional gain of GSC K_{pGSC}

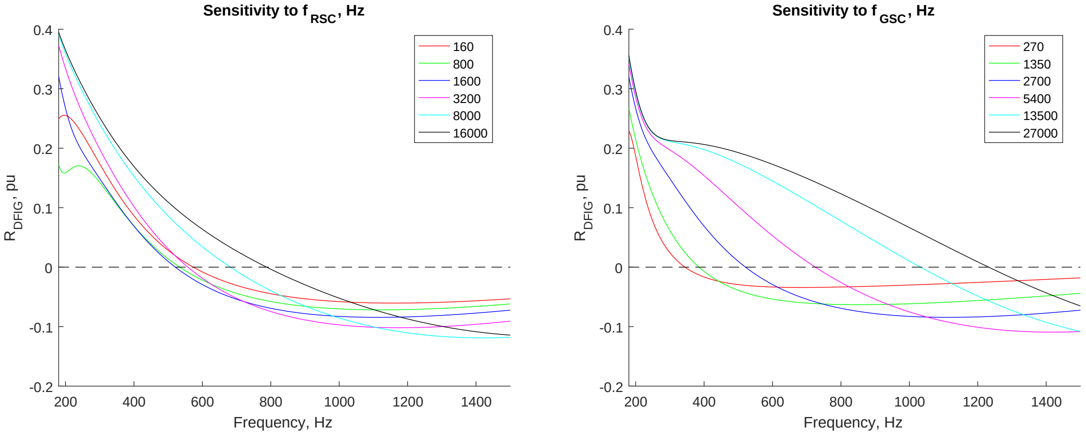

(c) Sensitivity to RSC switching frequency f_{RSC}

(d) Sensitivity to GSC switching frequency f_{GSC}

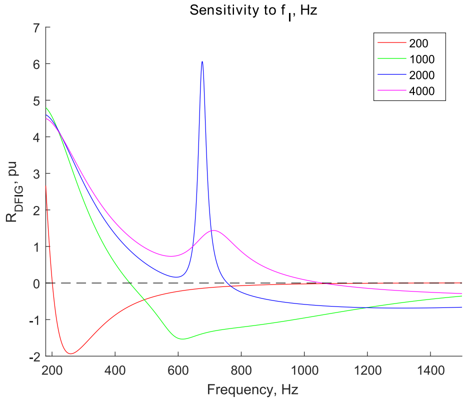

(e) Sensitivity to filter cutoff frequency f_I

Figure 3.4 – Sensitivity analysis of R_{DFIG}, influential variables

The analysis of the influential variables reveals the following information:

- Larger proportional gains K_{pRSC} and K_{pGSC} make the resistance more negative, consequently, more negative damping. The proportional gains contribute to the real part of the impedance with a negative sign, therefore this result is expected (recall the analysis in section 2.4.3 of expression (2.31)). From the tendency, if the proportional gains are reduced near to zero, the negative resistance interval can be eliminated. However, the proportional gains are necessary for proper current control.

- The negative resistance interval is shifted rightwards in the spectrum when the switching frequencies increase due to the effect of the phase shift of the associated delays. By increasing the switching frequencies of the converters, the control delay becomes less relevant. However, large increases lead to small improvements and the switching frequency is limited to the physical properties of the solid state devices. In addition, higher switching frequencies increase the converter losses.
- The increase of the filtering cutoff frequency f_I has a simmilar behavior to the switching frequencies, shifting the negative resistance interval rightwards in the spectrum due to the associated delay. Higher frequency values tend to reduce the effect in the resistance but this represents a trade-off with the noise filtering of the control system.

3.3 Mechanism of unstable high-frequency resonance

Certain combinations of WP size, reactive power compensation level, short-circuit capacity and control parameters, can make the system unstable. High-frequency unstable resonance occurs when a resonance frequency has negative damping. But negative damping at a resonance frequency is not the only required condition for destabilizing a circuit.

To understand the mechanism for high-frequency unstable resonance, consider the circuit in Fig. 3.5(a). The convention for power flow at the PCC can be observed in Fig. 3.5(b).

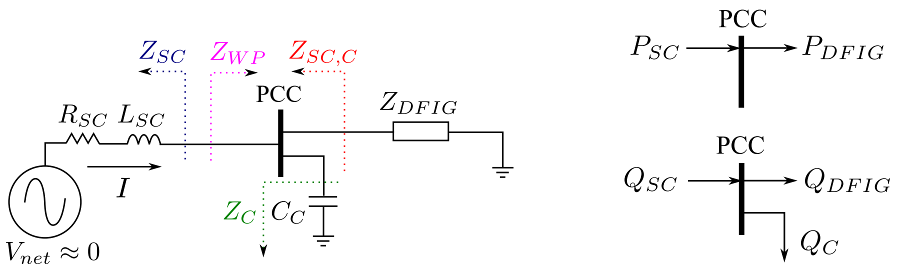

(a) Impedance model (b) Power flow convention

Figure 3.5 – Unstable high-frequency resonance model

The results of Fig. 3.6 correspond to a WP with a capacity of $S_{WP} = 100$ MVA and $Q_C = 10$ MVA of reactive power compensation, at a grid with a short-circuit level of $S_{SC} = 3000$ MVA. To enter unstable resonance conditions, the proportional gain of the GSC was changed from 0.6 to 3 at 6 seconds of simulation. It can be seen that the capacitor associated with the high-frequency resonance injects reactive power, which is consumed by both the DFIG and the grid. The active power at such frequency is provided by the

DFIG due to the action of the control of its voltage source converters (negative resistance), and consumed by the grid. The grid does not contribute to the voltage distortion at the resonance frequency.

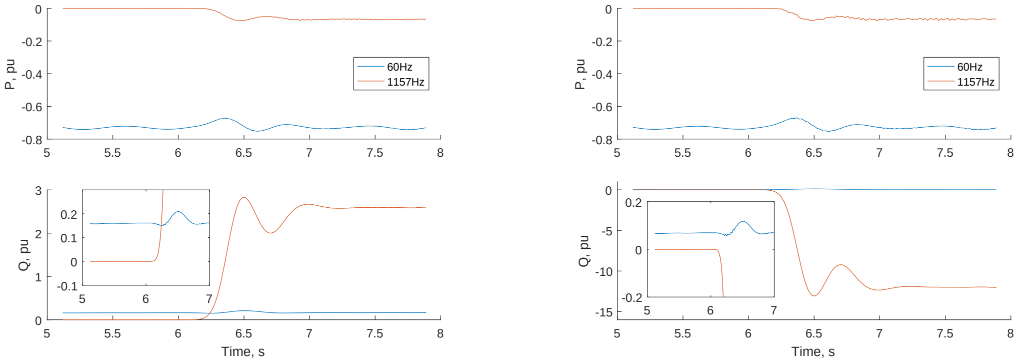

(a) DFIG (b) Grid

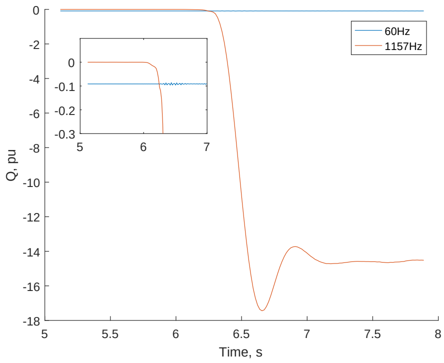

(c) Capacitor

Figure 3.6 – Power flows at PCC, unstable resonance conditions (1157 Hz)

The power flows in Fig. 3.6 confirm the DFIG as the source of energy for the oscillation at resonance frequency. Therefore, the grid impedance and the compensation capacitance can now be regarded as the “load”.

Following the previous logic, the ratio of impedances in expression (3.1) (analog to the calculation of amplification) can be used to determine if the oscillation component injected by the DFIG is attenuated or amplified.

$$A\left(f\right) = \frac{Z_{SC,C}\left(f\right)}{Z_{SC,C}\left(f\right) + Z_{DFIG}\left(f\right)} \tag{3.1}$$

The peak value A_{max} of expression (3.1) occurs at the resonance frequency f_{res}.

$$A_{max} = |A(f_{res})| \tag{3.2}$$

Later on, the damping at PCC can be defined as R_{sum} with expression (3.3). This quantity corresponds to the real part of the denominator of (3.1).

$$R_{sum}(f) = Re\left\{Z_{SC,C}(f) + Z_{DFIG}(f)\right\} \tag{3.3}$$

As stated previously, the phase shift from the filters and control delays at certain parameter configurations is such that it makes the negative resistance of the DFIG larger than the resistance of the grid, which results in negative damping. A resonance from the system with negative damping leads to unstable high-frequency resonance.

3.4 Stability determination methodology

Most of the literature studies the stability of DFIG-based WPs by using Nyquist plots (FAN; MIAO, 2012), eigenvalue analysis and EMT simulation. The Nyquist criterion is an impedance-based mathematical abstraction that uses a ratio of the grid and DFIG impedances Z_{SC}/Z_{WP} as input. This criterion is obtained from the analysis of the current injection I (see Fig. 3.5) from the grid towards the turbine with expression (3.4), considering the grid as the only voltage source.

$$I = \frac{V_{net}}{Z_{WP} + Z_{SC}} = \left(\frac{V_{net}}{Z_{WP}}\right)\frac{1}{1 + Z_{SC}/Z_{WP}} \tag{3.4}$$

The Nyquist criterion assumes a stable voltage source. It also assumes the wind park to be stable when connected directly to this voltage source. Therefore, it is only necessary to study the poles in the right half plane of $1 + Z_{SC}/Z_{WP}$. A Nyquist plot is drawn in the complex plane to determine the number of encirclements of the $(-1, 0)$ point. If the point is encircled, the system is considered unstable.

As an alternative to the Nyquist criterion, a resonance is unstable if it satisfies the following two conditions simultaneously:

$$1) R_{sum}(f_{res}) < 0 \qquad\qquad 2)\ |A(f_{res})| > 1$$

- Condition 1 (Negative damping at resonance): This condition determines the behavior of the oscillation mode associated with the resonance. If this damping is negative, the system is unstable. If the condition is not met, the grid provides sufficient damping to eliminate the oscillation.
- Condition 2 (Amplification at resonance): This condition is stated for the sake of completeness as an attenuated resonance would not result in instability. Attenuated resonances may appear in circuits with capacitors far away from the evaluated PCC.

The two previous conditions are obtained from the impedance model of the circuit using expressions (3.2) and (3.3). Their junction can be used as a criterion to easily visualize the stability at resonance as it directly describes physical characteristics of the circuit (location of the amplification peak in the spectrum and its associated damping) instead of using a mathematical abstraction.

A graphical definition of this criterion for unstable resonance is presented in Fig. 3.7. The shaded area in the plots indicates the frequencies with amplification and negative damping.

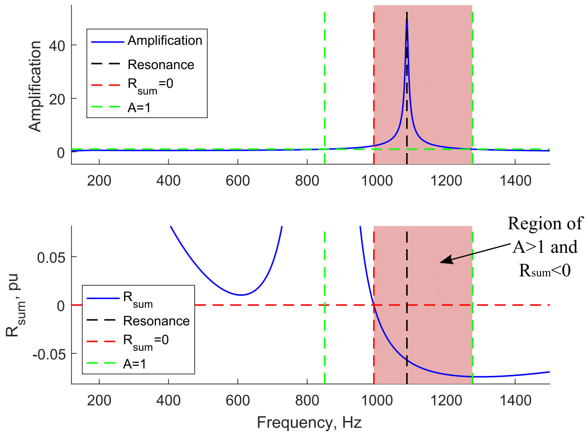

Figure 3.7 – Amplification and damping diagram for resonance stability evaluation

The location of the amplification peak and its damping define the stability of the system. This is illustrated with EMT simulation of the parameter combinations in Table 2. To introduce the resonance, the capacitance at PCC was connected at 1 second of the simulation. The results of the study are presented in Fig. 3.8. The Nyquist stability criterion was also included to compare the results with the proposed stability assessment methodology.

Table 2 – Parameters for unstable resonance evaluation

$S_{WP} = 100$ MVA, $X/R = 10$			
	Unstable	Marginal	Stable
S_{SC}/S_{WP}	10	30	50
Q_C/S_{WP}	0.05	0.1	0.2

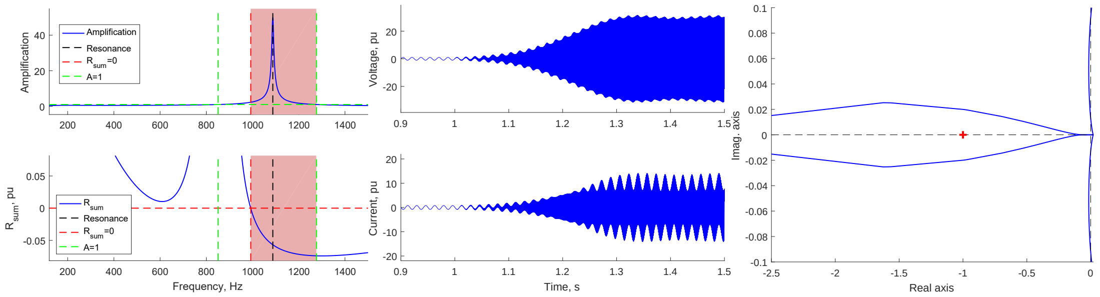

(a) Cond. 1) and 2), unstable (b) EMT waveforms, unstable (c) Nyquist plot, unstable

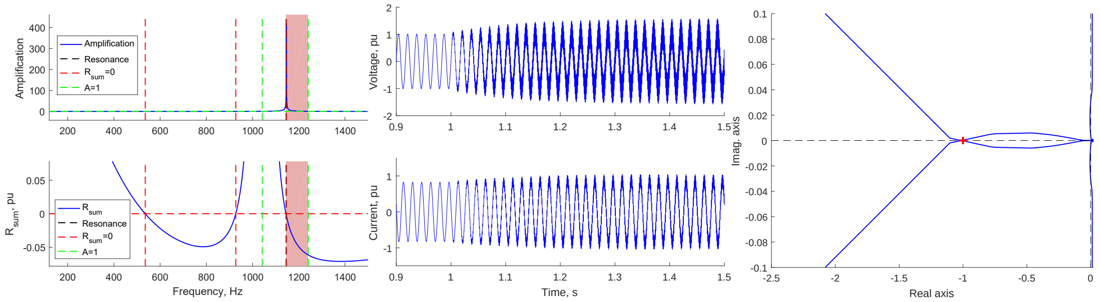

(d) Cond. 1) and 2), marginal (e) EMT waveforms, marginal (f) Nyquist plot, marginal

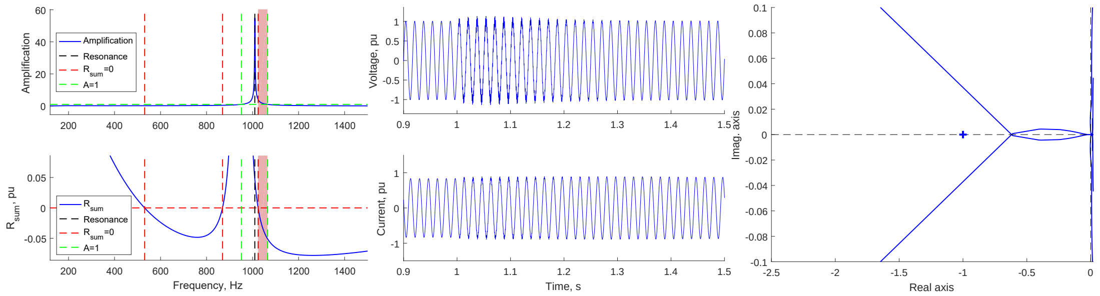

(g) Cond. 1) and 2), stable (h) EMT waveforms, stable (i) Nyquist plot, stable

Figure 3.8 – Unstable resonance conditions and EMT waveforms

In summary, the location of the resonance peak in the spectrum defines the following scenarios:

- Unstable: Inside of the shaded interval. The behavior in time domain is defined by the growth of an oscillating component in the resonant frequency, reaching a considerable magnitude.
- Marginal: At the boundaries of the shaded interval. Sustained oscillations can be observed in the component of resonant frequency with smaller magnitude than the unstable case.
- Stable: Outside of the shaded interval. The oscillation of the resonant frequency is damped over time.

This stability assessment can be presented in terms of values associated with physical quantities such as wind park capacity, the reactive power compensation level and short-circuit level, instead of using a higher mathematical abstraction as done by the Nyquist (-1,0) encirclement criterion. In addition, the proposed criterion can be computed by simply checking the location of a point within an interval. This is less complex than the computation of a directed contour encirclement of a point, which in addition, requires to calculate the number of system singularities.

3.5 Unstable resonance risk region (URRR)

A detailed description of unstable resonances was provided in previous sections. This section uses such description to develop a systematic method for assessing whether a given wind park can experience instability or not. This systematic method consists in determining an unstable resonance risk region as shown in Fig. 3.9. This plot represents multiple wind park capacities, reactive power compensation and short-circuit levels, as it relates the short-circuit ratio S_{SC}/S_{WP} to the reactive power compensation ratio Q_C/S_{WP}. In general, this information is readily available in a wind park.

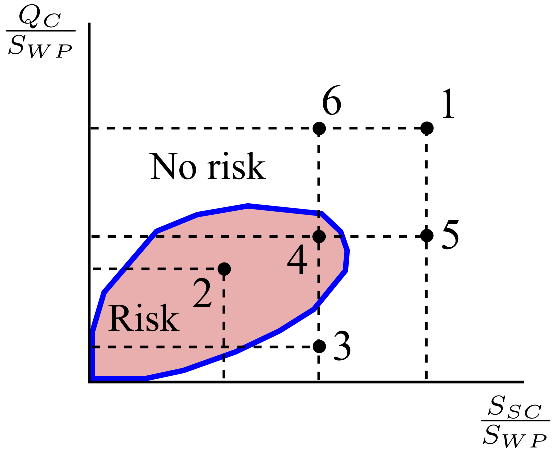

Figure 3.9 – Theoretical unstable resonance risk region

The shaded region corresponds to all parameter combinations resulting in high-frequency unstable resonance. The black markers correspond to scenarios that yield the following information:

- Points 1, 3, 5 and 6 are free of unstable resonance.
- Moving from point 1 towards point 2 in Fig. 3.9 represents an increase in S_{WP} by the connection of a group of wind turbines (so that $S_{WP_2} > S_{WP_1}$) while the reactive power compensation and the grid remain unchanged. This transition will create unstable resonance conditions.
- Moving from point 5 towards point 4 in Fig. 3.9 represents a reduction in short circuit capacity at PCC (so that $S_{SC_5} > S_{SC_4}$) due to a line outage which increased the equivalent impedance of the grid equivalent at PCC. This leads to unstable resonance conditions.
- Moving from point 5 towards point 4 in Fig. 3.9 can also be seen as the connection of a block of turbines in the WP with a proportional increase in reactive power compensation (so that $S_{WP_4} > S_{WP_5}$) while the grid conditions remain unchanged. The system will enter unstable resonance conditions with this operation.

- Moving from point 4 towards point 3 in Fig. 3.9, is a reduction in the reactive power compensation level of the WP to exit unstable resonance conditions (so that $Q_{C_3} < Q_{C_4}$).
- On the other hand, moving from point 3 towards point 4 in Fig. 3.9 indicates the connection of a capacitor bank stage which leads to unstable resonance. In order to exit these conditions, an additional block can be connected to move towards point 6 (so that $Q_{C_3} < Q_{C_4} < Q_{C_6}$).

The URRR can be obtained by performing repeated EMT simulations of all parameter combinations of reactive power compensation Q_C, wind park capacity S_{WP} and grid short-circuit capacity S_{SC}. The triples leading to unstable resonance can be later used to calculate the ratios S_{SC}/S_{WP} and Q_C/S_{WP}.

The following algorithm is used to detect parameter combinations with unstable resonance for every possible triple (Q_C, S_{WP}, S_{SC}):

- The circuit is simulated for a total of 4 s, and the capacitor bank is connected at 1 s.
- The voltage waveforms are collected with a sampling rate of 256 samples/cycle. This sampling frequency is able to visualize components up to 7680 Hz, which is sufficient for the studied range.
- The voltages are balanced, therefore, only phase A data is collected.
- The FFT is applied to the voltage waveforms in windows of 12 fundamental cycles (this resulted in a resolution of 5 Hz in the frequency spectrum). The window is shifted every one fundamental cycle.
- All of the components from the FFT with magnitude over 5 % of the fundamental frequency are preserved and the rest are forced to zero to eliminate noise.
- If any frequency component other than the fundamental frequency is detected, the following check conditions are evaluated:
    - Minimum time condition: Any remaining voltage components present in the simulation for at least 25 % of the time.
    - Non-damped condition: Any remaining voltage components different from zero in the last 20 % of the simulation time.
    - If both conditions are true, the presence of unstable resonance is confirmed.
- If unstable resonance is reported, the frequency component with the largest magnitude is chosen as the unstable resonance frequency.

An example of the detection capability of the algorithm is presented in the results of Fig. 3.10, which corresponds to the triple (Q_C, S_{WP}, S_{SC})=(10, 100, 2500) MVA. The algorithm determined the presence of an important high frequency component at 1067 Hz after the capacitor connection. The high-frequency component grew over time, triggering the minimum voltage magnitude check. At the end of the simulation, both the minimum time and the non-damped checks were met, therefore, the combination of parameters resulting in the ratio (S_{SC}/S_{WP}, Q_C/S_{WP})=(25, 0.1) was flagged as an unstable resonance.

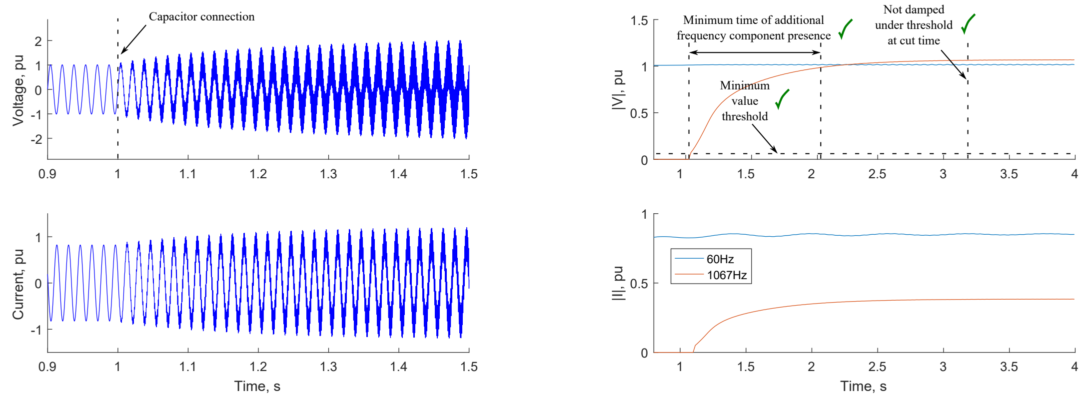

(a) Waveforms (b) Magnitude per frequency components

Figure 3.10 – Unstable resonance detection via simulation, voltage and current

The algorithm rejects all combinations of stable resonance. Fig. 3.11 presents the results for the triple (Q_C, S_{WP}, S_{SC})=(20, 100, 6000) MVA. As only the minimum voltage check was triggered, the combination was discarded. Nevertheless, other parameter combinations with the same ratios (S_{SC}/S_{WP}, Q_C/S_{WP})=(60, 0.2) still need to be evaluated in order to confirm that such point in the URRR will not involve unstable resonance.

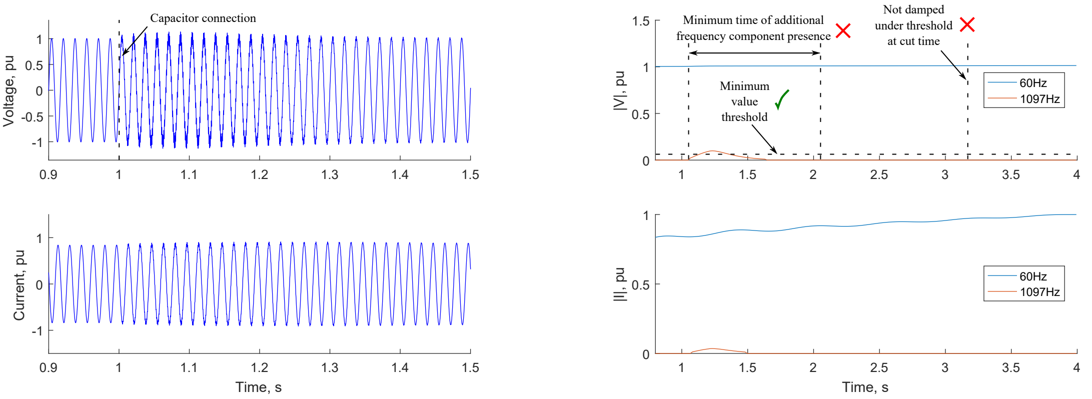

(a) Waveforms (b) Magnitude per frequency components

Figure 3.11 – Stable resonance detection via simulation, voltage and current

The simulation process proved to be a time-consuming task due to the large number scenarios and the high modeling detail of the EMT simulation. In addition, poorly damped scenarios can be mistaken for unstable scenarios if the condition of damping under threshold cutoff time is not set properly, i.e., the resonance signal damps out in the interval between the cutoff time and the end of the simulation, giving a false positive instability flag.

3.5.1 Model-based algorithm to build the URRR

This section presents a simple analytical method for obtaining the URRR. It is based on the impedance model of the DFIG and uses the amplification and damping at resonance criterion. The procedure is detailed as follows:

- Fix the WP capacity S_{WP} to one value, e.g., $S_{WP} = 100$ MVA. This step is only necessary to calculate the pu impedances of the wind park equivalent and the grid equivalent (recall the expressions in section 2.2), as the results of the plot are independent of the selected WP capacity.
- Define a frequency interval for the analytic sweep with an upper limit larger than the maximum evaluated frequency, e.g., $f \in [180, 6000]$ Hz.
- Fix the study frequency interval for the model at the frequency range of study, e.g., $f_{study} = [180, 1500]$ Hz.
- Define a range of S_{SC}/S_{WP} to be evaluated, e.g., $S_{SC}/S_{WP} = [2, 3, ..., 30, 40, ..., 100]$, and obtain the respective S_{SC} values. It is advised to consider ratios greater then 2. When evaluating low ratios, small steps are advised (i.e., from 2 up to 30 in steps of 1) for better resolution of the region as instability tends to appear at low ratios.
- Define a range of Q_C/S_{WP} to be evaluated, e.g., $Q_C/S_{WP} = [0.01, 0.02, ..., 0.2, 0.3, ..., 1]$ and obtain the respective Q_C values. Again, at the low ratios, define small increments (i.e., from 0.01 up to 0.2 in steps of 0.01) for a better resolution of the region as instability tends to appear at low ratios.
- Fix the rest of the parameters.
- For each (Q_C, S_{SC}) pair, sweep f to:
  - Obtain the amplification from expression (3.1).
  - Obtain the maximum amplification and store the resonance frequency f_{res}.
  - If $f_{res} \in f_{study}$:
    - Obtain the amplification at resonance $|A(f_{res})|$.
    - Calculate the damping at resonance $R_{sum}(f_{res})$.
    - Evaluate if $|A(f_{res})| > 1$ and $R_{sum}(f_{res}) < 0$. If yes, store the. from the amplification and damping at resonance criterion. If met, store the (Q_C, S_{SC}, f_{res}) triple. Else, discard it.
- From all of the stored (Q_C, S_{SC}, f_{res}) triples and the fixed S_{WP}, calculate the respective $(Q_C/S_{WP}, S_{SC}/S_{WP})$ pairs.
- The URRR is defined by the resulting $(Q_C/S_{WP}, S_{SC}/S_{WP})$ pairs.

The URRR of Fig. 3.12 was built with the equivalent impedance model and using the previous procedure. Recall the simulation cases of Fig. 3.8. It was confirmed that the unstable cases are located within the URRR, the marginal ones are near to the border of the region, and the stable ones are located outside of it.

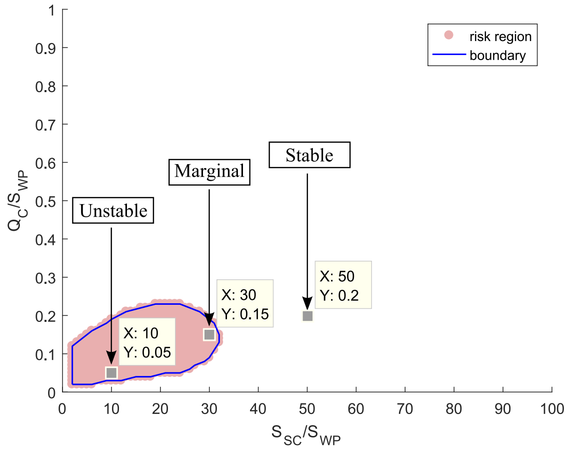

Figure 3.12 – Analytic unstable resonance risk region

The process of building the URRR is greatly facilitated by using the model-based approach instead of repeated EMT simulation. The computational requirements are much lower, as well as the modeling detail. Therefore, it can be used as a viable alternative to the assessment of the stability of high-frequency resonance of multiple scenarios.

3.5.2 Validation of the URRR

The validation of the URRR for a wind park of $S_{WP} = 100$ MVA is presented in Fig. 3.13. The red dotted line corresponds to the analytic determination of the URRR. The risk region obtained by repetitive EMT simulations is given by the blue solid line. These model-based approaches are conservative when compared to the EMT simulation (shaded area within the blue solid line).

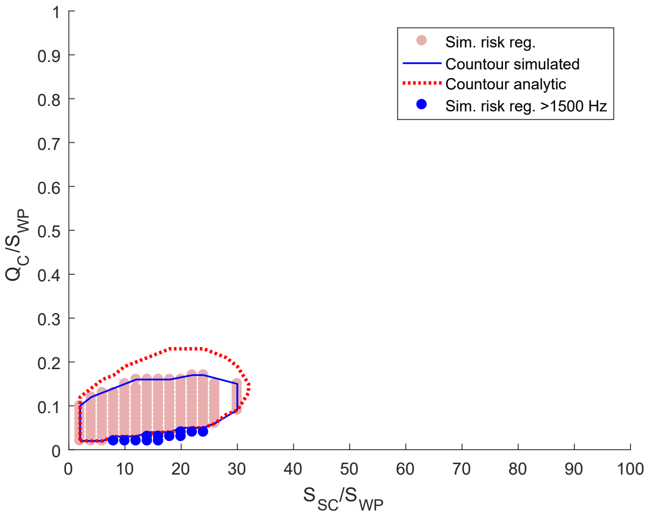

Figure 3.13 – URRR validation with EMT simulation

The combinations with blue markers of Fig. 3.13 correspond to the unstable resonances above 1500 Hz. As these conditions occur only in very specific scenarios, one can consider them to be within a margin of error of the boundary. As an alternative, the analytic URRR can be increased slightly to encompass these instabilities above 1500 Hz, i.e., expanding the interval of studied frequencies f_{study}.

The results indicate that the DFIG impedance model is accurate to assess the stability of the DFIG at high-frequency resonance without the need of running repeated EMT simulation. The EMT validation of Fig. 3.13 took several hours, whereas the analytic region can be drawn in a few seconds.

3.5.3 URRR sensitivity

This section studies how the circuit parameters which are not directly represented in the URRR affect the unstable resonance combinations.

The results for the variables with the highest influence in the shape of the URRR are presented in the sensitivity analysis of Fig. 3.14. These variables were selected for their higher influence in the previous sensitivity studies of the resistance and amplification at resonance.

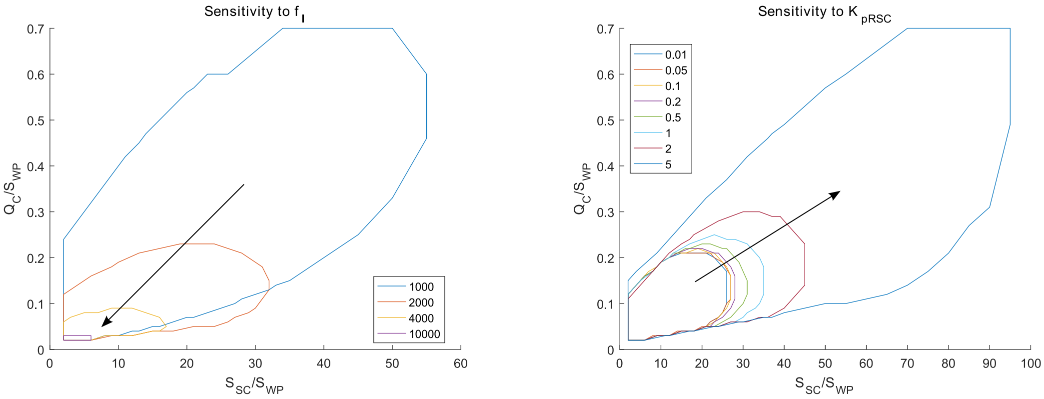

(a) Sensitivity to filter cutoff frequency (b) Sensitivity to RSC's proportional gain

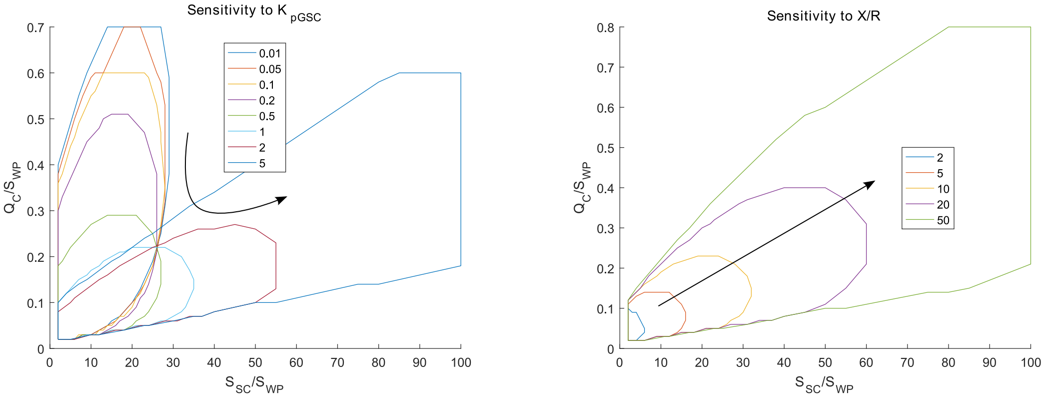

(c) Sensitivity to GSC's proportional gain (d) Sensitivity to grid's X/R ratio

Figure 3.14 – Sensitivity analysis of URRR, influential variables

Fig. 3.14 (a) presents the effect of the current measurement filter's cutoff frequency. The risk region becomes smaller with larger frequency values (no region for values over 10 kHz), but this would imply no filtering of the input signals. On the other hand, the lower this frequency, the larger the risk region. This occurs as the filter delay becomes more important, making the negative damping larger by increasing the phase shift of the DFIG impedance. The modelling of this parameter is fundamental to study the unstable resonance.

The effect of the proportional gains of the converters is presented in Fig. 3.14 (b) and (c). It can be observed that the larger the K_{pRSC} value, the larger the risk region. It can also be noted that a certain a value of K_{PGSC} minimizes the risk region. As observed in the sensitivity analysis of the negative resistance, larger proportional gains are associated with larger negative resistance, and thus, higher chances of the resonance to occur in the frequency interval of negative damping. These control gains can be used with a higher degree of freedom than the other variables to avoid unstable resonance conditions, making them an attractive candidate to partially mitigate the advance of an unstable resonance.

Finally, the effect of the grid's X/R ratio is presented in Fig. 3.14 (d). Lower ratios mean higher resistance, which increases the grid damping. These results indicate that there is a higher risk of unstable resonance to occur in WPs connected to transmission networks than those connected to distribution networks.

3.5.4 Mitigation of high-frequency unstable resonance based on the URRR

It is possible to implement preventive mitigation actions based on the URRR by observing how the operating point (i.e. compensation capacity and short-circuit ratio) is located according to the URRR, and how the region changes with new circuit parameter values. Suppose the unstable resonance risk regions in Fig. 3.15 for three different inner current control loop configurations:

- With both RSC and GSC feed-forward and GSC proportional gain of $K_{pGSC} = 0.86$.
- Without feed-forward and GSC proportional gain of $K_{pGSC} = 0.86$.
- Without feed-forward and reduced GSC proportional gain of $K_{pGSC} = 0.1$.

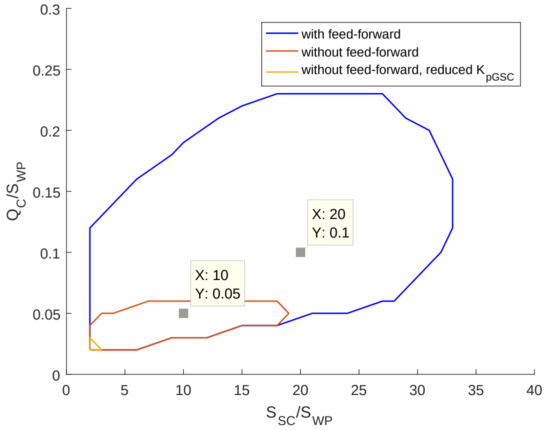

Figure 3.15 – URRR for different control configurations

The markers in Fig. 3.15 present two combinations that result in high-frequency unstable resonance for the first scenario. If operating with feed-forward (blue curve) at the point $(S_{SC}/S_{WP}, Q_C/S_{WP}) = (20, 0.1)$, the unstable resonance can be mitigated by removing the feed-forward from the inner current control loop, i.e., by operating at the orange curve. This operation was at 1.5 seconds of simulation and the results can be observed in Fig. 3.16.

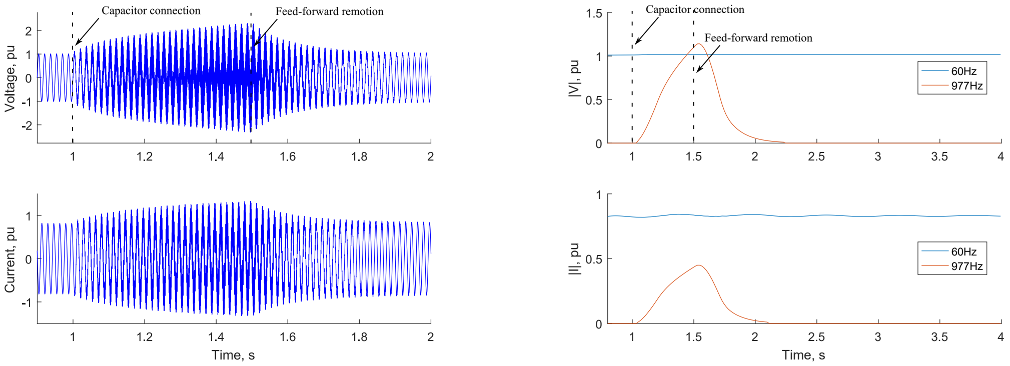

(a) Waveforms (b) Magnitude of components

Figure 3.16 – Mitigation of unstable resonance by feed-forward remotion

Now consider the more critical case of operating with feed-forward (blue curve) at the point $(S_{SC}/S_{WP}, Q_C/S_{WP}) = (10, 0.05)$. Here, removing the feed-forward terms will not suffice to mitigate the unstable resonance (orange curve). Thus, further actions are required such as reducing the proportional gain of the GSC current controller. By doing so, the risk region is considerably reduced (yellow curve). To demonstrate the previous statement, the mitigation actions were taken at 2 s and 3 s respectively, as in Fig. 3.17.

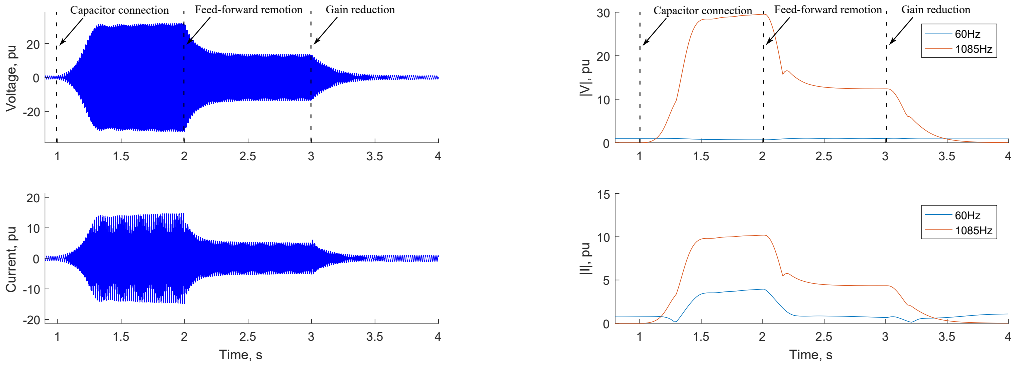

(a) Waveforms (b) Magnitude of components

Figure 3.17 – Mitigation of unstable resonance by feed-forward remotion and gain reduction

From the previous scenarios, it can be observed that both the feed-forward structure and the control tuning have important influence in the shape of the URRR as they also modify the DFIG impedance. A proper control tuning and feed-forward structure can eliminate the risk of high-frequency unstable resonance.

These mitigation techniques can be directly implemented in the controller of the DFIG converters by considering the shape of the URRR. Thus, the high-frequency unstable resonance can be studied as a local phenomenon using the URRR at PCC.

The elimination of the feed-forward can be used as a mitigation action to prevent the progress of unstable resonance, however, it slows down the response of the DFIG to output tracking. To mitigate unstable resonance while preserving the DFIGs tracking performance, the authors in (SONG *et al.*, 2017) proposed an active damping strategy by including a term in the feed-forward to add a virtual resistance to the impedance of the converters. A detailed study of mitigation techniques will be conducted as future work.

3.6 Important remarks

The impedance model of the converters cannot be neglected in order to study the stability of the system at resonance. It was confirmed that the impedance model of the DFIG and the equivalent grid impedance at PCC is sufficient to study the stability at high-frequency resonance of the interaction of the grid and the converter control, in the range of frequencies of 180 Hz to 1500 Hz.

To perform an adequate assessment, it is important to consider the following points that affect the converter's impedance:

- The bandwidth of the PLL and outer loop controllers.
- The inner current control loop gains.
- Filters and delays.
- The feed-forward structure of the inner current control loop.

Based on the results, high-frequency unstable resonance proved to occur at the following conditions of resonance and negative damping:

- Reactive power compensation ratios of $Q_C/S_{WP} < 0.2$.
- Short circuit ratios of $S_{SC}/S_{WP} < 30$.

Nevertheless, the following points also need to be considered:

- The short circuit ratio S_{SC}/S_{WP} tends to increase along with the X/R ratio. This means that lower short circuit ratios lead to higher damping values, and thus, the unstable resonance risk tends to be lower.
- Any circuit element with positive resistance will contribute to the system damping. For example, some DFIGs feature small shunt capacitors to filter the switching frequency distortions caused by the GSC. These capacitors may have a series resistance which contributes to the overall system damping. Loads also provide positive damping.

Given the previous considerations, it is unlikely to achieve the conditions for unstable high-frequency resonance in strong systems (high S_{WP}/S_{SC} ratios). Even in weak systems, the unstable resonances can be avoided by the positive damping characteristic of loads, low X/R ratios of the grid equivalent, and by proper tuning of the DFIG controllers based on the URRR.

Nevertheless, even if there is no unstable resonance (i.e., with negative damping), there can still exist weakly damped resonances (i.e., with low damping) in the wind park interconnection. Such weakly damped resonances also deteriorate the power quality of the system by amplifying background harmonic distortions and potentially damaging some equipment. A graphic approach to assess harmonic resonance phenomenon is further addressed in chapter 4.

3.7 Summary

This chapter has investigated the causes of high-frequency stability problems in DFIG-based wind parks, and determined they appear due to the negative damping effect of the DFIG converters in combination with resonance in the studied frequency range of 180 Hz to 1500 Hz. The main cause of this negative resistance effect are the phase angle shift introduced by measurement filters and the time delays, and large proportional gains of the control circuit.

Numerous EMT simulations are generally conducted to determine under which operating conditions a wind park can face high-frequency resonance stability problems. To facilitate this assessment, the chart in Fig. 3.18 was proposed, namely the Unstable Resonance Risk Region (URRR).

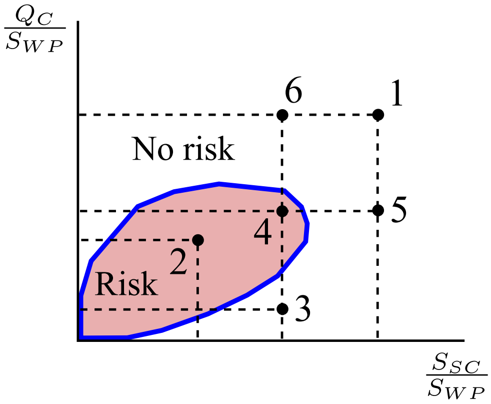

Figure 3.18 – Theoretical unstable resonance risk region

Through this chart, an engineer can quickly determine if there is risk of high-frequency unstable resonance in a wind park, knowing only the system short-circuit level, the wind park capacity and the reactive power compensation level. Furthermore, the risk region can be obtained analytically, without the need for any computer simulations.

The analysis of the risk region determined the following points:

- Unstable resonances take place if the negative resistance of the DFIG has a greater magnitude than the equivalent resistance of the utility grid in the resonance frequency (i.e., if there is negative damping at resonance).
- The minimum reactive power compensation level in the wind park Q_C/S_{WP} and short-circuit ratio S_{SC}/S_{WP} that guarantee no risk of high-frequency instability can be determined. For the wind park that was tested in this chapter, these minimum values correspond to $Q_C/S_{WP} \approx 0.2$ and $S_{SC}/S_{WP} \approx 30$ in a grid with low damping.

- Proper tuning of DFIG control parameters can reduce the risk of high-frequency instability problems even for wind parks with low reactive power compensation or connected to weak grids. Resistive loads will most likely eliminate the risk of high-frequency unstable resonance as they contribute with positive damping (LEAO *et al.*, 2014). However, resonances with high amplification can still occur and create excessive harmonic distortions. This will be discussed in the following chapter.

4 Harmonic resonance analysis

The previous chapter revealed high-frequency stability of DFIG-based wind parks is unlikely to become a general concern in practice due to two main reasons: instability problems can be avoided by properly tuning DFIG control parameters; and elements of the grid will most likely contribute with sufficient positive damping. Nevertheless, weakly damped resonances may still occur between the capacitive compensation of the wind park and the inductive characteristic of the grid and DFIG. These resonances can be excited if they occur close to harmonics that are present in the grid (e.g., the 5^{th}, 7^{th}, 11^{th} or 13^{th} harmonics).

This chapter investigates when these resonances become a concern to the utility. Traditionally, such analysis is carried out by running numerous EMT simulations, but this chapter proposes two charts to simplify the assessment. The charts can be obtained analytically, by using the circuit model of the wind park and without running any EMT simulation. Through a quick inspection of these charts, an engineer can conclude if there is risk of harmonic resonance in a wind park, and which changes in the wind park (such as expansions) or in the grid (such as an increase in the short-circuit level) can create harmonic resonance risk. Only the short-circuit level of the grid at the point of common coupling with the wind park, the rated capacity of the wind park and its reactive power compensation level need to be known to assess the proposed charts.

Finally, a measurement-based approach is also proposed to obtain the charts if the wind park circuit model is not available.

4.1 Harmonic resonance in wind parks

The authors in (SONG *et al.*, 2017) report the existence of harmonic resonance (weakly damped resonance) in DFIG-based wind parks. This was confirmed using the impedance model in chapter 2 and a detailed EMT simulation study which is presented as follows:

The parameters of the grid were set to a short-circuit ratio $S_{SC} = 3500$ MVA and $X/R = 10$, and the wind park capacity was set to $S_{WP} = 100$ MVA with a reactive power compensation of $Q_C = 25$ MVA. At 2.5 seconds, two components of 660 Hz and 780 Hz with 1 % magnitude of the fundamental each (11^{th} and 13^{th} harmonics) were added as background voltage distortions in the grid equivalent. The results of the simulation study are presented in Fig. 4.1, where a resonance took place near the 13^{th} harmonic given that the small harmonic distortion component was greatly magnified, but the 11^{th} harmonic was not affected.

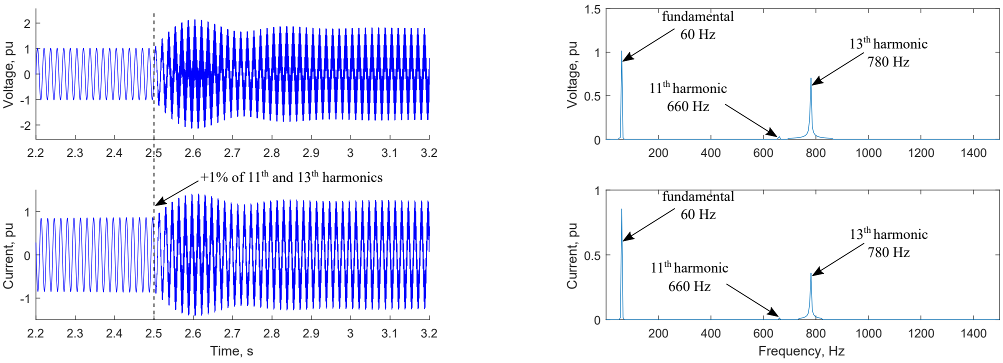

(a) Voltage and current waveforms

(b) FFT spectrum of the last 12 fundamental cycles

Figure 4.1 – Resonance (780 Hz) at PCC of DFIG-based wind park in presence of voltage background distortion at 11^{th} and 13^{th} harmonics

Now suppose the grid was reconfigured due to maintenance of a line, and therefore, the short-circuit level at PCC was reduced to $S_{SC} = 2300$ MVA and the same background distortion of the previous case was added. Fig. 4.2 confirms the new grid condition has a resonance at the 11^{th} harmonic. This scenario demonstrates that changes in the grid can induce harmonic resonance conditions or shift their location in the spectrum.

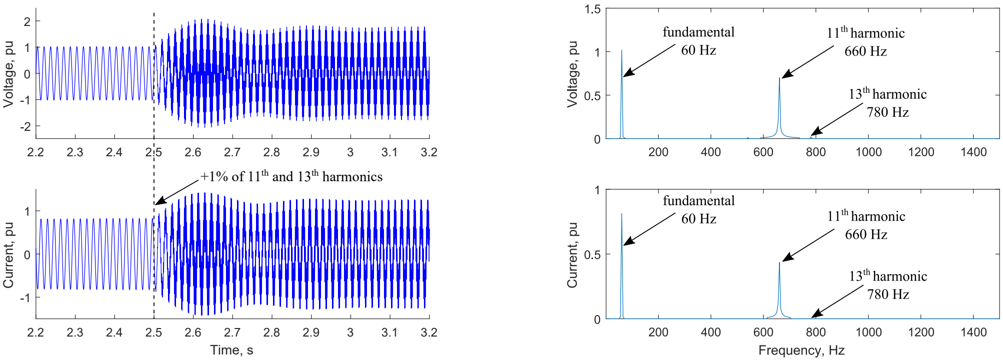

(a) Voltage and current waveforms

(b) FFT spectrum of the last 12 fundamental cycles

Figure 4.2 – Resonance (660 Hz) at PCC of DFIG-based wind park in presence of voltage background distortion at 11^{th} and 13^{th} harmonics

Finally, suppose one stage of the compensation capacitance is disconnected. The reactive power compensation level will decrease to $Q_C = 10$ MVA. If the same background distortion is present, it does not result in harmonic resonance as the resonance frequency is shifted to a higher value (19^{th} harmonic in this case). Simulation results of this scenario are presented in Fig. 4.3. Note that wind park operations such as removing a stage of capacitive compensation or adding a block of turbines can create or eliminate a harmonic resonance condition.

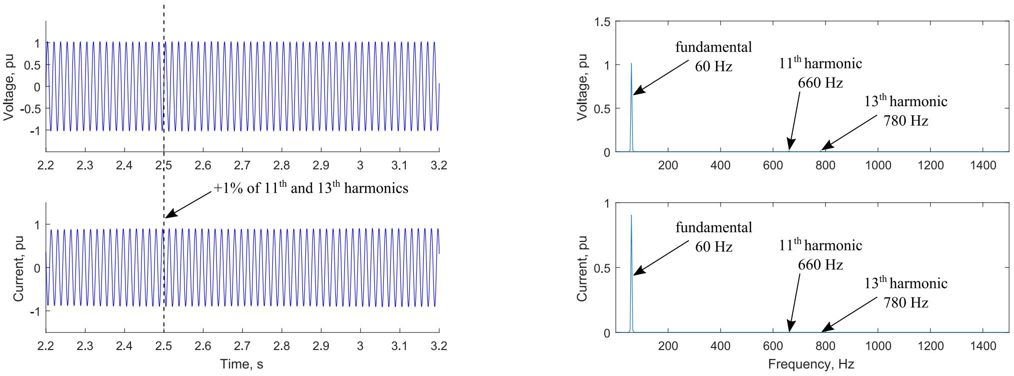

(a) Voltage and current waveforms

(b) FFT spectrum of the last 12 fundamental cycles

Figure 4.3 – No resonance at PCC of DFIG-based wind park in presence of voltage background distortion at 11^{th} and 13^{th} harmonics

As observed from the previous examples, several situations may lead to harmonic resonance. A detailed assessment of harmonic resonance involves the study of a large number of scenarios with multiple parameter combinations (such as wind park capacity, short-circuit level, or reactive power compensation levels). This requires numerous EMT simulations, which demand significant time and computational resources, making the approach inviable.

In order to address this issue, the following sections present two practical charts designed to facilitate the analysis of harmonic resonance in DFIG-based wind parks without the necessity of any simulation.

4.2 Reactive compensation at resonance risk chart

It is important to evaluate different reactive power compensation levels as they have a significant influence in the resonance frequency. To this end, the present section proposes a chart shown in Fig. 4.4, namely the reactive compensation at resonance risk (RCRR) chart.

The risk region is delimited by resonance frequencies below or equal to a harmonic order h_{max}. Combinations of S_{SC}/S_{WP} and Q_C/S_{WP} that yield a resonance frequency at harmonic order below or equal to h_{max} are in the risk region. This harmonic limit is set to $h_{max} = 13$ in this dissertation, but it can be adjusted according to the utility and the wind park requirements.

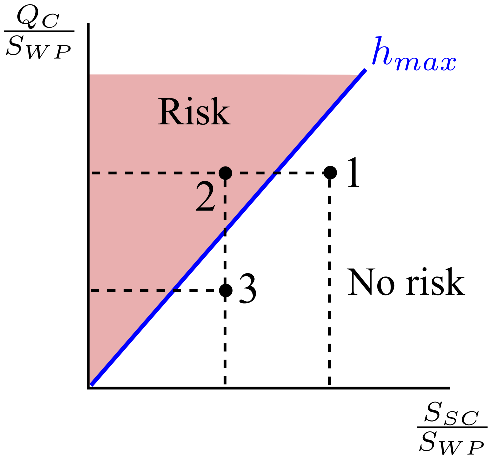

Figure 4.4 – Theoretical reactive compensation risk at resonance region

By using the RCRR chart, engineers are able to quickly assess if wind park reconfigurations or if changes in the grid will induce resonance frequencies within the range of typical voltage background distortion of the grid, where the blue boundary corresponds to h_{max}. For example, from Fig. 4.4 it can be observed that:

- Given the harmonic limit h_{max}, the points at the white region (e.g., points 1 and 3) are wind park and grid combinations free of harmonic resonance risk. On the other hand, the combinations located within the shaded region (e.g., point 2), present risk of harmonic resonance.
- A wind park with characteristics of point 1 will experience problematic harmonic resonances if its capacity is expanded, while the percentage of reactive power compensation and the grid short-circuit level remain unchanged (i.e. move from point 1 to point 2 of Fig. 4.4).
- A wind park will also experience problematic harmonic resonances if its characteristic is in point 3 and the reactive compensation level is increased from (i.e. move from point 3 to point 2 of Fig. 4.4), while the grid and the wind park capacity remain unchanged.

To illustrate this risk region in an actual wind park, consider the circuit in Fig. 4.5. The simulation parameters for the wind park and the grid are given in Table 5 of the Appendix. The equivalent resistance and inductance of the grid are given as functions of the short-circuit level S_{SC} and the X/R ratio as shown in expression (4.1), and the compensation capacitance in terms of the reactive power compensation ratio as in expression (4.2).

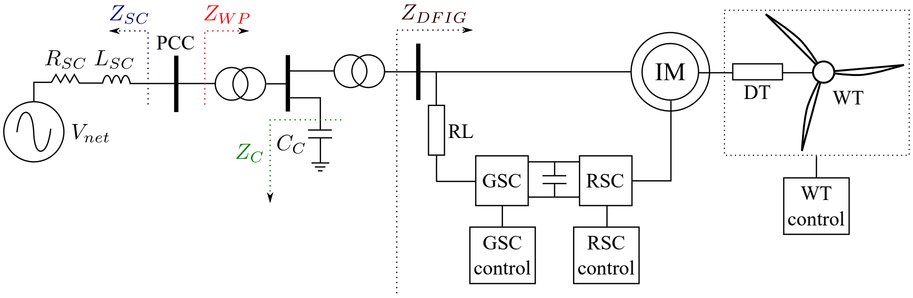

Figure 4.5 – DFIG-based wind park model at PCC

$$L_{SC} = \frac{{V_{\substack{base\\PCC}}}^2}{S_{SC}\omega_0} \frac{1}{\sqrt{1+(X/R)^{-2}}} \qquad R_{SC} = \frac{\omega_0 L_{SC}}{(X/R)} \tag{4.1}$$

$$C_C = \frac{(Q_C/S_{WP})\, S_{WP}}{\omega_0 {V_{\substack{base\\PCC}}}^2} \tag{4.2}$$

In order to obtain the RCRR, such circuit was modeled for detailed EMT simulations at each of the S_{SC}/S_{WP} vs. Q_C/S_{WP} ratio combinations from Fig. 4.6.

For each parameter combination, 5^{th}, 6^{th}, ..., 13^{th}, 14^{th} harmonic order distortions were added to the grid equivalent and the order with the highest amplification at PCC voltage was stored. If the corresponding harmonic is located in the range up to 13^{th} order, the parameter combination is flagged as it produced a problematic resonance within the studied range, meaning that the combination is in the risk region. The resulting risk region is formed by the pink dots in Fig. 4.6.

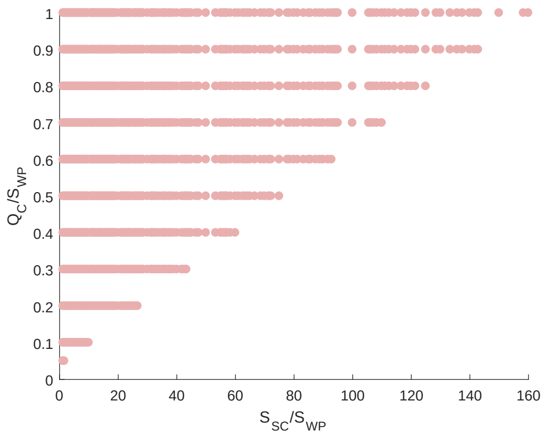

Figure 4.6 – Parameter combinations with resonance frequencies lower than $h_{max} = 13$

This task is highly time-consuming, as it requires to repeat the entire study for different reactive compensation levels. The following section presents an analytic procedure to build the chart from the impedance model of the DFIG from Chapter 2 without the need to run any EMT simulations.

4.2.1 Model-based approach to build the RCRR

Suppose the circuit at Fig. 4.7 (b) which describes the DFIG-based wind park and the grid equivalent at PCC as a set of impedances for conditions where only the grid injects harmonic components. The voltage amplification of these harmonics can be described by expression (4.3).

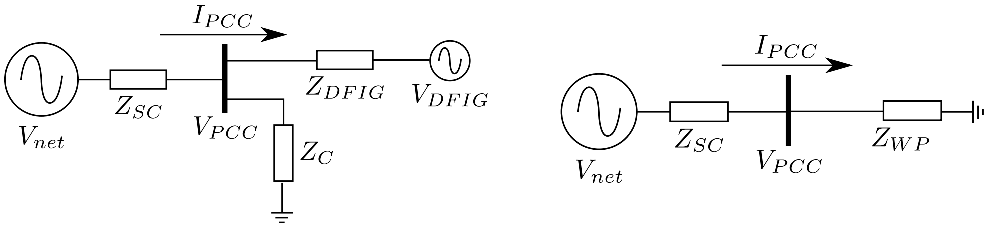

(a) Model for any frequency

(b) Simplified model for grid-injected harmonics

Figure 4.7 – Impedance models at PCC for harmonic resonance study of DFIG-based wind parks

$$A = \frac{V_{PCC}}{V_{net}} = \frac{Z_{WP}}{Z_{SC} + Z_{WP}} \tag{4.3}$$

The grid equivalent is modeled as a series RL branch of impedance Z_{SC} using expression (4.4) in terms of the short-circuit ratio S_{SC}/S_{WP} and the wind park capacity S_{WP} as in expression (4.1). The wind park impedance Z_{WP} can be calculated with expression (4.5) as a parallel of the compensation capacitance Z_C (see expression (4.6), which depends on the reactive power compensation ratio Q_C/S_{WP} and the WP capacity S_{WP} as in expression (4.2)) and the DFIG impedance Z_{DFIG} (see the expressions in chapter 2).

$$Z_{SC} = R_{SC} + sL_{SC} \tag{4.4}$$

$$Z_{WP} = \left(Z_{DFIG}{}^{-1} + Z_C{}^{-1}\right)^{-1} \tag{4.5}$$

$$Z_C = \frac{1}{sC_C} \tag{4.6}$$

The reactive compensation at resonance risk chart can be built by evaluating a range of wind park capacities S_{WP}, a range short-circuit capacities S_{SC}, and a range of reactive power compensation ratios Q_C/S_{WP}. This chart incorporates several reactive power compensation ratios instead of using a fixed value (as done previously for the resonance risk region chart) in order to study the changes in the resonance frequency. These three parameters are used to calculate the impedance expressions of the circuit at Fig. 4.7.

For each triple (S_{WP}, S_{SC}, Q_C), the amplification expression (4.3) is evaluated at a range of harmonic frequencies h up to a maximum considered harmonic, e.g., $h_{max} = 13$. This range is set to $h = [3, 4, 5, \ldots, h_{max}, h_{max} + 1]$ as it is necessary to observe if a peak value of amplification occurred at a harmonic order equal or lower than h_{max} (i.e., a resonance will occur at a harmonic $k \in h$, if $|A(k-1)| < |A(k)|$ and $|A(k)| > |A(k+1)|$ are true). If a resonance within the studied interval is detected, the pair of ratios $(S_{SC}/S_{WP}, Q_C/S_{WP})$ calculated from the triple (S_{WP}, S_{SC}, Q_C) is flagged as a problematic parameter combination and located in the risk region of harmonic resonance.

The model-based approach to build the RCRR is given as follows:

- Set the maximum evaluated harmonic order, e.g., $h_{max} = 13$.
- Set the evaluated frequency range, e.g., $h = [3, 4, 5, \ldots, h_{max}, h_{max} + 1]$.
- Set a range of wind park capacities, e.g., $S_{WP} = [2, 5, 10, \ldots, 100]$ MVA.
- Set a range of short-circuit levels, e.g., $S_{SC} = [5, 10, 20, \ldots, 1000]$ MVA.
- Set a range of reactive power compensation ratios, e.g., $Q_C/S_{WP} = [0.01, 0.05, \ldots., 0.5]$.
- For each triple (S_{WP}, S_{SC}, Q_C) with $S_{WP} < S_{SC}$:
  - Calculate the impedances Z_{SC}, Z_C, Z_{DFIG} and Z_{WP}.
  - Calculate the amplification A at every evaluated harmonic from h.
  - If a peak value of amplification is detected at a frequency equal or lower than h_{max}, mark the respective pair of ratios $(S_{SC}/S_{WP}, Q_C/S_{WP})$ as a problematic combination for harmonic resonance.
- Plot all the problematic combinations for harmonic resonance to build the RCRR, using the S_{SC}/S_{WP} in the horizontal axis and Q_C/S_{WP} in the vertical axis.

This procedure tests each parameter combination in a point-to-point fashion using the impedance model of the wind park, including the internal wind park circuit in detail.

A simplified approach to obtain the RCRR is to define its boundary directly instead of using a point-to-point test. This boundary was added to Fig. 4.8 as a blue line.

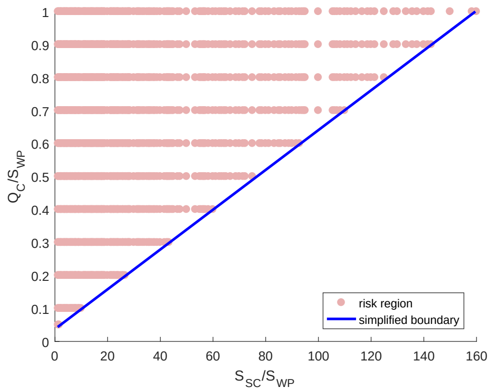

Figure 4.8 – Analytic RCRR and simplified boundary

As this chart focuses in the value of the resonance frequency , the simplified approach is possible by re-arranging the resonance frequency expression (2.37) to evidence the reactive power compensation ratio Q_C/S_{WP} in terms of the short-circuit ratio S_{SC}/S_{WP}, for any given resonance frequency value f_{res}. This procedure results in expression (4.7).

$$f_{res} \approx f_0 \sqrt{(Q_C/S_{WP})^{-1} \left(\sqrt{1+(X/R)^{-2}}\,(S_{SC}/S_{WP}) + {L_{DFIG_{pu}}}^{-1} \right)}$$

$$Q_C/S_{WP} \approx \left(\frac{f_0}{f_{res}} \right)^2 \left(\sqrt{1+(X/R)^{-2}}\,(S_{SC}/S_{WP}) + {L_{DFIG}}^{-1} \right) \tag{4.7}$$

It can be observed in expression (4.7) that the Q_C/S_{WP} ratio is linearly correlated with S_{SC}/S_{WP}. This result demonstrates the linear tendency of the boundary at the RCRR. The simplified method for obtaining the RCRR is given as follows:

- Set the resonance frequency value to match the RCRR boundary, e.g., $h_{max} = 13$.
- Set a range of short-circuit to wind park capacity ratios, e.g., $S_{SC}/S_{WP} = [2, 5, 10, \ldots, 100]$.
- Evaluate each short-circuit ratio in expression (4.7) to obtain the corresponding reactive compensation ratio Q_C/S_{WP}.
- Plot a blue line with all the $(S_{SC}/S_{WP}, Q_C/S_{WP})$.
- The region above the boundary is the RCRR.

This simplified procedure is considerably faster than the point-to-point testing because it only uses a one-dimensional sweep of S_{SC}/S_{WP} instead of a four dimensional-sweep of S_{SC}; S_{WP}; Q_C and h, and can be used as a quick reference to determine the compensation ratio required for a given harmonic resonance frequency at any given short-circuit ratio.

However, for wind parks with considerable feeder impedances between the generators and the PCC as in Fig. 4.9, the boundary of the RCRR starts to curve downwards with the larger values of S_{SC}/S_{WP}, as in Fig. 4.10. This effect is due to the feeder impedances which are not scaled by the wind park capacity. For a better fit of the RCRR boundary in these cases, it is advised to consider the feeder impedances and build the boundary as the black curve of Fig. 4.10, with the largest problematic short-circuit ratios S_{SC}/S_{WP} for every evaluated reactive power compensation level Q_C/S_{WP}.

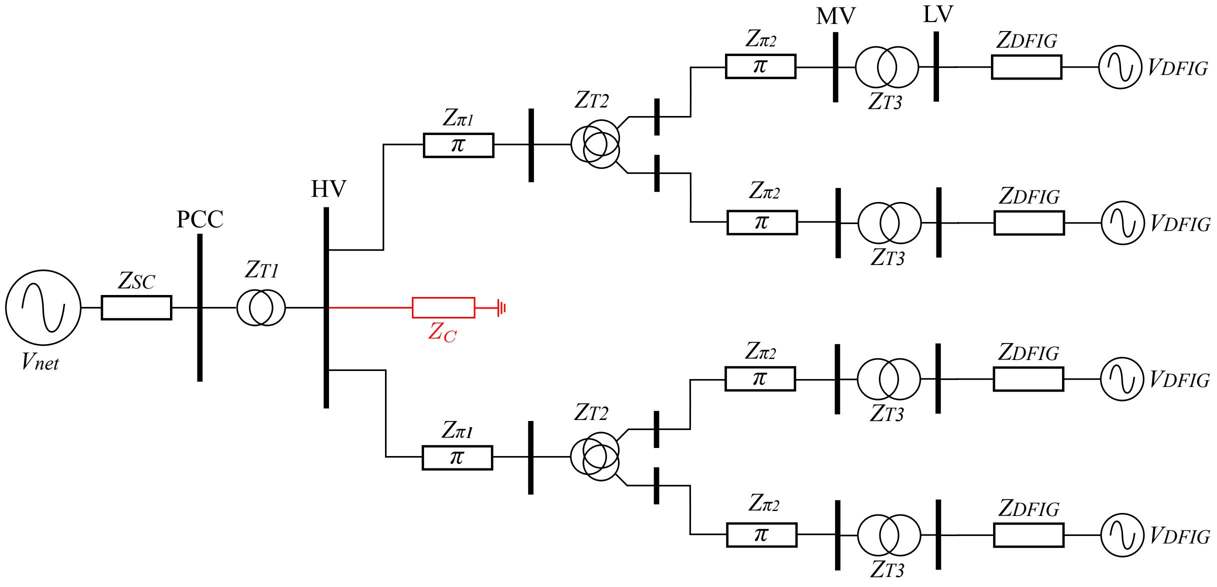

Figure 4.9 – Detailed WP with non-ideal feeders, bulk compensation

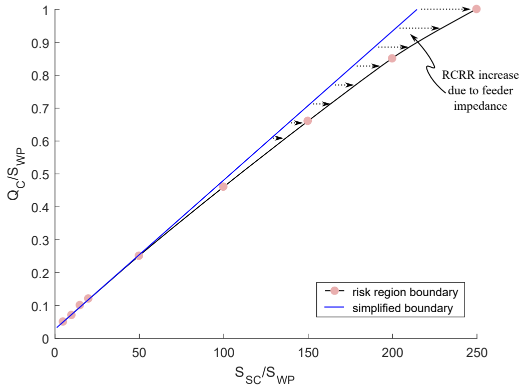

Figure 4.10 – RCRR boundary for detailed wind park with feeder impedances, comparison of simplified and point-to-point methods

4.2.2 Measurement-based approach to build the RCRR

Although, typically, the parameters of the equivalent circuit of large wind parks are known, it is important to update them periodically, as they may change with time due to wind park expansions and aging of the components. The equivalent impedance of the wind park can be updated continuously through field measurements. It can be calculated once two different operating conditions are monitored for a given frequency f (e.g., *pre* and *pos* a disturbance in the electric network), as follows:

$$Z\left(f\right) = \frac{\delta V}{\delta I} = \frac{V_{pos}\left(f\right) - V_{pre}\left(f\right)}{I_{pos}\left(f\right) - I_{pre}\left(f\right)} \tag{4.8}$$

If possible, it is advised to conduct the impedance measurement at the PCC where $Z = Z_{DFIG}$, by using the variables $I = I_{DFIG}$ and the $V = V_{PCC}$ from Fig. 4.11, so the measurements exclude the contribution of the reactive compensation capacitor. This consideration is useful to normalize the impedance profile of the DFIG and scale it according to the required wind park capacity. The reactive compensation capacitance can be modeled separately since it is a controlled variable.

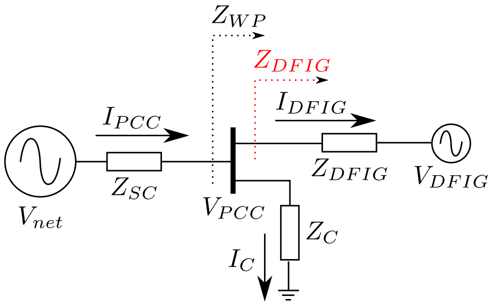

Figure 4.11 – Advised point to conduct impedance measurements

If the measurement without the reactive compensation bank contribution is not possible, the impedance corresponding to the capacitor can be removed anallytically using expression (4.9) as the information of the capacitance value is better known.

$$Z_{DFIG} = \left(\frac{1}{Z_{WP}} - \frac{1}{Z_C}\right)^{-1} \tag{4.9}$$

Once the DFIG impedance is known, the risk regions can be obtained for different wind park capacities by escalating the normalized DFIG impedance using expression (4.10).

$$Z_{DFIG}^{new} = Z_{DFIG}^{meas} \frac{S_{WP}^{meas}}{S_{WP}^{new}} \tag{4.10}$$

The RCRR can be built with the following procedure:

- Set the maximum evaluated harmonic order, e.g., $h_{max} = 13$.
- Set the evaluated frequency range, e.g., $h = [3, 4, 5, \ldots, h_{max}, h_{max} + 1]$.
- Set a range of wind park capacities, e.g., $S_{WP} = [2, 5, 10, \ldots, 100]$ MVA.
- Set a range of short-circuit capacities, e.g., $S_{SC} = [5, 10, 20, \ldots, 1000]$ MVA.
- Set a range of reactive power compensation ratios, e.g., $Q_C/S_{WP} = [0.01, 0.05, \ldots., 0.2]$.
- For each triple (S_{WP}, S_{SC}, Q_C) with $S_{WP} < S_{SC}$:
  - Obtain the escalated value of Z_{DFIG} to the respective wind park capacity S_{WP} using expression (4.10).
  - Calculate the impedances Z_{SC}, Z_C and Z_{WP}.
  - Calculate the amplification A at every evaluated harmonic from h.
  - If a peak value of amplification is detected in a frequency equal or lower than h_{max}, mark the respective pair of ratios $(S_{SC}/S_{WP}, Q_C/S_{WP})$ as a problematic combination for harmonic resonance.

- Plot all the problematic combinations for harmonic resonance to build the RCRR, using the S_{SC}/S_{WP} in the horizontal axis and Q_C/S_{WP} in the vertical axis.

Alternatively, a simplified method to calculate the boundary as a straight line from the origin is given as follows:

- Fix the wind park capacity to its original value from the measurement, e.g., $S_{WP} =$ 100 MVA.
- Fix the reactive power compensation ratio to its original value from the measurement, e.g., $Q_C/S_{WP} = 0.2$.
- Fix the Z_{DFIG} value at the resonance frequency $f_{res} = h_{max}$, e.g., $h_{max} = 13$.
- Set a range of short-circuit ratios S_{SC}/S_{WP} to be evaluated, e.g., $S_{SC}/S_{WP} = [2, 10, ..., 1000]$, and obtain the respective S_{SC} values.
- Determine the y-axis coordinate of a point **P**, which is located at the boundary of the RCRR, by using the previously fixed reactive power compensation ratio Q_C/S_{WP}.
- For each value of S_{SC}:
  - Calculate the amplification at h_{max} with expression (2.30).
  - Store the $(S_{SC}/S_{WP}, A(h_{max}))$ pairs.
- From the stored pairs, select the S_{SC}/S_{WP} with the highest $A(h_{max})$. This value corresponds to the x-axis coordinate of the point **P**.
- Draw a straight line from the origin to point **P**. This corresponds to an approximation of the RCRR boundary.

The previous procedure is an approximation since it neglects the effect of the y-axis shift near the origin (associated with the DFIG inductance term) and the change of tendency for large detailed wind parks which include feeder impedances. However, it holds well for wind parks where the feeder and transformer impedances can be neglected if compared with the generator impedances.

4.2.3 Validation study of the RCRR

The model-based and measurement-based methods to obtain the RCRR boundaries are verified in this section. In order to configure the EMT simulation, the resonance frequency was set to $h_{max} = 13$ and added to the grid equivalent voltage as 1 % of the fundamental. The wind park capacity was fixed at $S_{WP} = 100$ MVA for each DFIG model. Then, a range of short-circuit capacities $S_{SC}/S_{WP} = [2, 5, 10, \ldots, 100]$ was set. For each S_{SC}/S_{WP} ratio, the approximate value of the reactive power compensation ratio Q_C/S_{WP} was calculated with expression (4.7). This approximation was used as an initial guess $(Q_C/S_{WP})_0$ for the reactive power compensation ratio that produces resonance at h_{max} instead of searching the entire space of parameter combinations. Values from $(Q_C/S_{WP})_0 \pm 10\%$ in steps of 1 % were tested individually (for a total of 21 EMT simulations for each S_{SC}/S_{WP} ratio), and the voltage amplification at PCC of the h_{max} component was recorded. If an amplification peak was detected within the $(Q_C/S_{WP})_0 \pm 9\%$ interval, the respective Q_C/S_{WP} was stored as the closest value for resonance at h_{max}, thus, forming the pair of ratios $(S_{SC}/S_{WP}, Q_C/S_{WP})$ as part of the RCRR boundary. The resulting RCRR boundary is formed by the pink circles in Fig. 4.12 for the detailed wind parks. In the following comparisons, it is referred to as the true risk region boundary.

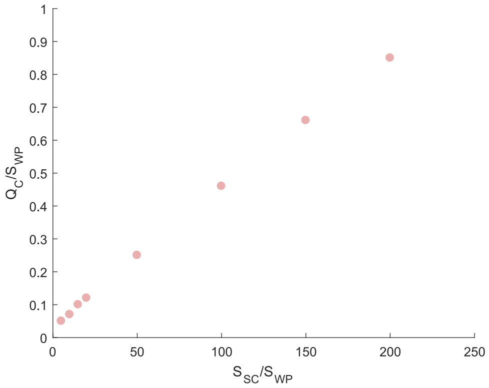

Figure 4.12 – True RCRR boundary obtained from repeated EMT simulation

The model-based method from section (4.2.1) was tested to obtain the RCRR. Once again, the DFIGs are modeled as impedances given that all the circuit parameters are known. The boundary of the RCRR corresponds to the black circles of Fig. 4.13. The model-based method was found to be accurate when compared to the true risk region boundary (pink circles) for both the aggregated and the detailed wind park which included line impedances. Equivalent results are obtained by using the measurement-based method from section (4.2.2).

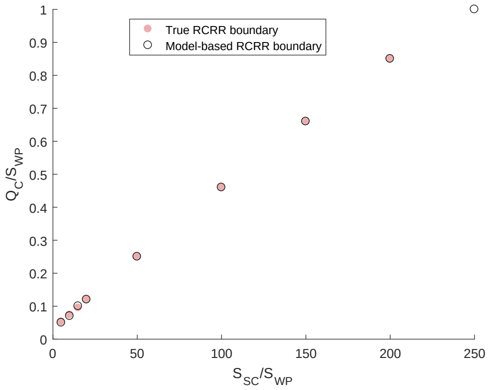

Figure 4.13 – Comparison of true RCRR boundary with model-based RCRR boundary

The results of the model-based simplified method to obtain the boundary of the RCRR are shown in Fig. 4.14. This method uses the approximate resonance frequency expression to calculate directly the reactive power compensation ratio Q_C/S_{WP} from the short-circuit ratio S_{SC}/S_{WP} and draw the boundary of the risk region as a straight line. It can be observed that the results are accurate. As detailed previously in Fig. 4.10, the reactive power compensation ratio results diverge from the line of the approximation in wind parks with considerable feeder impedances, especially for short circuit ratios $S_{SC}/S_{WP} > 100$. Nevertheless, the approximation can still be considered valid as compensation ratios in the range of $Q_C/S_{WP} > 0.5$ are unlikely to occur in practice.

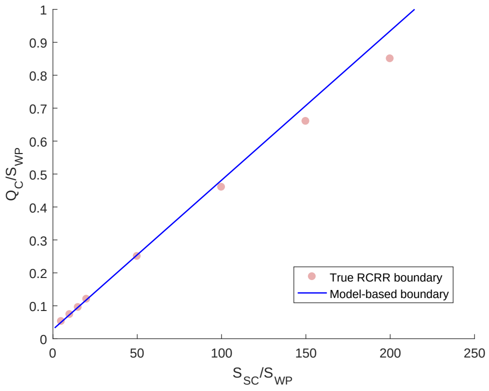

Figure 4.14 – Comparison of true RCRR with simplified model-based RCRR boundary

Finally, the results of the measurement-based simplified method are presented in Fig. 4.15. This method uses a single wind park impedance measurement to calculate the risk region boundary, approximating the boundary as a straight line from the origin up to the measured point that produces resonance at the desired harmonic frequency h_{max}.

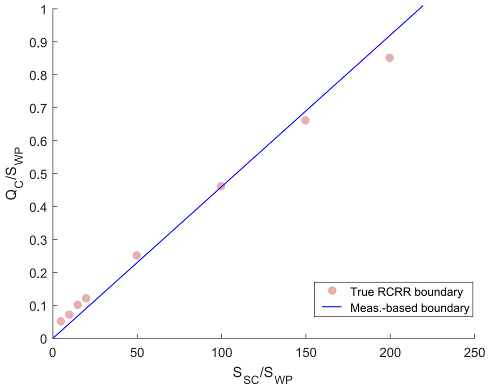

Figure 4.15 – Comparison of true RCRR with measurement-based RCRR boundary

It can be observed that the method also yields accurate results. The method is valid for the cases that consider feeder impedances since reactive power compensation ratios in the range of $Q_C/S_{WP} > 0.3$ are unlikely since they occur only at over-compensation conditions.

4.2.4 Sensitivity study of the RCRR

The reactive compensation at resonance risk chart is mostly sensitive to the maximum evaluated harmonic frequency h_{max}. As the region is defined in the short-circuit ratio vs. reactive power compensation ratio (S_{SC}/S_{WP} vs. Q_C/S_{WP}) plane, it already incorporates most of the studied variables, with exception to the X/R ratio of the grid equivalent. The sensitivity of the chart to this parameter will also be studied as it demonstrated influence over the resonance frequency value for some compensation capacities.

The boundaries of the different regions resulting from the sensitivity analysis are presented in Fig. 4.16.

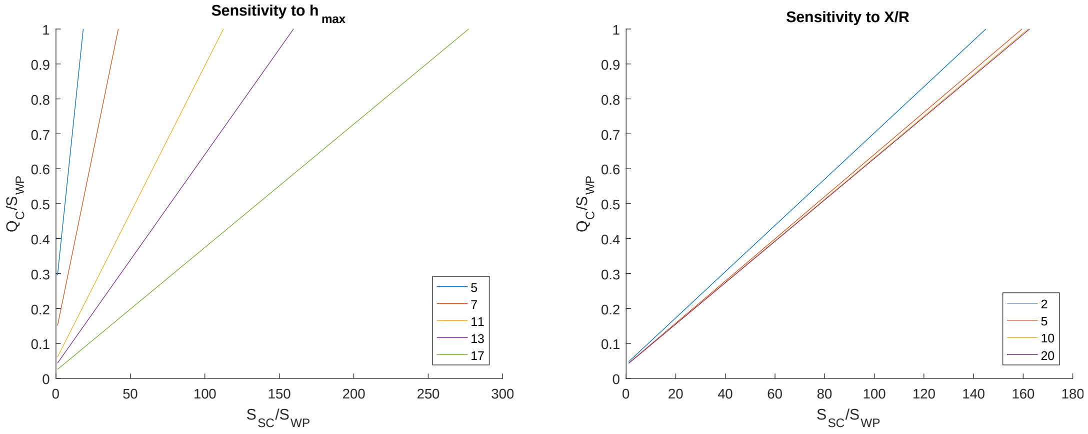

(a) Sensitivity to maximum evaluated harmonic h_{max}

(b) Sensitivity to the X/R ratio of the grid

Figure 4.16 – Sensitivity analysis of RCRR, influential variables

From the sensitivity analysis, the following observations can be made:

- A higher maximum harmonic limit leads to a larger risk region. This is an expected result as the range of problematic resonances is expanded, thus, more parameter combinations may have resonance frequencies with values equal or lower to h_{max}.
- Again, parameters related to the resistances of the circuit have little to no effect in the value of the resonance frequency. The reduction of the X/R slightly rotates the limit counterclockwise towards the y-axis, however, low values of X/R are uncommon at PCCs of large wind parks. In addition, ratios of $X/R \geq 5$ do not produce significant changes in the boundary.
- The RCRR chart can also be delimited by two harmonic values, i.e. the lowest expected harmonic distortion order, and the highest. For example, using the results from Fig. 4.16 (a), the user of the chart can set a range of frequencies based on the typical spectrum at the PCC (i.e., 300 to 780 Hz). At this condition, the RCRR chart would correspond to those combinations that fall within the blue and purple curves.

4.3 Resonance risk region chart

The RCRR chart can be used to determine a capacitor bank for reactive power compensation to avoid resonances under a certain frequency limit. With such fixed reactive power compensation ratio Q_C/S_{WP}, it is still necessary to check for problematic amplification levels of background distortions. Two conditions can be used to objectively determine if a resonance is problematic:

- Condition 1 (resonance frequency): the maximum resonance frequency must be at most the h_{max} harmonic, as resonances above this harmonic will hardly ever be excited (distortions in the electric grid above the limiting harmonic are improbable).
- Condition 2 (amplification): the resonance must amplify the harmonic voltage distortion present in the electric network by a factor greater or equal to A_{lim}.

These conditions can be determined based on the specific characteristics of each utility and wind park location. In the present work, Condition 1 is set in the 13^{th} harmonic, as it is the highest harmonic order with non-negligible distortions in the Brazilian transmission system (as mentioned in chapter 1). Condition 2 can be set in $A_{lim} = 3$, so a background distortion of $V_h = 1.3$ % of the fundamental produces a $THD_V = 4$ %.

Once conditions 1 and 2 are established, resonances can be divided into problematic and not problematic using the chart at Fig. 4.17.

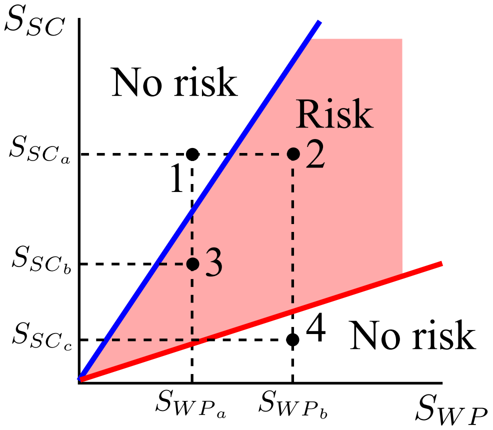

Figure 4.17 – Theoretical harmonic resonance risk region

The resonance risk region (RRR) indicates combinations of wind park capacities and short-circuit levels that create problematic resonances. This chart greatly facilitates resonance analysis in wind parks as engineers can quickly figure out if wind park expansions or grid changes create problematic amplifications due to harmonic resonances. The scenarios at Fig. 4.17 yield the following information:

- Given conditions 1 and 2, the points at the white region (e.g., points 1 and 4) are wind park and grid combinations free of harmonic resonance risk. On the other hand, the combinations located within the shaded region (e.g., points 2 and 3), present risk of harmonic resonance.
- A wind park with characteristics of point 1 will experience problematic harmonic resonances if its capacity is expanded from S_{WP_a} to S_{WP_b} while the percentage of reactive power compensation and the grid short-circuit level remain unchanged (i.e. move from point 1 to point 2 of Fig. 4.17).

- A wind park will also experience problematic resonance if its characteristic is in point 4 and the short-circuit level at the PCC is increased from S_{WP_c} to S_{WP_a} (i.e. move from point 4 to point 2 of Fig. 4.17).
- A short-circuit level decrease from S_{SC_a} to S_{SC_b} (i.e. move from point 1 to point 3 of Fig. 4.17) will also create resonance concerns in the wind park.

Detailed EMT simulations are conducted for all S_{SC} vs. S_{WP} combinations using the circuit at Fig. 4.5. For each combination, 5^{th}, 7^{th}, 11^{th} and 13^{th} harmonic order distortions are added to the grid equivalent, to check the presence of amplification at PCC voltage over A_{lim} for any of these frequencies. If the condition is met, this S_{SC} vs. S_{WP} combination is inside the risk region. The resulting risk region is formed by the pink dots in Fig. 4.18.

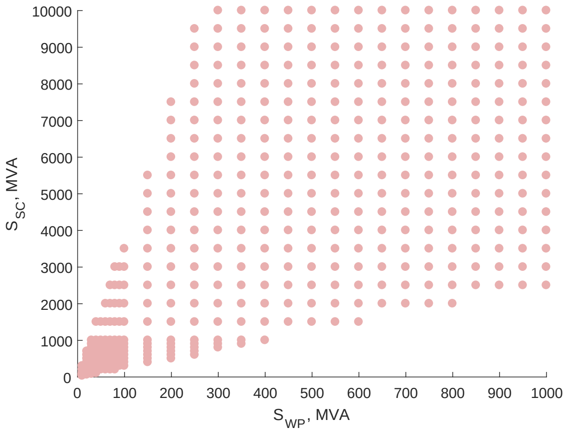

Figure 4.18 – Problematic harmonic resonances under conditions 1 and 2

However, this process is very time-consuming to obtain the chart as numerous EMT simulations are required. The following section uses the DFIG impedance model of Chapter 2 to propose an analytic method for determining this risk region without the need to run any EMT simulations.

4.3.1 Model-based approach to build the RRR

Recall the circuit at Fig. 4.7 (a), where the DFIG, the reactive compensation capacitor and the grid are connected at PCC. If V_{net} is considered the only source at a given harmonic frequency, the circuit can be simplified to Fig. 4.7 (b) to calculate V_{PCC} and its amplification A with respect to the existing voltage distortion in the system V_{net} as in expression (4.3).

$$A = \frac{V_{PCC}}{V_{net}} = \frac{Z_{WP}}{Z_{SC} + Z_{WP}}$$

Given a fixed reactive power compensation ratio Q_C/S_{WP}, the RRR can be built by evaluating a range of wind park capacities S_{WP} and a range short-circuit capacities S_{SC}. These parameters are used to calculate the impedance expressions of the circuit.

Later on, at each pair (S_{WP}, S_{SC}), expression (4.3) can be evaluated at the harmonic frequencies from the grid (e.g., 5^{th}, 7^{th}, 11^{th}, 13^{th} harmonics). If any of the amplification values of the evaluated harmonics is greater or equal to A_{lim}, then the corresponding pair (S_{WP}, S_{SC}) is marked as a problematic combination for harmonic resonance (i.e. as a pink dot in the RRR).

The model-based approach to build the RRR in a point-to-point fashion can be summarized as follows:

- Set conditions 1 and 2, e.g., $h_{max} = 13$ and $A_{lim} = 3$.
- Set a range of evaluated harmonics, e.g., $h = [5, 7, 11, h_{max}]$.
- Set a range of wind park capacities, e.g., $S_{WP} = [2, 5, 10, \ldots, 100]$ MVA.
- Set a range of short-circuit levels, e.g., $S_{SC} = [5, 10, 20, \ldots, 1000]$ MVA.
- Fix a reactive power compensation ratio, e.g., $Q_C/S_{WP} = 0.2$.
- For each pair (S_{WP}, S_{SC}) with $S_{WP} < S_{SC}$:
  - Calculate the impedances Z_{SC}, Z_C and Z_{WP} with expressions (4.4), (4.6) and (4.5) respectively.
  - Calculate the amplification A at every evaluated harmonic from h.
  - If the amplification limit is violated at any evaluated harmonic h (i.e., $A_{lim} < A(h)$), mark the respective pair (S_{WP}, S_{SC}) as a problematic combination for harmonic resonance.
- Plot all the problematic combinations for harmonic resonance to build the RRR, using the S_{WP} in the horizontal axis and S_{SC} in the vertical axis.

The previous procedure tests each parameter combination in a point-to-point fashion using the impedance model and can be applied to any wind park topology. To do this, all the wind park impedances (impedances from lines, transformers and DFIGs) must be properly referred to the PCC, and then, the amplification expression can be calculated.

The RRR can also be estimated with a simplified procedure that delimits the region by two straight lines. These boundaries were added to the RRR at Fig. 4.19 (a).

These boundaries define slopes of lines in the S_{WP} vs. S_{SC} plane, i.e., they correspond to a pair of short-circuit ratios S_{SC}/S_{WP}. The slopes can be obtained with a graphical approach as in Fig. 4.19 (b), by selecting the lowest (red) and the largest (blue) ratios that meet the problematic amplification criterion $A > A_{lim}$. The boundaries cross the origin $(0, 0)$.

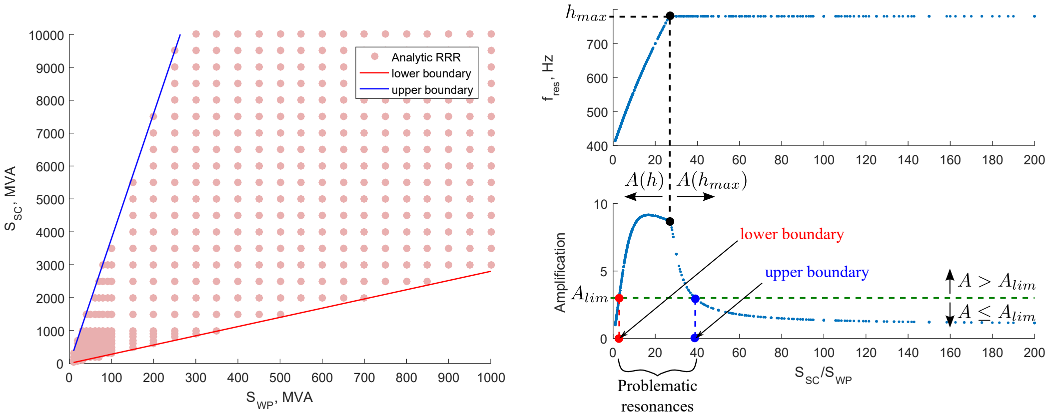

(a) Analytic RRR (b) Limits of RRR

Figure 4.19 – Analytic RRR and graphical limits definition

Fig. 4.19 (a) can be drawn by setting a range of S_{SC}/S_{WP} ratios and a fixed S_{WP}, or with a fixed S_{SC}/S_{WP} ratio and a range of S_{WP} values. Then, at each S_{SC}/S_{WP} ratio, the impedances of the model and the amplification at PCC are calculated. If the amplification at any of the evaluated harmonics violates the $A > A_{lim}$ limit, then the S_{SC}/S_{WP} ratio is flagged as problematic for harmonic resonance. Finally, the lowest and the largest flagged ratios correspond to RRR boundaries. The change of tendency marked by the black dashed lines in Fig. 4.19 (b) corresponds to the point where the frequency of the resonance is higher than h_{max}. If the harmonic resonance is above h_{max}, the amplification is evaluated at h_{max}.

The simplified method to obtain the RRR is summarized as follows:

- Set conditions 1 and 2, e.g., $h_{max} = 13$ and $A_{lim} = 3$.
- Set a range of evaluated harmonics, e.g., $h = [5, 7, 11, h_{max}]$.
- Set a fixed wind park capacity, e.g., $S_{WP} = 100$ MVA.
- Set a range of short-circuit to wind park capacity ratios, e.g., $S_{SC}/S_{WP} = [2, 5, 10, \dots, 100]$, and calculate its respective S_{SC} values to form the (S_{WP}, S_{SC}) pairs.
- Fix a reactive power compensation ratio, e.g., $Q_C/S_{WP} = 0.2$.
- For each pair (S_{WP}, S_{SC}):
  - Calculate the impedances Z_{SC}, Z_C, Z_{DFIG} and Z_{WP} with expressions (2.27), (2.29), (2.22) and (2.23) from chapter 2.
  - Calculate the amplification A at every evaluated harmonic from h.
  - If the amplification limit is violated at any evaluated harmonic h, $i.e.A_{lim} < A(h)$, mark the respective ratio S_{SC}/S_{WP} as a problematic ratio for harmonic resonance.
- Plot a red line with the lowest problematic ratio S_{SC}/S_{WP} as the slope from $S_{WP} = 0$ MVA to $S_{WP} = 100$ MVA. This line corresponds to the lower boundary of the RRR.

- Plot a blue line with the highest problematic ratio S_{SC}/S_{WP} as the slope from $S_{WP} = 0$ MVA to $S_{WP} = 100$ MVA. This line corresponds to the upper boundary of the RRR.
- The risk region is between the boundaries as the RRR.

This simplified procedure provides a first screening estimate of the risk region. This estimate is more accurate when the line and transformer impedances of the wind park can be neglected. However, for wind parks with considerable feeder impedances between the turbines and the PCC such as Fig. 4.9, the lower boundary of the RRR starts to curve upwards with the larger values of S_{WP} as in Fig. 4.20. In the present example, this happens because the feeder impedances do not depend on wind park capacity and their value becomes more dominant at larger wind park capacities, where the DFIG impedances become smaller. If the feeders are scalated to the wind park capacity (when designing a wind park), then the DFIG impedances dominate over the feeder's.

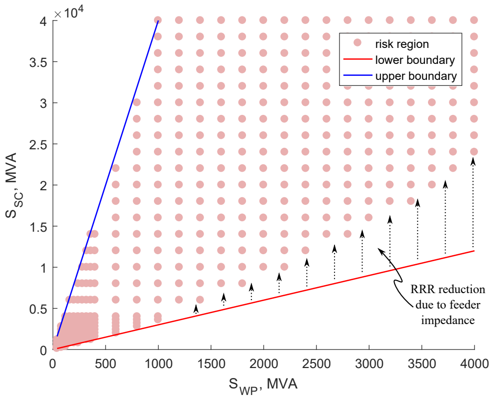

Figure 4.20 – RRR for detailed wind park with feeder impedances

4.3.2 Measurement-based approach to build the RRR

The detailed algorithm to obtain the RRR is given as follows:

- Set conditions 1 and 2, e.g., $h_{max} = 13$ and $A_{lim} = 3$.
- Set a range of evaluated harmonics, e.g., $h = [5, 7, 11, h_{max}]$.
- Set a range of wind park capacities, e.g., $S_{WP} = [2, 5, 10, \ldots, 100]$ MVA.
- Set a range of short-circuit capacities, e.g., $S_{SC} = [5, 10, 20, \ldots, 1000]$ MVA.
- Fix a reactive power compensation ratio, e.g., $Q_C/S_{WP} = 0.2$.
- For each pair (S_{WP}, S_{SC}) with $S_{WP} < S_{SC}$:
  - Scale the normalized impedance of the DFIG by the desired S_{WP} capacity of the wind park to obtain Z_{DFIG}.
  - Calculate the impedances Z_{SC}, Z_C and Z_{WP}.
  - Calculate the amplification A at every evaluated harmonic from h.
- If the amplification limit is violated at any evaluated harmonic h (i.e., $A_{lim} < A(h)$), mark the pair (S_{WP}, S_{SC}) as a problematic combination for harmonic resonance.

The previous procedure is the same as the model-based approach, but instead of calculating the impedance of the DFIG in terms of the model parameters, it is measured at the wind park PCC and escalated based on S_{WP} for other wind park capacities.

Similar to the model-based approach, this algorithm can also be simplified to determine only the lower and upper boundaries of the risk region. This can be done as follows:

- Set conditions 1 and 2, e.g., $h_{max} = 13$ and $A_{lim} = 3$.
- Set a range of evaluated harmonics, e.g., $h = [5, 7, 11, h_{max}]$.
- Set a fixed wind park capacity, e.g., $S_{WP} = 100$ MVA.
- Set a range of short-circuit to wind park capacity ratios, e.g., $S_{SC}/S_{WP} = [2, 5, 10, \ldots, 100]$, and calculate its respective S_{SC} ratios to form the (S_{WP}, S_{SC}) pairs.
- Fix a reactive power compensation ratio, e.g., $Q_C/S_{WP} = 0.2$.
- For each pair (S_{WP}, S_{SC}):
  - Scale the normalized impedance of the DFIG to the desired wind park capacity S_{WP} to obtain Z_{DFIG}.
  - Calculate the impedances Z_{SC}, Z_C and Z_{WP}.
  - Calculate the amplification A at every evaluated harmonic from h.
  - If the amplification limit is violated at any evaluated harmonic h (i.e., $A_{lim} < A(h)$), mark the respective ratio S_{SC}/S_{WP} as a problematic ratio for harmonic resonance.
- Plot a red line with the lowest problematic ratio S_{SC}/S_{WP} as the slope from $S_{WP} = 0$ to $S_{WP} = 100$ MVA. This line corresponds to the lower boundary of the RRR.
- Plot a blue line with the highest problematic ratio S_{SC}/S_{WP} as the slope from $S_{WP} = 0$ to $S_{WP} = 100$ MVA. This line corresponds to the upper boundary of the RRR.
- The region between the boundaries is the RRR.

4.3.3 Validation study of the RRR

The effectiveness of the model-based and measurement-based methods proposed to obtain the RRR are verified in this section. First, detailed EMT simulations are conducted for a given range of S_{WP} vs. S_{SC} combinations. For each combination, 5^{th}, 7^{th}, 11^{th} and 13^{th} harmonic order distortions are added to the grid equivalent and it is verified if there is any amplification greater than A_{lim}. If the condition is met, the (S_{WP}, S_{SC}) pair is part of the risk region. The resulting RRR is formed by the pink circles, as in Fig. 4.21 for the detailed wind park. In the following comparisons, it is referred to as the true risk region.

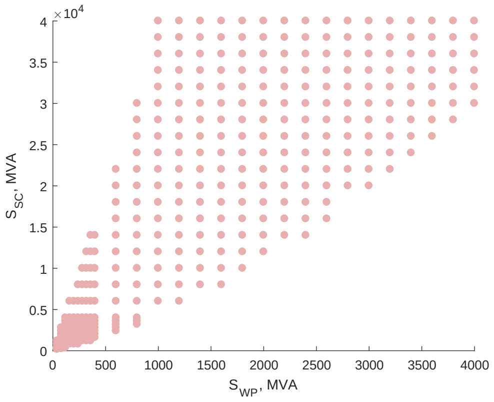

Figure 4.21 – True RRR obtained from repeated EMT simulation

First, the model-based method from section 4.3.1 was tested to obtain the RRR. DFIGs are modeled as equivalent impedances and all circuit parameters are assumed to be known. The resulting risk region is formed by the black circles shown in Fig. 4.22. It is possible to see this region matches the true risk region with good accuracy. A similar result is obtained when the equivalent impedance of the wind park is obtained with the measurement-based method described in section 4.3.2.

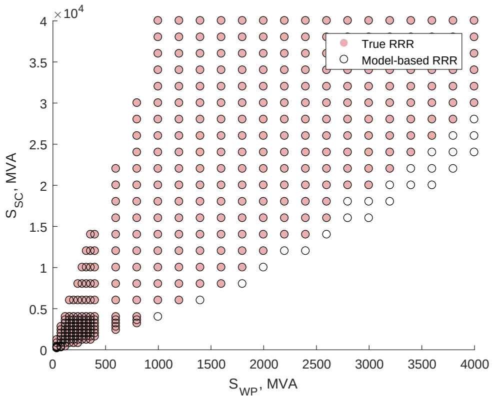

Figure 4.22 – Comparison of true RRR with model-based RRR

The simplified model-based method to determine the upper and lower boundaries of the risk region (described in section 4.3.1) was also tested. The results are shown with the solid lines presented in Fig. 4.23.

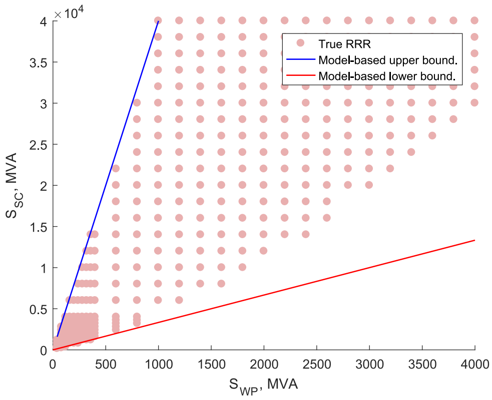

Figure 4.23 – Comparison of true RRR with simplified model-based RRR boundaries

It is worthwhile to mention this method neglects the impedance of lines and transformers inside the wind park. The results match the upper and lower boundaries of the risk region, although it encompasses a larger area than the true risk region that becomes more pronounced with larger wind park capacities. Therefore, this simplified method can be used with confidence by engineers as it determines a conservative risk region (larger than the true risk region). Similar results are obtained with the measurement-based method of section 4.3.2 to obtain the boundaries of the risk region. Results for this case are shown with dashed lines in Fig. 4.24.

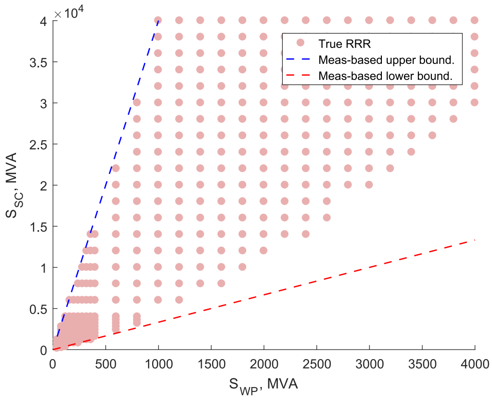

Figure 4.24 – Comparison of true RRR with simplified measurement-based RRR boundaries

Overall, these validation studies confirmed the model-based and measurement-based approaches to obtain the risk region in detail match the true risk region obtained through repeated EMT simulations. The simplified model-based and measurement-based methods proposed to obtain the upper and lower boundaries of the risk region also work well, although they provide a more conservative estimate of the true risk region near the lower boundary.

4.3.4 Sensitivity study of the RRR

The resonance risk region is sensitive to the maximum harmonic order of concern h_{max} and the maximum allowable amplification A_{lim}, which are the 2 conditions used to delimit a problematic parameter combination for harmonic resonance. The maximum amplification and the resonance frequency demonstrated to be sensitive to the X/R ratio of the grid equivalent and to the reactive power compensation level of the wind park Q_C/S_{WP} (see section 2.4.3 of chapter 2). This section investigates how these four parameters affect the risk region using the simplified model-based approach from section 4.3.1. Study results shown in Fig. 4.25 reveal that:

- Higher amplification limits A_{lim} lead to smaller risk regions. This is expected as a higher allowable amplification means less resonances are considered to be problematic. This condition affects both the upper and lower boundaries of the RRR.
- A smaller range of evaluated frequencies leads to smaller risk regions. This condition affects primarily the upper boundary of the RRR. Therefore, a resonance must occur at a more restricted number of low frequencies in order to be problematic.
- A higher reactive power compensation level moves the risk region counterclockwise towards the vertical axis as the evaluated frequency range is kept constant, and therefore, the short-circuit ratio S_{SC}/S_{WP} has to increase to keep the resonances below the h_{max} limit. This results in higher short-circuit capacities S_{SC} and lower wind park capacities S_{WP}. Therefore, problematic resonances will take place in stronger grids. This behavior can be explained by observing the relationship of the variables within the approximate resonance frequency expression (2.37) (see section (2.5)). If Q_C/S_{WP} increases, S_{SC}/S_{WP} must increase for f_{res} to remain unchanged.

$$f_{res} \approx f_0 \sqrt{\left(Q_C/S_{WP}\right)^{-1} \left(\sqrt{1+\left(X/R\right)^{-2}}\left(S_{SC}/S_{WP}\right) + {L_{DFIG}}_{pu}{}^{-1}\right)}$$

- Changes in the X/R ratio of the short-circuit level do not affect the risk region significantly because the largest portion of the resonance damping is provided by the wind farm and the grid equivalent has less effect on it.

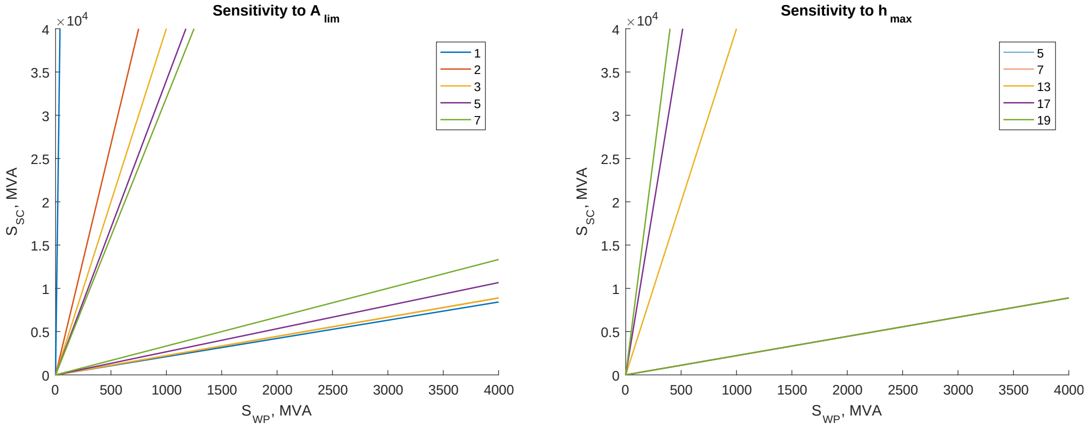

(a) Sens. to amplification limit A_{lim}

(b) Sens. to maximum evaluated harmonic h_{max}

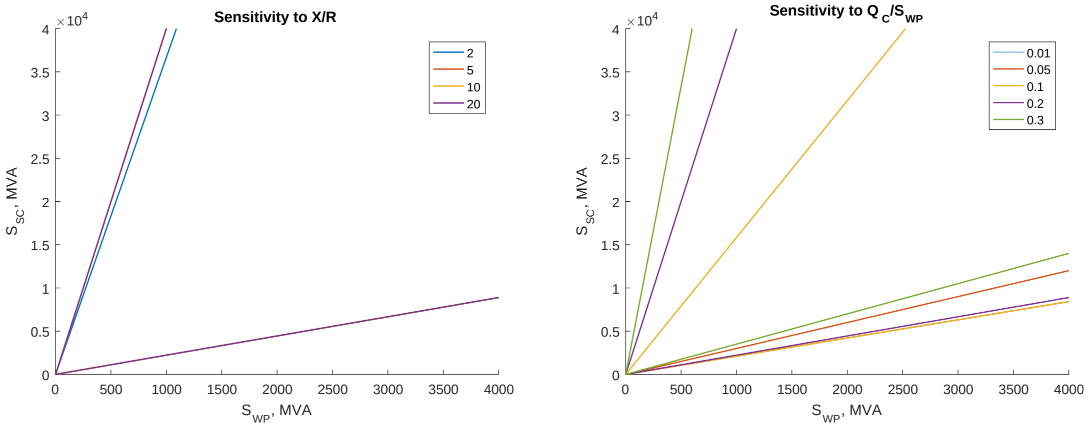

(c) Sens. to X/R ratio of the grid

(d) Sens. to compensation ratio Q_C/S_{WP}

Figure 4.25 – Sensitivity analysis of RRR, influential variables

4.4 Different wind park topologies

In some cases, DFIG-based wind parks can feature tuned harmonic filters with capacitive characteristic at each generator. An example with these filters is shown in Fig. 4.26. This new topology changes the shape of the RRR but the model-based and measurement-based methodologies proposed to obtain the charts remain the same.

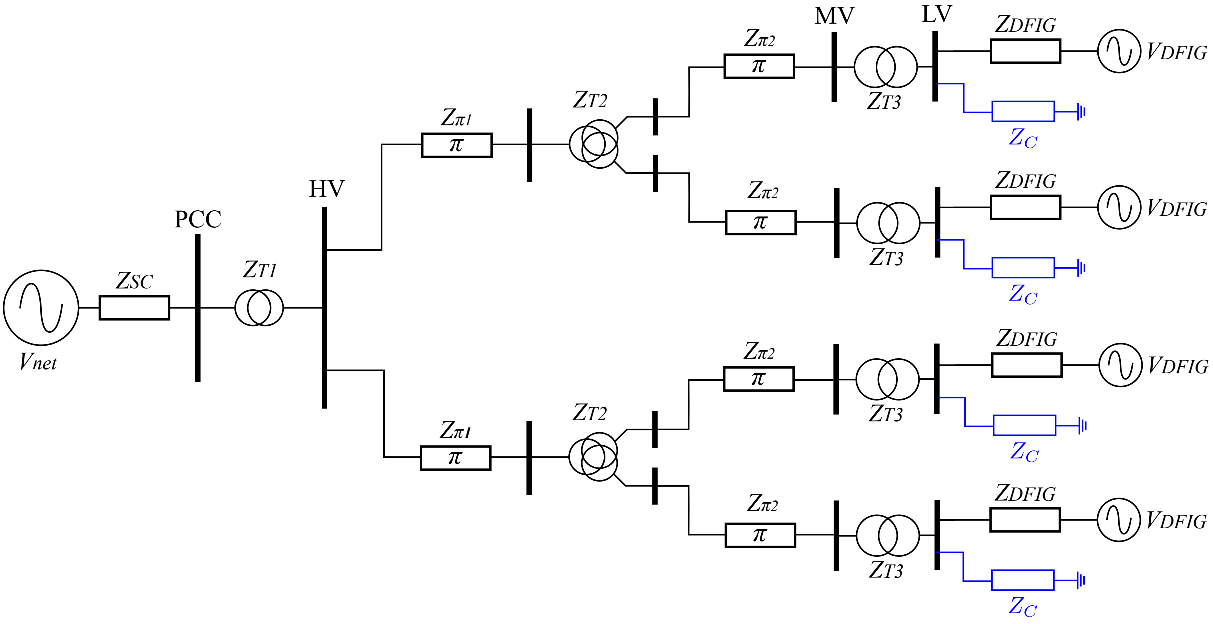

Figure 4.26 – Detailed WP with non-ideal feeders, dispersed harmonic filters

To illustrate the previous affirmation, the RRR of the circuit shown in Fig. 4.26 is obtained and presented in Fig. 4.27. The capacitive filters were set to match a total reactive power compensation of $Q_C/S_{WP} = 0.2$, or 5% per DFIG equivalent with a quality factor of $QF = 50$. This last parameter defines a series resistance to the capacitors, which is calculated with expression (4.11).

$$R_C = \frac{1}{QF\omega_0 C_C} \tag{4.11}$$

The blue impedances from Fig. 4.26 correspond to $Z_C = R_C + 1/(sC_C)$. The resulting risk region is presented in Fig. 4.27. The results confirm that both risk regions (model-based and measurement-based), match well the risk region from detailed EMT simulations. In the model-based case, the circuit of the wind park must be known so that the equivalent impedance Z_{WP} can be calculated. The measurement-based algorithm does not require such knowledge of the parameters.

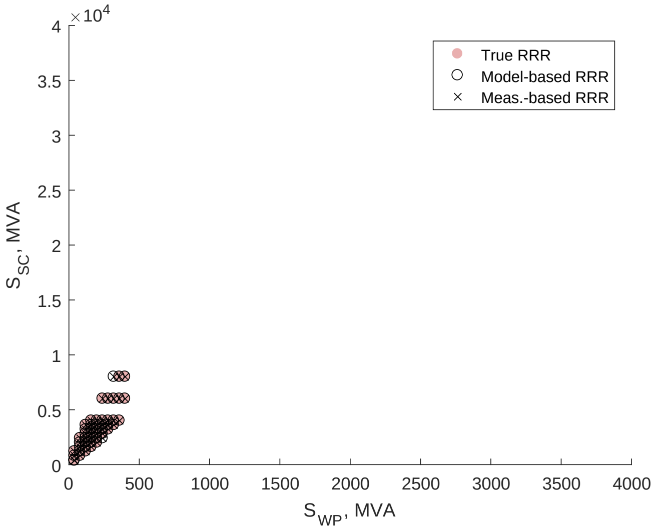

Figure 4.27 – Resonance risk region due to filtering

A second important takeaway of Fig. 4.27 is that the risk region is much smaller than in previous studies of this chapter. This occurs because the filter capacitors are smaller, which shifts resonances to higher frequencies (above the frequency range of concern), and the series resistance of the capacitors damps the amplification at resonance.

4.5 Summary

This chapter analyzed the occurrence of weakly damped harmonic resonances in DFIG-based wind parks. A practical method to quickly assess the occurrence and characteristics of these resonances was proposed, consisting in the analysis of the following two charts:

- Chart for assessment of the reactive power compensation level: this chart informs the characteristic of the resonance frequency due to the network and wind park interaction for different levels of reactive power compensation, see Fig. 4.28 (a). To evaluate the resonance frequency for a given reactive power compensation level, only the short-circuit level of the electric system at the PCC, the rated power capacity of the wind park, and the level of reactive power compensation installed in this wind park are required.
- Chart for resonance risk assessment: this chart informs if there is the risk of problematic voltage amplifications due to harmonic resonances at the PCC of the grid and a DFIG wind park, see Fig. 4.28 (b). Once the chart has been obtained, it is possible to evaluate if such harmonics are problematic by using only the short-circuit level of the electric system at the PCC, the rated power capacity of the wind park, and a fixed reactive power compensation level.

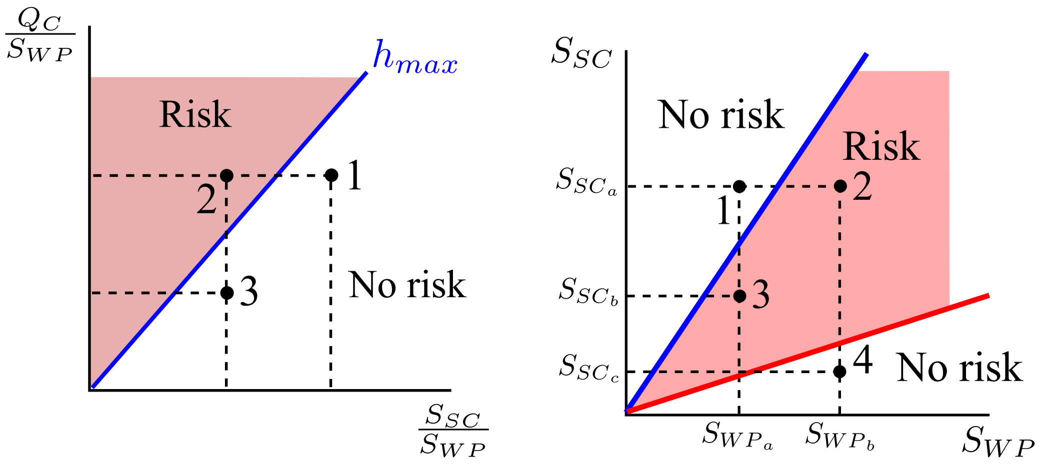

(a) Reactive compensation risk region (b) Harmonic resonance risk region

Figure 4.28 – Theoretical risk regions for harmonic resonance analysis

One purely analytic (model-based) and one measurement-based method were provided to obtain each of the proposed charts without the need of performing any EMT simulation, which requires high computational effort and modeling detail. To employ the purely analytic method, the impedance parameters of the generators installed in the wind park must be known, as well as the gains of the generator control loops and the line and transformer impedances. For large wind parks, it is rather realistic to assume that these parameters are known with good precision. On the other hand, if the parameters of the DFIG model are unavailable, the measurement-based method can be employed. This method requires equipment capable of measuring gapless waveforms at the point of study.

Even if all circuit parameters are known, they are likely to change with time and with expansions or reconfigurations of the wind park. The measurement-based method can be employed in order to obtain the new values of these parameters and update the model to perform further studies.

5 Conclusion

The penetration of renewable generation, such as solar and wind, is growing in electrical power systems. In particular, DFIG-based wind parks are the dominant wind generation technology nowadays. This technology is widely adopted due to its lower commercial cost and control flexibility. However, it presents topological disadvantages such as direct coupling of the machine stator to the grid and reactive compensation requirements for machine magnetization. These topological characteristics make the generator more vulnerable to power quality disturbances in the grid, such as transients, overvoltage, harmonic distortion and resonance.

Resonances in the range from 180 to 1500 Hz are a particular concern in DFIG-based wind parks due to two main reasons. First, at this frequency range, the power electronics converters have a negative resistance behavior that reduces the overall resonance damping. If resonance damping is negative, the system is unstable. Second, even if the resonance has positive damping, it may become problematic if it occurs at frequencies such as the 5^{th}, 7^{th}, 11^{th} or 13^{th} harmonics. Resonances at these frequencies can be excited by background distortions of the transmission system.

These two types of resonances (i.e., unstable and weakly damped resonances) were studied in this dissertation. They were initially characterized in terms of their causes and effects on the system. Then, practical charts were developed for anticipating these phenomena without running EMT simulations. The proposed charts are versatile, as 1) they can be obtained either analytically or with measurements from the PCC of the wind park, 2) once obtained, they can be easily consulted based on information that is readily available to engineers, and 3) they are useful even under constantly changing grid conditions (i.e., with grid reconfigurations, unit outages, connection of compensation bank stages etc.).

More specifically, three practical charts were proposed, and they can be described as follows:

- Unstable Resonance Risk Region (URRR): This chart correlates the short-circuit ratio (S_{SC}/S_{WP}) with the reactive power compensation ratio (Q_C/S_{WP}) of the wind park. It defines a risk region where combinations of S_{SC}/S_{WP} with Q_C/S_{WP} result in unstable resonance (i.e., create resonances with negative damping).

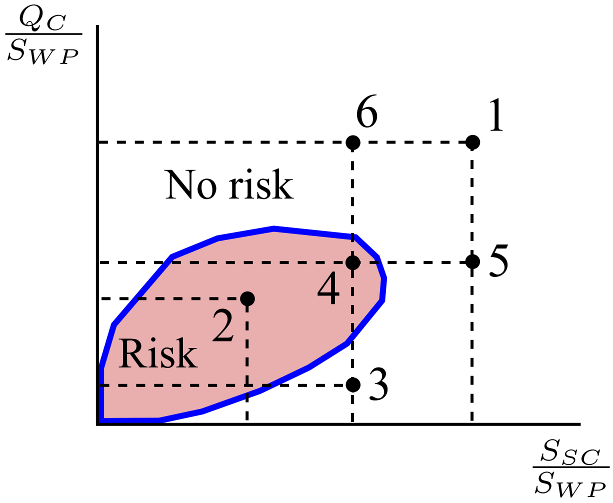

Figure 5.1 – Unstable resonance risk chart

- Reactive Compensation at Resonance Risk (RCRR): This chart correlates the short-circuit ratio S_{SC}/S_{WP} with the reactive compensation ratio Q_C/S_{WP} of the wind park. It defines a risk region where combinations of S_{SC}/S_{WP} with Q_C/S_{WP} result in resonances at frequencies below a maximum harmonic order h_{max}. The chart is used to determine if a reactive power compensation bank will result in a problematic harmonic resonance.

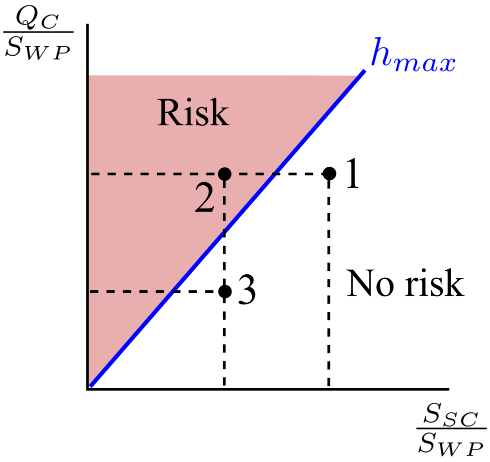

Figure 5.2 – Reactive compensation at resonance risk chart

- Resonance Risk Region (RRR): This chart correlates the wind park capacity (S_{WP}) with the short circuit capacity (S_{SC}) at PCC, for a fixed reactive power compensation ratio Q_C/S_{WP}. It defines a risk region where combinations of S_{WP} with S_{SC} result in problematic weakly damped resonances (i.e., resonances that amplify background grid distortion by more than a limit A_{lim}).

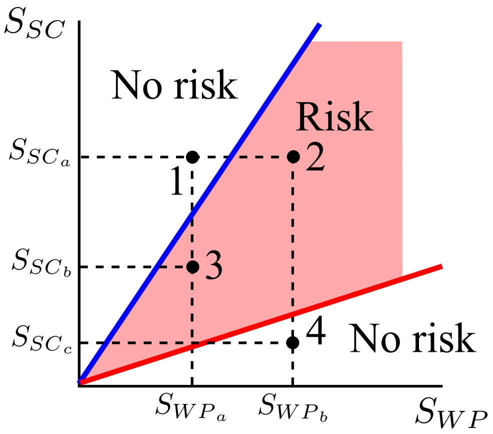

Figure 5.3 – Reactive compensation risk chart

Model-based and measurement-based methods were proposed to build each of these charts without the need to run any detailed EMT simulation.

Overall, the analyses of this dissertation have revealed that high-frequency unstable resonance is unlikely to become a generalized concern as it can be mitigated with proper control tuning, and grid resistance can also contribute with system damping. In other words, the URRR can be managed to become negligible. Nevertheless, weakly damped harmonic resonances are still a concern, and should be considered in wind park planning and operation to avoid equipment malfunction and damages. The RRR and RCRR can help to facilitate these tasks.

The following points can be expanded in future research:

- Evaluate sub-synchronous resonance with the proposed methodologies. The same analysis should be conducted for wind parks with full-converter generators.
- Develop mitigation strategies to the high-frequency resonance problem.
- Study the characteristics of resonances due to significant cable capacitances and passive filter capacitances.
- Study unstable resonances in scenarios with multiple wind parks and develop methods for ranking contributions from different wind parks (or even from different generators inside a wind park) to an instability. This information can be used, for example, to determine which wind park should be disconnected first to mitigate an instability.
- Investigate how this resonance stability management can be improved if synchronized waveform measurements are available at all wind parks.
- Study the risk of unstable resonances in distribution systems with high penetration of inverter-based generators (photovoltaic and/or of wind generation).

Bibliography

ABEEÓLICA. *Boletim anual de geração eólica.* [S.l.], 2017. Referenced at page 16.

ANDRADE, F.; MEDEIROS, J.; KIYOSHI, S. Discussões e proposições do processo de gerenciamento do conteúdo harmônico gerado pelos parques eólicos conectados a rede básica. In: *XXIII SNPTEE Seminario Nacional de Produção e Transmissão de Energia Eletrica.* [S.l.: s.n.], 2015. Referenced at page 22.

BACELLS, J.; GONZÁLEZ, D. Harmonics due to resonance in a wind power plant. In: *8th International Conference on Harmonics and Quality of Power ICHQP 98.* Athens, Greece: [s.n.], 2011. Referenced at page 16.

BAROUDI, J.; DINAVAHI, V.; KNIGHT, A. A review of power converter topologies for wind generators. *ELSEVIER Renewable Energy*, v. 32, p. 2369–2385, jan. 2007. Referenced at page 16.

BRADT, M.; BADRZADEH, B.; CAMM, E.; MUELLER, D.; SCHOENE, J.; SIEBERT, T.; SMITH, T.; STARKE, M.; WALLING, R. Harmonics and Resonance Issues in Wind Power Plants. In: IEEE PES WIND PLANT COLLECTOR SYSTEM DESIGN WORKING GROUP. *Power and Energy Society General Meeting, 2011 IEEE.* [S.l.], 2011. Referenced at page 22.

BUCHHAGEN, C.; RAUSCHER, C.; MENZE, A.; JUNG, J. BorWin1 - First Experiences with harmonic interactions in converter dominated grids. In: *International ETG Congress 2015; Die Energiewende - Blueprints for the new energy age; Proceedings of.* Bayreuth, Germany: [s.n.], 2015. Referenced 3 times at pages 16, 20, and 21.

CAMM, E.; BEHNKE, M.; BOLADO, O.; BOLLEN, M. Reactive Power Compensation for Wind Power Plants. In: *Power and Energy Society General Meeting, 2009 IEEE.* [S.l.]: IEEE, 2009. IEEE PES Wind Plant Collector System Design Working Group. Other authors: Bradt, M. and Brooks, C. and Dilling, W. and Edds, M. and Hejdak, W. and Houseman, D. and Klein, S. and Li, F. and Li, J. and Maibach, P. and Nicolai, T. and Patino, J. and Pasupulati, S. and Samaan, N. and Saylors, S. and Siebert, T. and Smith, T. and Starke, M. and Walling, R. Referenced at page 18.

CAMM, E.; EDWARDS, C. Reactive Compensation Systems for Large Wind Farms. In: *Transmission and Distribution Conference and Exposition, 2008. T&D. IEEE/PES.* [S.l.]: IEEE, 2008. Chicago, IL. USA. Referenced at page 18.

CHANG, Y.; HU, J. Modeling, analysis and parameters design of rotor current control in DFIG-based wind turbines for dynamic performance optimizing. In: *2017 IEEE Energy Conversion Congress and Exposition (ECCE).* Ohio, USA: [s.n.], 2017. Referenced at page 26.

EBRAHIMZADEH, E.; BLAABJERG, F.; WANG, X.; BAK, C. L. Harmonic Stability and Resonance Analysis in Large PMSG-Based Wind Power Plants. *IEEE Transactions on Sustainable Energy*, Vancouver, BC, Canada, v. 9, n. 1, p. 12–23, jan. 2018. Referenced 2 times at pages 21 and 38.

FAN, L.; MIAO, Z. Nyquist-Stability-Criterion-Based SSR Explanation for Type-3 Wind Generators. *IEEE Transactions on Energy Conversion*, v. 27, n. 3, p. 807–809, 2012. Referenced 2 times at pages 21 and 54.

FAN, L.; ZHU, C.; MIAO, Z.; HU, M. Modal Analysis of a DFIG-Based Wind Farm Interfaced With a Series Compensated Network. *IEEE Transactions on Energy Conversion*, v. 26, n. 4, p. 1010–1020, 2011. Referenced at page 21.

GAGNON, R.; TURMEL, G.; LAROSE, C.; BROCHU, J.; SYBILLE, G.; FECTEAU, M. Large-Scale Real-Time Simulation of Wind Power Plants into Hydro-Québec Power System. In: *9th International Workshop on Large-Scale Integration of Wind Power Into Power Systems as well as on Transmission Networks for Offshore Wind Plants.* Quebec, Canada: [s.n.], 2010. Referenced at page 24.

HALPIN, S. Comparison of IEEE and IEC Harmonic Standards. In: *Power Engineering Society General Meeting, 2005. IEEE.* [S.l.: s.n.], 2005. Referenced at page 22.

HAMZA, K. E. W.; LINDA, H.; CHERIF, L. LCL filter design with passive damping for photovoltaic grid connected systems. In: *Renewable Energy Congress (IREC), 2015 6th International.* [S.l.: s.n.], 2015. Referenced at page 25.

JAZAERI, M.; SAMADI, A.; NAJAFI, H.; NOROOZI-VARCHESHME, N. Eigenvalue Analysis of a Network Connected to a Wind Turbine Implemented with a Doubly-Fed Induction Generator (DFIG). *Journal of Applied Research and Technology*, v. 10, n. 5, p. 791–811, out. 2012. Referenced at page 21.

KARAAGAC, U.; MAHSEREDJIAN, J.; JENSEN, S.; GAGNON, R.; FECTEAU, M.; KOCAR, I. Safe Operation of DFIG based Wind Parks in Series Compensated Systems. *IEEE Transactions on Power Delivery*, v. 33, n. 2, p. 709–718, abr. 2018. Referenced at page 20.

LAROSE, C.; GAGNON, R.; PRUD'HOMME, P.; FECTEAU, M.; ASMINE, M. Type-III Wind Power Plant Harmonic Emissions: Field Measurements and Aggregation Guidelines for Adequate Representation of Harmonics. *IEEE Transactions on Sustainable Energy*, v. 4, n. 3, p. 797–804, jul. 2013. Referenced 2 times at pages 20 and 22.

LEAO, R.; SAMPAIO, R.; ANTUNES, F. *Harmônicos em sistemas elétricos.* 5th. ed. [S.l.]: Elsevier, 2014. Referenced 4 times at pages 17, 18, 22, and 68.

LIAO, X.; SUN, H.; WONG, S.; TIAN, L.; WANG, M.; LIU, X. Impedance Modeling of DFIG-Wind Turbine System. In: *Circuits and Systems (ISCAS), 2015 IEEE International Symposium on.* [S.l.: s.n.], 2015. Referenced at page 28.

LIU, Z.; RONG, J.; ZHAO, G.; LUO, Y. Harmonic Assessment for Wind Parks Based on Sensitivity Analysis. *IEEE Transactions on Sustainable Energy*, v. 8, n. 4, p. 1373–1382, out. 2017. Referenced at page 21.

MONJO, L.; SAINZ, L.; JUN, L.; PEDRA, J. Study of resonance in wind parks. *Electric Power Systems Research*, v. 128, p. 30–38, 2015. Referenced at page 21.

ONS. *ProRede Submodulo 3.6: Requisitos técnicos mínimos para a conexão as instalações de transmissão.* [S.l.], 2010. Referenced at page 18.

ONS. *ProRede Submodulo 2.8: Gerenciamento dos indicadores de qualidade da energia elétrica da Rede Básica.* [S.l.], 2011. Referenced at page 22.

ONS. *Dados ANATEM/ANAREDE sistema brasileiro.* 2018. Disponível em: <https://agentes.ons.org.br/avaliacao_condicao/casos_eletromecanicos.aspx>. Referenced at page 16.

PATEL, J.; JOSHI, S. Harmonic Stability of Grid Connected Renewable Energy Source-A Case Study. In: *Universities Power Engineering Conference (UPEC), 2017 52nd International.* [S.l.: s.n.], 2017. Referenced at page 16.

PRECIADO, V.; MADRIGAL, M.; MULJADI, E.; GEVORGIAN, V. Harmonics in a Wind Power Plant. In: *Power and Energy Society General Meeting, 2015 IEEE.* Colorado, United States: [s.n.], 2015. Referenced at page 22.

REN21. *Renewables 2016: Global Status Report (GSR).* 2017. Disponível em: <http://www.ren21.net>. Referenced at page 16.

SHALIL, S.; PARSA, L. Impedance Modeling of Three-Phase Voltage Source Converters in DQ, Sequence, and Phasor Domains. *IEEE Transactions on Energy Conversion*, v. 32, n. 3, p. 1139–1150, set. 2017. Referenced at page 31.

SONG, Y.; BLAABJERG, F. Analysis of the Behavior of Undamped and Unstable High-Frequency Resonance in a DFIG System. *IEEE Transactions on Power Electronics*, v. 32, n. 6, p. 4370–4394, jun. 2017. Referenced 2 times at pages 19 and 28.

SONG, Y.; BLAABJERG, F. Overview of DFIG-Based Wind Power System Resonances Under Weak Networks. *IEEE Transactions on Power Electronics*, v. 32, n. 12, p. 9105–9116, dez. 2017. Referenced 3 times at pages 17, 19, and 28.

SONG, Y.; WANG, X.; BLAABJERG, F. High-Frequency Resonance Damping of DFIG-Based Wind Power System Under Weak Network. *IEEE Transactions on Power Electronics*, v. 32, n. 3, p. 1927–1940, mar. 2017. Referenced 5 times at pages 19, 28, 47, 66, and 69.

SORENSEN, P.; HAUGE, P.; VIKKELSO, A.; KOLBAEK, J.; FATHIMA, K.; UNNIKRISHNAN, A.; LAKAPARAMPIL, Z. *Power Quality and Integration of Wind Farms in Weak Grids in India.* [S.l.], 2000. Referenced at page 16.

TENTZERAKIS, S.; PAPATHANASSIOU, S. An Investigation of the Harmonic Emissions of Wind Turbines. *IEEE Transactions on Energy Conversion*, v. 22, n. 1, p. 150–158, mar. 2007. Referenced at page 22.

VIETO, I.; SUN, J. Sequence Impedance Modeling and Analysis of Type-III Wind Turbines. *IEEE Transactions on Energy Conversion*, 2017. Early access. Referenced at page 28.

WANG, X. *Harmonic Stability in Wind Power Plants.* 2014. Disponível em: <http://www.dffv.dk/english/-/media/Sites/dffv/Dokumenter/Presentations/Zone%20B/05-Danish-Wind-Industry-Annual-Event_Final-wang.ashx>. Referenced 2 times at pages 12 and 28.

WANG, X.; BLAABJERG, F. Harmonic Stability in Power Electronic Based Power Systems: Concept, Modeling, and Analysis. *IEEE Transactions on Smart Grid*, mar. 2018. Referenced at page 21.

WECC. Description and Technical Specifications for Generic WTG Models - A Status Report. In: WECC WORKING GROUP ON DYNAMIC PERFORMANCE OF WIND POWER GENERATION & IEEE WORKING GROUP ON DYNAMIC PERFORMANCE OF WIND POWER GENERATION OF THE IEEE PES POWER STABILITY CONTROLS SUBCOMMITTEE OF THE IEEE PES POWER SYSTEM DYNAMIC PERFORMANCE COMMITTEE. *IEEE/PES Power Systems Conference and Exposition*. Arizona, USA, 2011. Referenced at page 16.

XIE, X.; ZHANG, X.; LIU, H.; LIU, H.; LI, Y.; ZHANG, C. Characteristic Analysis of Subsynchronous Resonance in Practical Wind Farms Connected to Series-Compensated Transmissions. *IEEE Transactions on Energy Conversion*, v. 32, n. 3, p. 1117–1126, set. 2017. Referenced at page 16.

XU, W.; HUANG, Z.; CUI, Y.; WANG, H. Harmonic Resonance Mode Analysis. *IEEE Transactions on Power Delivery*, v. 20, n. 2, 2005. Referenced at page 39.

XU, W.; LIU, X.; LIU, Y. Assessment of harmonic resonance potential for shunt capacitor applications. *Electric Power Systems Research*, v. 57, p. 97–104, 2001. Referenced at page 34.

YANG, K.; BOLLEN, M.; AMARIS, H.; ALVAREZ, C. Decompositions of harmonic propagation in wind power plant. *Electric Power Systems Research*, v. 141, p. 84–90, ago. 2016. Referenced at page 22.

YANG, K.; BOLLEN, M.; LARSSON, E. A.; WAHLBERG, M. Measurements of harmonic emission versus active power from wind turbines. *Electric Power Systems Research*, v. 108, p. 304–314, 2013. Referenced at page 22.

YANG, K.; BOLLEN, M.; WAHLBERG, M. A comparison study of Harmonic Emission Measurements in Four Windparks. In: *Power and Energy Society General Meeting, 2011 IEEE*. [S.l.: s.n.], 2011. Referenced at page 22.

ZHENG, R.; BOLLEN, M. *Harmonic Resonances Associated with Wind Farms*. Swiss, 2010. Referenced at page 17.

APPENDIX A – Tables of model parameters

Table 3 – Parameters for DFIG impedance validation

$K_{p\,GSC} = 0.83$	$K_{i\,GSC} = 5$	$f_{GSC} = 1600$ Hz
$K_{p\,RSC} = 0.6$	$K_{i\,RSC} = 8$	$f_{RSC} = 2700$ Hz
$\omega_I = 2\pi \times 2000$ rad/s	$\xi = 0.7$	$\omega_0 = 2\pi \times 60$ rad/s
$\omega_r = 1.2$ pu	$R_f = 0.003$ pu	$L_f = 0.3$ pu
$R_s = 0.23$ pu	$L_s = 0.18$ pu	$L_m = 2.9$ pu
$R_r = 0.23$ pu	$L_r = 0.18$ pu	$V_{\underset{PCC}{base}} = 33$ kV
$S_{SC} = 1500$ MVA	$X/R = 5$	$S_{WP} = 100$ MVA

Table 4 – Parameters of detailed WP feeder

Basis for pu calculation		
S, VA	V_{LL}, V	f, Hz
450×10^6	150×10^3	60
Line parameters, pu		
$R_{\pi1}$	$L_{\pi1}$	$C_{\pi1}$
0.022	1.802×10^{-4}	7.841×10^{-6}
$R_{\pi2}$	$L_{\pi2}$	$C_{\pi2}$
0.018	5.8×10^{-4}	7.54×10^{-5}
Transformers parameters, pu		
$L_{Z_{T1}}$	$L_{Z_{T2}}$	$L_{Z_{T3}}$
4.46×10^{-4}	3.8×10^{-4}	3.18×10^{-4}
V_{net}/V_{PCC}	V_{PCC}/V_{HV}	V_{HV}/V_{MV}
150/150	150/150	150/33

Table 5 – Parameters for grid and DFIG-based WP, harmonic resonance simulation

$K_{p\,GSC} = 0.83$	$K_{i\,GSC} = 5$	$f_{GSC} = 1600$ Hz
$K_{p\,RSC} = 0.6$	$K_{i\,RSC} = 8$	$f_{RSC} = 2700$ Hz
$\omega_I = 2\pi \times 2000$ rad/s	$\xi = 0.7$	$\omega_0 = 2\pi \times 60$ rad/s
$\omega_r = 1.2$ pu	$R_f = 0.003$ pu	$L_f = 0.3$ pu
$R_s = 0.23$ pu	$L_s = 0.18$ pu	$L_m = 2.9$ pu
$R_r = 0.23$ pu	$L_r = 0.18$ pu	$V_{\underset{PCC}{base}} = 33$ kV
$X/R = 5$		$Q_C/S_{WP} = 0.2$